GEOSTANDARDS and GEOANALYTICAL RESEARCH

GGR Cutting-Edge Review

NanoSIMS: Technical Aspects and Applications in Cosmochemistry and Biological Geochemistry

Peter **Hoppe** (1)*, Stephanie **Cohen** (2) and Anders **Meibom** (2)

(1) Particle Chemistry Department, Max Planck Institute for Chemistry, Hahn-Meitner-Weg 1, 55128, Mainz, Germany
(2) Laboratory for Biological Geochemistry, Architecture, Civil and Environmental Engineering (ENAC), Ecole Polytechnique Fédérale de Lausanne, CH-1015, Lausanne, Switzerland
* Corresponding author. e-mail: peter.hoppe@mpic.de

The NanoSIMS ion probe is a new-generation SIMS instrument, characterised by superior spatial resolution, high sensitivity and multi-collection capability. Isotope studies of certain elements can be conducted with 50–100 nm resolution, making the NanoSIMS an indispensable tool in many research fields. We review technical aspects of the NanoSIMS ion probe and present examples of applications in cosmochemistry and biological geochemistry. This includes isotope studies of presolar (stardust) grains from primitive meteorites and of extraterrestrial organics, the search for extinct radioactive nuclides in meteoritic materials, the study of lunar samples, as well as applications in environmental microbiology, cell biology, plant and soil science, and biomineralisation.

Keywords: secondary ion mass spectrometry, ion probe, isotope ratio imaging, high spatial resolution.

Received 21 Dec 12 – Accepted 11 Mar 13

Secondary ion mass spectrometry (SIMS) is an analytical technique, which is used in a variety of fields spanning from the material sciences over biology to geo- and cosmochemistry. One incarnation of a SIMS instrument is the 'ion microprobe' or 'ion probe', which permits *in situ* studies at the micrometre or sub-micrometre scale. The ion probe uses a finely focused primary ion beam to erode the target and produce secondary ions that can be mass analysed. Ion probe SIMS offers μg g^{-1} or better detection limits for most elements, essentially periodic table coverage, imaging and depth profiling capabilities, and isotopic analyses of major and minor elements with (sub-) micrometre lateral resolution on a wide range of materials, for which the main requirements are that they can be prepared with relatively flat surfaces and introduced into an ultra-high-vacuum environment. Furthermore, a combination of imaging and depth profiling allows three-dimensional chemical and isotope maps to be created. The fundamentals of ion probe SIMS were developed some 50 years ago, but it was not until the 1980s that the technique became an important tool to a wider range of researchers in different fields. This development started with the advent of the IMS 3f (Lepareur 1980) and Sensitive High Resolution Ion Microprobe (SHRIMP; Clement *et al.* 1977) instruments, developed by Cameca and the Australian National University, respectively.

In section 'NanoSIMS fundamentals' of this review, we provide a simplified description of how an ion probe functions, then focus on the specifics of the Cameca NanoSIMS 50/50L ion probe. NanoSIMS is the name of an instrument, but the term is now also used as synonym for ion probe analyses with sub-micrometre lateral resolution, which is what the development of the NanoSIMS instrument has made possible. Developed in the 1990s and originally intended for applications in biology, the first commercial NanoSIMS instruments were delivered at the beginning of this millennium to two laboratories conducting research in cosmochemistry at Washington University in St. Louis and the Max Planck Institute for Chemistry, respectively. Both these laboratories worked closely with Cameca to implement several improvements in the instrument design. It was quickly recognised by other research fields that the high spatial resolution (down to 50 nm) and high sensitivity of the NanoSIMS would open new research opportunities. Today, the NanoSIMS can be considered an indispensable analytical

doi: 10.1111/j.1751-908X.2013.00239.x

tool in many fields, including material sciences, biology, cosmochemistry and the geosciences. There are currently more than thirty NanoSIMS instruments operational world-wide.

Section 'Applications in cosmochemistry' presents examples of NanoSIMS applications in cosmochemistry, with the emphasis on isotopic studies of presolar (stardust) grains. Examples of isotope studies of extraterrestrial organics, the search for extinct radioactive nuclides in meteoritic materials and other studies of meteoritic and lunar samples complement this section. Section 'Applications in biological geochemistry' provides examples of NanoSIMS applications in biological geochemistry and includes research work in environmental microbiology, cell biology, biomineralisation and on plants and soils.

NanoSIMS fundamentals

Ion probe secondary ion mass spectrometry

The basic principles of the SIMS technique are described in detail in the literature (Benninghoven *et al.* 1987). Here, we give a brief introduction focused on the fundamental and practical aspects of the technique.

Sputtering, ionisation, transmission and ion detection: The physical principle is illustrated in Figure 1. A solid surface is bombarded by a primary beam of ions with energies typically in the range of several kilo-electron volts (keV). Each primary ion hitting the surface triggers a collision cascade in the target. This causes atoms and small molecules from the upper layers of the sample (typically down to 5–20 nm depth) to be ejected into the vacuum, a process referred to as 'sputtering' (Sigmund 1969). Most of these sputtered particles are neutral and cannot be analysed. But a fraction of the sputtered particles, typically in the range between 10^{-5} and 10^{-2}, but strongly depending on the species and the composition of the target (matrix), are ionised in the process of ejection. These ions are referred to as 'secondary ions'. It is these ions that are physically separated and counted in the mass spectrometer, hence the name secondary ion mass spectrometry (SIMS). The NanoSIMS is a magnetic sector mass spectrometer, which means that secondary ions of different mass-to-charge ratio are physically separated by the Lorentz force as they pass through a magnetic field arranged perpendicular to the velocity vector of the secondary ions.

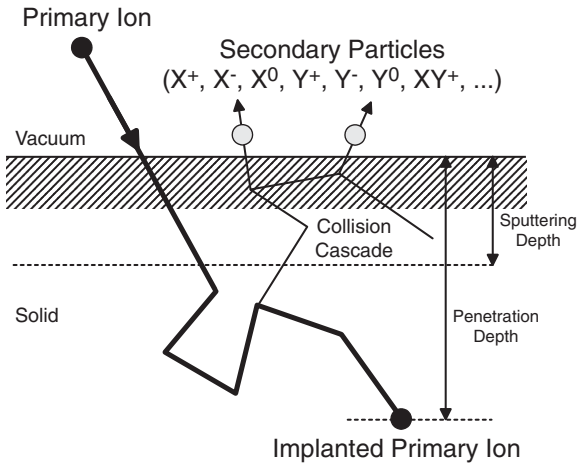

Figure 1. The physical principle of SIMS. Impacting primary ions on a sample surface creates sputtering or ejection of atoms and small molecules, a fraction of which are ionised. These secondary ions are subsequently transferred through a mass spectrometer and counted.

The secondary ions leaving the sample surface have relatively low kinetic energies (several eV, although a small fraction can obtain energies in the keV range) and are extracted by an electrostatic field and transferred to a mass spectrometer. Of particular importance in this process are the spectrometer transmission and the mass resolution with which the secondary ions reach the detectors. High transmission, that is, low loss of secondary ions between the sample surface and the detector, and high mass resolution, that is, the capability to separate the secondary ions or molecules of interest from other ions/molecules of very similar mass (for a definition of mass resolution see below), are prerequisites for precise isotope measurements. These requirements are met in many of the designs of magnetic-sector ion probe instruments, such as the NanoSIMS.

It is instructive to parameterise the process of creation and transmission of secondary ions in an ion probe. Primary ions impact the surface with a certain frequency per surface area. Each primary ion sputters a number of atoms from the sample (here we ignore the formation of molecules). A fraction of these atoms will be ionised. These secondary ions are then transferred through the mass spectrometer and detected. Thus, for a given number of primary ions impacting the surface per second, a number of secondary ions of the isotope ^iM will reach the detector and be counted each second.

The process can be parameterised as follows:

$$I(^iM) = d_b \times S \times Y \times X_M \times A_i \times Y_i \times T \qquad (1)$$

Here, $I(^iM)$ is the count rate at the detector counting the arrival of isotope ^iM of the element M, which has an atomic concentration in the sample of X_M and an isotopic

abundance A_i. The primary beam has a density of d_b (ions/second/surface area) and is assumed to cover a surface area S with a flat distribution of primary ions. Each primary ion sputters Y atoms off the sample (sputter yield), a fraction Y_i of which is ionised (ionisation yield of isotope ^iM). T is the probability that a given ion is transferred through the mass spectrometer and detected. Note that the product $Y_i \times T$ is referred to as the useful yield, because it specifies the fraction of sputtered isotopes ^iM that are both ionised and detected, which depends on the physics of the sputtering process and the specifics of the instrument, respectively.

So, going through Equation 1, the entire process is revealed. A given surface area S receives $d_b \times S$ primary ions per second. This will sputter $d_b \times S \times Y$ atoms off the sample per second. A fraction of these atoms are of the species M and of the isotope ^iM: $d_b \times S \times Y \times X_M \times A_i$. Of the isotopes ^iM removed from the sample every second, a fraction Y_i is ionised, and a fraction T of these is transferred though the mass spectrometer and counted.

In order to get an idea of the operational mode of a NanoSIMS, one can insert typical numbers into Equation 1. Let us assume that a primary beam of 1 pA is focused and delivered to a surface area of about 0.01 μm^2 (i.e., 100 by 100 nm^2). In other words, about 6×10^6 primary ions arrive on this surface area every second. Each primary ion is assumed to sputter five atoms off the surface. If an atom M has an atomic concentration of 10% in the sample and an isotopic abundance of 10%, $X_M \times A_i = 10^{-2}$. If about 1 out of 1000 sputtered atoms ^iM is ionised (i.e., $Y_i = 10^{-3}$) and 50% of these ions are transferred and detected, the count rate at the detector will be: $I(^iM) = 6 \times 10^6$ (ions s^{-1}) $\times$ $5 \times 10^{-2} \times 10^{-3} \times 0.5 = 150$ counts per second (cps).

This example illustrates at the same time the ion probe process and one of the peculiarities of the NanoSIMS. In the NanoSIMS, a very feeble primary beam is focused to a very small beam spot, down to about 50 nm under certain conditions. This spatial resolution opens up a multitude of scientifically interesting applications across a wide spectrum of disciplines, as illustrated below, but the price paid for high spatial resolution, which can only be achieved with low primary beam current, is that the number of secondary ions produced is correspondingly low, and high analytical precision is therefore more difficult to obtain. In comparison, a conventional ion probe typically delivers a primary beam of say 10 nA (equivalent to ~ 6×10^{10} cps) to a surface area of about 400 μm^2 (20 by 20 μm^2). The count rate for the same isotope ^iM from the same sample would be 10^4 times higher, that is, about 1.5×10^6 cps, but the spatial resolution, that is, the beam spot on the sample surface, is 40000 times larger.

Important primary ion species are oxygen and caesium because their use promotes secondary ion yields. Oxygen (O^- on the NanoSIMS) favours the formation of positive secondary ions and is chiefly used when alkali, alkaline earth and transition metals are determined. Caesium (Cs^+), on the other hand, favours the formation of negative secondary ions and is preferentially employed for isotope measurements of, for example, H, C, N (measured as CN^-), O, Si and S. Sputter yields are typically in the order of 1–10 secondary particles per impinging primary ion; however, most of these occur as uncharged atoms. Useful yields depend not only on the ionisation efficiency but also on the transmission through the mass spectrometer and detector characteristics. In the most favourable cases, that is, when transmission and detection efficiency are close to unity, the useful yield may reach values at the per cent level for certain elements.

Matrix, instrumental mass fractionation and QSA effects: Quantitative SIMS measurements are complicated by several factors: isobaric interferences, matrix effects, instrumental mass fractionation (IMF) and problems related to ion detection and sample preparation (i.e., non-conducting samples, topography). Magnetic sector-type instruments offer a mass resolution power (MRP) of several 1000, which is sufficient to resolve most isobaric interferences for the low atomic number elements (see Isotope measurements). The matrix effect can lead to extremely strong fractionation of major, minor or trace elements because the ionisation yield of two different elements from the same matrix can differ by many orders of magnitude and their relative ion yields might change substantially with even minor chemical changes in the sample matrix (Shimizu and Hart 1982). For isotope ratio measurements, a mass fractionation due to matrix effects also exists that is linked to small differences in ionisation. The only way to control such matrix effects is to also analyse well-characterised reference materials with essentially identical chemical composition and preferably crystal structure and orientation. IMF induces a systematic bias in the analysis of, for example, an isotopic ratio because of small differences in spectrometer transmission and detection efficiency for each isotope. In general, for a given element, the IMF tends to artificially enhance the relative abundance of the lighter isotope (i.e., lead to a count rate of the heavier isotope that is apparently too low).

Both matrix effect and IMF are mass-dependent effects, that is, proportional to the mass difference between two isotopes (Slodzian *et al.* 1980). For example, the mass fractionation on a measured $^{18}O/^{16}O$ ratio will be twice that for the $^{17}O/^{16}O$ ratio measured at the same time on the same sample. For isotope measurements, the mass

fractionation is typically in the per mil to per cent range. For many applications in cosmochemistry and biological experiments involving isotopic labelling (see sections 'Applications in cosmochemistry' and 'Applications in biological geochemistry'), such small effects are not important because the isotopic effects in the samples are commonly much larger. For terrestrial non-labelled materials, however, the total isotopic variation for a given element in a given sample, or set of samples, is often only at the per mil level, in which case, corrections due to IMF and matrix effects can be extremely important.

Two types of detectors are commonly used to record secondary ion intensities: electron multipliers and Faraday cups. Electron multipliers are usually used in the pulse-counting mode in which each arriving ion produces an electrical pulse, which is then amplified and registered. Electron multipliers have a large dynamic range, permitting measurement of ion count rates between < 1 and 10^6 cps. Count rates must be corrected for detector dead time (typically 20–40 ns). For typical NanoSIMS applications (see below), count rates of major isotopes can easily be on the order of 100000 cps (~ 1 pA primary current). From the relationship

$$C_{true} = C_{meas} \times \exp(\tau \times C_{meas}) \approx C_{meas} \times (1 + \tau \times C_{meas}) \quad (2)$$

where C_{meas} is the measured count rate, C_{true} the true count rate and τ the detector dead time, it follows that count rate corrections of major isotopes are something on the order of a few per mil ($1 + 4 \times 10^{-8} \times 10^5 = 1.004$). For precise isotope measurements, it is thus important that the dead time of the detector system is well known.

A much more serious limitation of measurements by electron multipliers is the effect of quasi-simultaneous arrivals (QSA; Slodzian *et al.* 2001). This effect occurs when a single impacting primary ion has a high probability of producing multiple secondary ions of the same species that are then registered as a single event by the electron multiplier. QSA leads to a discrimination against the major isotope, and a measured isotope ratio R_{meas} (minor over major isotope) will deviate from the true isotope ratio R_{true} according to:

$$R_{meas} = R_{true} \times (1 + a \times K), \quad (3)$$

where K is the ratio of secondary over primary ions and a is a constant with a theoretical value of 0.5 (Slodzian *et al.* 2001). For SIMS instruments with high transmission, such as the NanoSIMS, the QSA corrections can be quite large. For example, the K parameter may reach values in excess of 0.1 for sulfur isotope measurements (Slodzian *et al.* 2004), leading to a QSA correction on the order of 5%.

To complicate matters further, Slodzian *et al.* (2004) recognised that the true value of parameter a can deviate significantly from the theoretical value of 0.5. Recently, Hillion *et al.* (2008) reported values of a for different elements in a set of different samples and found $a \approx 0.75$ for sulfur and oxygen, $a \approx 1$ for carbon and $a \approx 0.6$ for silicon. These numbers are subject to large uncertainties, and the QSA correction is hence a potential source of large uncertainties for isotope measurements of elements with high useful yields, such as C, N (measured as CN^-), O, Si and S. To minimise uncertainties introduced by QSA corrections, it is important to measure reference materials of essentially the same matrix under the same measurement conditions (i.e., with the same K value) and to reduce the spectrometer transmission (which reduces the value of K and thus the measurement bias) to yet acceptable count rates. The QSA effect can be avoided altogether when secondary ion intensities are recorded with Faraday cups instead of electron multipliers, because Faraday cups measure secondary ion currents directly. However, Faraday cup measurements require that the secondary ion beam intensity is substantially higher than background corrections due to electronic noise in the amplifiers, which can be significant. In practice, precise Faraday cup measurements require count rates in excess of ~ 10^7 cps. In such a case, however, the use of Faraday cups permits isotope measurements with sub-per mil precision. The required high secondary ion signals can be achieved only with comparatively high primary currents (several nA) at the expense of spatial resolution.

Design and ion optics of the NanoSIMS instrument

In the following, we turn to more technical aspects of the NanoSIMS instrument. The NanoSIMS ion optics is based on a design by Georges Slodzian, and the instrument was developed by a team led by Francois Hillion at Cameca. Details are described in Hillion *et al.* (1993) and Slodzian *et al.* (1993). Technically speaking, the NanoSIMS is a dynamic, double-focussing, magnetic-sector, multi-collecting ion probe. The instrument is built in two basic configurations, the NanoSIMS 50 (NS50; Figure 2) and NanoSIMS 50L (NS50L). These two models differ in that the NS50L has a larger magnet and modified detector ion optics, which permits the simultaneous measurements of up to seven different isotopes or molecular species, compared with five for the NS50. The basic NanoSIMS design and the ion optical elements are illustrated in Figure 3, and selected characteristics are given in Table 1.

The most important fundamental property of the NanoSIMS instrument, which distinguishes it from other types of magnetic-sector SIMS instruments, is its ability to produce a

small primary beam diameter (defined as encompassing 68% of the primary beam flux assuming a Gaussian density distribution) on the surface of a flat sample. Minimum beam diameters are ~ 50 nm for primary Cs^+ ions and ~ 200 nm for primary O^- ions, respectively, under optimal tuning conditions.

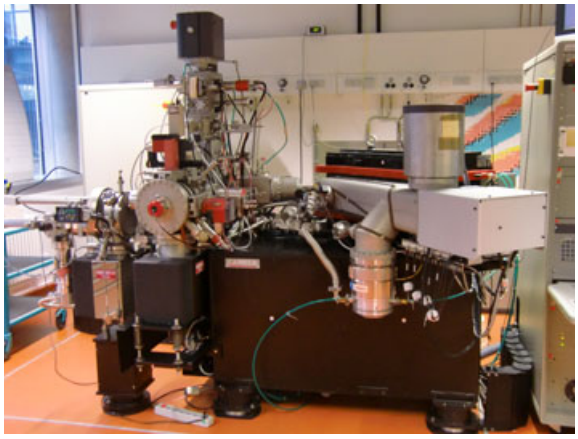

Figure 2. The Cameca NanoSIMS 50 ion probe at the Max Planck Institute for Chemistry.

The ion sources and the primary ion beam: Starting with the creation of primary ions, the NanoSIMS offers a choice between two primary ion sources: a $CsCO_3$ source that allows the formation of a beam of positive caesium ions (Cs^+) and a duoplasmatron source that forms a beam of negatively (and positively) charged oxygen ions. The most frequently used species is O^-, which is selected from other species (notably NO^-, O_2^- and O_3^-) with a Wien filter. Primary ions are accelerated from a potential of +/- 8 kV at the source, to a potential of -/+ 8 kV at the surface of the sample, thus impacting the sample with an energy of 16 keV.

From the source, an image (crossover image for Cs or image of plasma located close to the extraction hole for O) of the primary ion beam is demagnified by three electrostatic lenses (Figure 3: L0, L1 and L2). The primary beam then

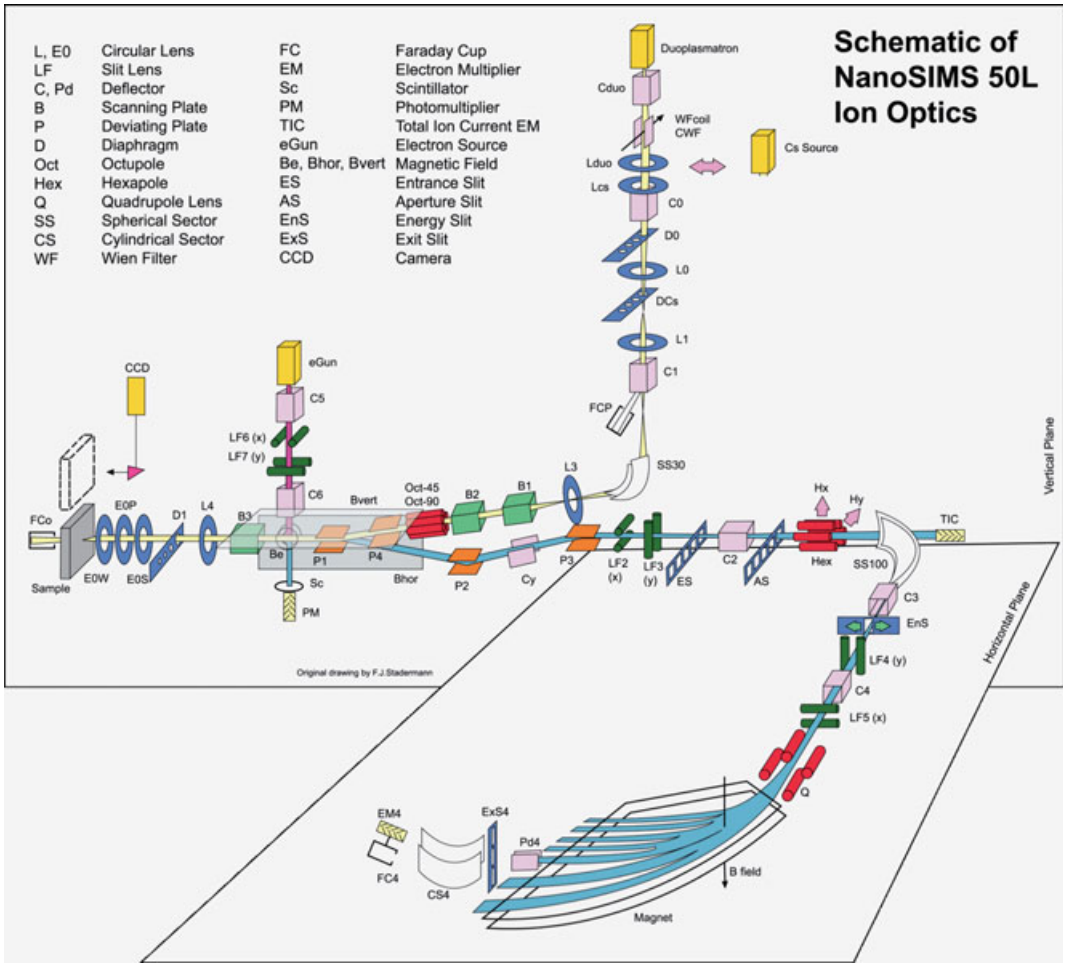

Figure 3. Schematic of the ion optics of the NanoSIMS 50 (Picture credit: François Hillion and Frank Stadermann).

Table 1.
Cameca NanoSIMS 50/50L characteristics

Item[a]	Characteristics	
Primary ions	Cs^+	O^-
Source voltage	+8 kV	-8 kV
Source current (typical, D0 open)	30–50 nA	500–1000 nA
Probe current (range)	0.1 pA … > 5 nA	0.1 pA … > 5 nA
Probe current (D1 = 150 μm, L0/L1 = 0 V)	1 pA	10 pA[b]
Beam size (routine conditions)	100 nm (1 pA)	400 nm (10 pA)
Beam size (smallest)	< 50 nm (0.3 pA)	200 nm (< 1 pA)
Raster size (maximum)	200 × 200 μm^2	200 × 200 μm^2
Secondary ions	Negative	Positive
Extraction voltage	-8 kV	+8 kV
Transmission for Si isotope measurement	> 50%	> 50%
Multi-collection system	NanoSIMS 50	NanoSIMS 50L
Number of detectors	5	7
Mass dispersion (M_{max}/M_{min})	13.2	21
Mass separation between detectors[c]	$M_{max}/30$	$M_{max}/58$
Detector characteristics		
EM dead time (standard setting)	44 ns	
EM background	< 0.01 cps	
FC noise (low-noise electrometer)	< 5 × 10^{-16} A	

[a] D0, D1: Apertures (*cf.* Figure 3); L0, L1: Lenses (*cf.* Figure 3); M_{max}: Mass at largest possible radius; M_{min}: Mass at lowest possible radius; EM: Electron multiplier; FC: Faraday cup.
[b] D0 = 200 μm, Wien filter on (*cf.* Figure 3).
[c] At largest radius (528 mm for NS50, 680 mm for NS50L).

enters an electrostatic spherical sector (SS30) that turns the beam 78°. The beam is then guided onto the target; it passes an octopole, which is used to correct astigmatism, it is deflected by the P1 plates to hit the sample surface perpendicularly, and its angular distribution is trimmed by an aperture of variable size (D1), after which it is focused by the EOP lens to its final spot size on the sample surface (Figure 3). Three sets of scanning plates (B1, B2 and B3) allow the primary beam to be displaced horizontally across the sample surface, in order to create a raster with a maximum area of 200 × 200 μm^2. This raster allows ion images to be created (see Ion imaging). Ion yields are largely constant across relatively large areas in ion images. For example, the useful yield of Si^- from a Si wafer does not change by more than 5% within a field of 50 × 50 μm^2 (unpublished, MPI Mainz).

The fact that the primary beam hits the sample surface with normal incidence is a unique feature of the NanoSIMS. Because the extraction of secondary ions also occurs coaxially, the same ion optical system (immersion lens consisting of EOW, EOP, EOS, L4) can be used to extract and begin focussing the secondary ions. This permits the ion optical elements to be placed much closer to the sample surface (the nominal distance is 400 μm), compared with conventional ion probe instruments, where the primary ion beam strikes the sample obliquely and the ion optics focussing the primary beam is at a distance on the order of centimetre from the sample surface. The short distance between sample and the probe-forming lens in the NanoSIMS results in a reduction in focal length and aberrations and a much smaller probe size (beam spot) on the sample surface for a given primary current. At the same time, this geometry results in the secondary ions experiencing a strong electrostatic extraction field that favours high useful yields. Shadowing effects from topography on the sample surface, which can reduce the useful yield, are also minimised with this geometry. Useful yields of 2.5–3% have been measured for C^- and C_2^- from a polished vitreous carbon sample at full spectrometer transmission (Hillion *et al.* 1995). About the same useful yields were obtained for Si^- from a Si wafer (F. Hillion, personal communication).

Because of the short distance between the immersion lens and the sample, it is not possible to do real-time viewing of the sample in an optical microscope. Nevertheless, a high-resolution (3 μm) reflected light image of the sample can be viewed if the sample is moved away from its analysis position.

The aperture D1 limits the angular dispersion of the primary beam and is therefore used to control primary beam current and probe size. At the same time, D1 acts as a field aperture for the extracted secondary ions. Because of the

coaxial ion optics, polarities of primary and secondary ions must be of opposite sign. In practice, this is no limitation because the use of Cs^+ primary ions favours formation of negative secondary ions and the use of O^- primary ions favours the formation of positive secondary ions.

The secondary ion beam and mass resolution: Secondary ions are transferred to a double-focussing mass spectrometer by several circular lenses (EOW, EOS, L4) and two slit lenses (LF2, LF3) that shape the secondary ions into a beam with a rectangular cross-section before it enters the mass spectrometer through the entrance slit (ES). Two external coils are used to compensate for the mass fractionation at the ES. A set of deflection plates (P1) separates secondary from the oppositely charged primary ions. Another set of deflection plates allow the secondary beam to be centred on the ES, which trims the size and lateral energy distribution of the secondary ion beam. An aperture slit (AS) of variable width again trims the secondary beam to limit its angular dispersion after which a hexapole minimises second-order angular aberrations further. The beam then enters the electrostatic spherical analyser (SS100), where the secondary ions are dispersed according to energy and deviated onto an energy slit (EnS) of variable width, which can be used to trim the beam and reduce its energy bandwidth. Before the secondary beam enters the magnet, it passes through two slit lenses (LF4 and LF5) and a quadruple lens (Q), which allow angular and energy focussing across the entire focal plane of the magnet, where the detectors are situated.

Mass separation occurs in a laminated magnet. Either five or seven detectors are placed in the focal plane of the magnet, in the case of NS50 or NS50L instruments, respectively. Four and six of these, respectively, are moveable on trolleys. Mass dispersion between the highest and lowest possible mass is 13.2 (NS50) and 21 (NS50L), respectively. The smallest possible mass separation between two detectors at highest radius (r_{max} = 528 mm for NS50 and r_{max} = 680 mm for NS50L) is about Mass/30 (NS50) and Mass/58 (NS50L). In practice, optimised positioning of detector end-switches permits some increase in this detector separation limit. For instance, with the NS50 at Max Planck Institute for Chemistry, it is possible to measure all S isotopes (M = 32, 33, 34 and 36) simultaneously in adjacent detectors (Sinha *et al.* 2008). The higher mass separation limit in the NS50L results from the larger magnet and because each ion detector is equipped with a small electrostatic analyser (CS) to reorient the secondary ion beams. Rectangular exit slits are placed in front of each detector. Depending on the NanoSIMS configuration, the detector trolleys can be equipped with either a Hamamatsu miniature electron multiplier, which counts secondary ions individually, or a Faraday cup, which measures the current of the beam of secondary ions. Exchanging between electron multipliers and Faraday cups currently requires venting and complete removal of the multi-collection system. A new design of the multi-collection will overcome this problem in the near future.

Mass resolution is defined as $m/\Delta m$, where m is the (mean) mass and Δm the mass difference between two species, A and B, to be separated. On the NanoSIMS, the achievable MRP depends on the choice of the entrance and exit slits. To first order, that is, ignoring aberrations, the MRP is calculated here as:

$$\mathrm{MRP}_1 = \frac{1}{2} \times \frac{r}{(G \times \mathrm{ES} + \mathrm{ExS})}, \quad (4)$$

where r is the turning radius of mass m in the magnet, G is the magnification of the entrance slit image in the exit slit plane ($\approx r/r_{max}$), ES is the width of the entrance slit and ExS is the width of the exit slit. In a mass spectrum, recorded by changing the deflection plate voltage in front of the exit slit (deflector Pd in Figure 3), the two species A and B appear as separated peaks if $\mathrm{MRP}_1 > m/\Delta m$ (*cf.* Figure 4). Each detector on the NanoSIMS is equipped with three exit slits. On the NS50 instrument at Max Planck Institute for Chemistry, the exit slits are 25, 50 and 80 μm wide, respectively. For ES = 10 μm (the smallest available ES size) and r_{max} = 528 mm, MRP_1 varies between 2900 and 7500 at r_{max} and between 1800 and 4900 at r = 300 mm, depending on the exit slit size. Note that Cameca uses a different definition for MRP, namely

$$\mathrm{MRP}_2 = \frac{1}{4} \times \frac{r}{L} \quad (5)$$

where L is the width of the portion of the mass peak between 10% and 90% of the maximum intensity, a measure for the steepness of the peak flanks (which is independent of the exit slit width). For $\mathrm{MRP}_2 > m/\Delta m$, species A and B appear as separated mass lines in the plane of the exit slit, but not necessarily in recorded mass spectra. With this approach, the MRP is usually above 10000 for the smallest ES.

Auxiliary measurement tools: The NanoSIMS is equipped with additional tools to support the measurement and tuning. A total ion current (TIC) electron multiplier, placed close to the electrostatic sector, can be used to record non-mass-filtered secondary ion signals. An electron flood gun enables charge compensation for the analysis of insulating samples, for example, large olivine or corundum grains, and an electron detector (scintillator/photomultiplier) permits acquisition of secondary electron images in the mode where negative secondary ions are analysed.

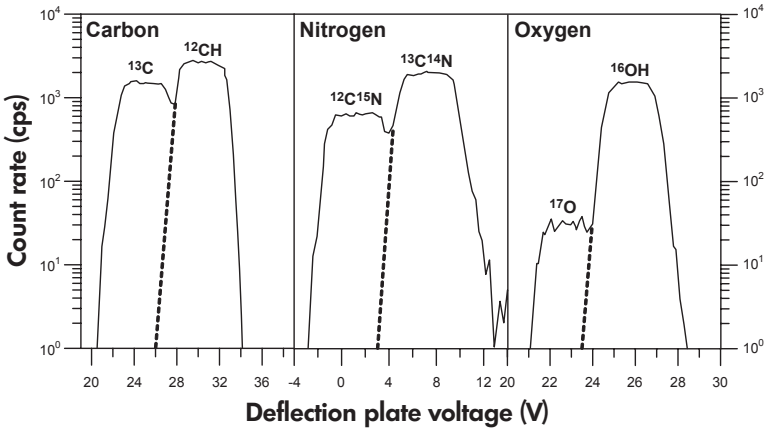

Figure 4. High-resolution mass spectra for mass regions 13, 27 and 17. Varying the voltage on the deflection plates in front of each exit slit allows for the scanning of a small portion of the mass spectrum. Entrance/exit slit settings: 20/50 μm (mass 13), 20/50 μm (mass 27) and 10/25 μm (mass 17). A difference between two deflection plate voltages ΔV can be approximately converted to a mass difference by Δm (amu) = $k^*\Delta V$ (k = 0.000749 for mass 13, k = 0.00104 for mass 27, k = 0.00103 for mass 17).

Vacuum and sample transfer system: The required ultra-high vacuum in the NanoSIMS is achieved by several turbo-molecular and ion pumps and a Ti sublimation pump. At the location of the sample, the vacuum should be maintained at the 10^{-10} hPa level. This restricts the analysis to low-degassing samples and requires that geological thin sections should be prepared only with selected resins and stored for a sufficiently long time (up to several days) in the airlock/vessel system prior to analysis. The vessel is located between the airlock, where samples are introduced into the NanoSIMS, and the analysis chamber and hosts a carousel that can take up eight ~ 2 inch-sized sample holders. Each sample holder usually can host 1 inch-, half inch- and 1 cm-sized samples in various combinations, but user-defined designs for specific applications are possible as well.

Isotope measurements

An important class of NanoSIMS applications are isotope measurements of the low and intermediate atomic number elements at high spatial resolution. There is a natural limitation on achievable precision, simply because of the relatively low number of atoms available within an analysed volume. Consider a particle of pure carbon (e.g., graphite or diamond), on which a C isotopic measurement is to be conducted. Assuming that the cubic particle has a density of 2.2 g cm^{-3} and a size of 100 nm, it contains about 10^8 C atoms (Table 2). If the NanoSIMS delivers a 1 pA primary beam of Cs^+ (6×10^6 Cs^+ ions per second) to a surface area of 0.01 μm^2 (i.e., 100 × 100 nm^2) on this sample and assuming a sputter yield of 5, it will take just a few seconds to sputter away all ~ 10^8 C atoms, and the particle no longer exists. With an assumed ionisation yield of 1%, an isotopic abundance of ^{13}C of ~ 1% (Table 3) and a transmission and detection efficiency of 30%, the number of ^{13}C atoms detected from this particle will be about 3300. This means that the relative counting statistical uncertainty on the $^{13}C/^{12}C$ ratio, which is determined by a Poisson distribution, is 1/sqrt(3300) × 100%, or about 2%. Table 3 provides other examples of the theoretical counting statistical

Table 2.
Achievable precision for C isotopic measurements with the NanoSIMS

Particle size (nm)	N_{atoms}[a]	N_{ions}[b]	$N_{detected}$[c]	$^{13}C_{detected}$[d]	$\Delta^{13}C/^{12}C$[e] (‰)
100	1.1×10^8	1.1×10^6	3.3×10^5	3.3×10^3	17
500	1.4×10^{10}	1.4×10^8	4.2×10^7	4.2×10^5	1.5
1000	1.1×10^{11}	1.1×10^9	3.3×10^8	3.3×10^6	0.6

[a] Cubic carbon particle, ρ = 2.2 g cm^{-3}, N_{atoms} = 110 × V [nm^3].
[b] Ionisation yield of 1% assumed.
[c] Spectrometer transmission/detection efficiency of 30% assumed.
[d] For VPDB composition.
[e] Counting statistical uncertainty.

uncertainty on a measured $^{13}C/^{12}C$ ratio for larger sample sizes. Only for C particles with volumes of ~ 1 μm^3 or more will a measurement of $^{13}C/^{12}C$ in principle be possible with a precision better than 1 per mil. In situations where the element of choice is present in much lower abundances, has lower ionisation yield or has lower abundance of the minor isotope (e.g., H, N and O, *cf.* Table 3), the situation is even less favourable.

Measurement precision is further limited due to QSA correction, adjustments of exit slit deflection plate voltages during measurements (used to compensate for drift in peak position) and sensitivity of IMF to sample topography and charging. QSA corrections, which only affect measurements with electron multipliers, can be very large for certain elements, and taking the uncertainty and spot-to-spot variation of this correction into account, in practice, isotope measurements with electron multipliers can hardly achieve a precision (1*s*) of better than ~ 1–2‰ (Rasmussen *et al.* 2008, Kilburn and Wacey 2011). For many applications in cosmochemistry (see section 'Applications in cosmochemistry') and biological geochemistry (see section 'Applications in biological geochemistry'), precision (and measurement accuracy) at the several per mil or even per cent level is acceptable and presents no serious limitation. Some applications in geochemistry, however, require sub-per mil precision (and measurement accuracy) for isotope measurements. Sub-per mil precision is possible with micrometre-scale lateral resolution when Faraday cups are used. Test measurements on the NS50 at the Max Planck Institute for Chemistry (unpublished), made with two Faraday cups connected to low-noise electrometers, yielded precisions (1*s*) of 0.1‰ for $^{30}Si/^{28}Si$ on a perfect Si wafer and with a primary beam spot size of 10 × 10 μm^2 (20 spots), 0.2‰ for $^{34}S/^{32}S$ on the Canyon Diablo Troilite (spot size 10 × 10 μm^2, 8 spots) and 0.4‰ for $^{18}O/^{16}O$ on the San Carlos Olivine (spot size 5 × 5 μm^2, 8 spots). However, high-precision isotopic determination of a 'natural' sample or rock consisting of multiple, chemically zoned minerals, conducting or non-conducting, with polishing surface topography due to hardness differences is a different challenge.

Table 3.
Reference values for isotope ratios of selected low and intermediate atomic number elements

Isotope ratio	Reference material	Reference value
D/H	VSMOW	0.00015576
$^{13}C/^{12}C$	VPDB	0.0111796
$^{15}N/^{15}N$	Air	0.0036765
$^{17}O/^{16}O$	VSMOW	0.0003799
$^{18}O/^{16}O$	VSMOW	0.0020052
$^{25}Mg/^{24}Mg$	NIST SRM 980	0.12663
$^{26}Mg/^{24}Mg$	NIST SRM 980	0.13932
$^{29}Si/^{28}Si$	NIST NBS 28	0.050804
$^{30}Si/^{28}Si$	NIST NBS 28	0.033532
$^{33}S/^{32}S$	VCDT	0.0078773
$^{34}S/^{32}S$	VCDT	0.0441626
$^{36}S/^{32}S$	VCDT	0.0001535

Data were calculated from isotope abundances given in Coplen *et al.* (2006).

In the following, we will briefly describe some details of isotope measurements for selected elements with the NanoSIMS. Table 4 lists the most important isobaric interferences, required MRP and typical settings for entrance and exit slits to achieve this.

Hydrogen: Hydrogen isotopes can be measured as positive and negative secondary ions. The advantage of measuring negative secondary ions is that the H_2^- interference is much less intense than the D^- signal (Zinner 1989), and use of Cs^+ primary ions gives a better spatial resolution. The separation of H_2 from D requires a MRP of 1300 (Table 4), which is easily achieved in the NanoSIMS even at full transmission. Hydrogen and D can be measured in multi-collection; if C or heavier elements are measured simultaneously in the NS 50, then a combination of multi-collection measurement and magnetic peak-switching may have to be used because of mass dispersion constraints (Duprat *et al.* 2010). Because the mass dispersion is larger in the NS50L, this instrument is capable of measuring H, C and O isotopes simultaneously in multi-collection.

Carbon: Carbon isotopes are measured as negative secondary ions and usually in multi-collection mode along with other isotopes, for example, of CN (Busemann *et al.* 2009), O (Stadermann *et al.* 2005a) or Si (Hoppe *et al.* 2010). Measurement of ^{13}C requires a MRP of about 3000 (Table 4) to separate ^{12}CH from ^{13}C, which is easily achieved in the NanoSIMS (Figure 4). Contributions from the tail of the ^{12}CH peak to ^{13}C are typically < 1‰ of the ^{13}C signal. Note that the C isotopic ratio can also be measured as $^{13}C^{12}C/^{12}C_2$, which requires a MRP of 5600, and as $^{13}C^{14}N/^{12}C^{14}N$, which requires a mass resolution of 4300, if the $^{11}B^{16}O$ interference can be ignored (Table 4).

Nitrogen: Nitrogen isotopic compositions can be measured only under special circumstances. The positive secondary ion yield of N is very low, and negative secondary ions do not form at all. However, in the presence of carbon, N can be measured as CN^- with Cs^+ primary ions (Zinner 1989). Depending on the amount of C present, the CN^- signal can be very strong and $^{15}N/^{14}N$ can be inferred

Table 4.
Isotope measurements of selected low and intermediate atomic number elements by NanoSIMS: isobaric interferences, required MRP and typical entrance and exit slit settings

Element	Critical isotope	Isobaric interferences	MRP	Typical settings (ES/ExS)
Hydrogen	D	H_2	1300	30–40 μm/80 μm
Carbon	^{13}C	^{12}CH	2900	20 μm/50 μm
	$^{13}C^{12}C$	$^{12}C_2H$	5600	10 μm/25 μm
Nitrogen[a]	$^{12}C^{15}N$	$^{13}C^{14}N$	4300	10–20 μm/25–50 μm
		$^{11}B^{16}O$	6600	10–20 μm/25–50 μm[b]
Oxygen	^{17}O	^{16}OH	4700	10 μm/25 μm
Silicon	^{29}Si	^{28}SiH	3500	20–30 μm/50–80 μm
Sulfur	^{33}S	^{32}SH	3900	20 μm/50 μm
	^{36}S	$^{12}C_3$	1100	20 μm/80 μm

[a] Measured as CN^-.
[b] Measurement of $^{12}C^{15}N$ to the left of peak centre.

from $^{12}C^{15}N/^{12}C^{14}N$. Important isobaric interferences are $^{13}C^{14}N$ (Figure 4) and sometimes $^{11}B^{16}O$. While $^{13}C^{14}N$ can be easily separated at a MRP of 4300 (Table 4), $^{11}B^{16}O$ is more difficult to separate as the required MRP of 6600 is at the limit of what can be achieved with the NanoSIMS. In a typical measurement set-up (ES = 20 μm, ExS = 50 μm), no proper separation is achieved between the $^{12}C^{15}N^-$ and $^{11}B^{16}O^-$ peaks, but recording the $^{12}C^{15}N$ intensity at ~ 1 V to the left of the $^{12}C^{15}N$ peak centre (Figure 4) ensures a proper measurement of this isotope.

Oxygen: Oxygen isotopes are measured as negative secondary ions in multi-collection. Major problems are the low abundances of ^{17}O and ^{18}O (Table 3) and the ^{16}OH interference at mass 17 that can be orders of magnitude higher than ^{17}O (Figure 4). The required MRP to separate ^{16}OH from ^{17}O is 4700, which is easily achieved with the NanoSIMS (Table 4). However, contributions from the tail of the ^{16}OH peak to ^{17}O must be considered and can account for several per mil of the ^{17}O signal. For ^{18}O, the situation is unproblematic. The $^{16}OH_2$ interference is relatively small, and its separation requires a MRP of only 1600. Also the ^{17}OH interference is well separated, and since the $^{17}OH/^{18}O$ ratio is typically only on the order of 10^{-3} to 10^{-2}, its tail contribution can be neglected.

Silicon: Silicon can be measured either as positive or negative secondary ions. Usually, negative secondary ions are preferred in the NanoSIMS as in this case the Cs source can be used, which provides a higher spatial resolution. All three Si isotopes can be measured simultaneously in multi-collection. The separation of the interference ^{28}SiH to ^{29}Si requires a MRP of 3500, which is easy to achieve in the NanoSIMS, and tail contributions can usually be neglected. Measurement of ^{30}Si is unproblematic.

Sulfur: Sulfur isotopes are measured as negative secondary ions. All four S isotopes, ^{32}S, ^{33}S, ^{34}S and ^{36}S, can be measured simultaneously in multi-collection, not only with the NS50L but under optimised conditions also with the NS50. The most problematic isotopes are ^{33}S and ^{36}S. To separate ^{33}S from ^{32}SH, a MRP of 3900 is required; ^{32}SH tail contributions to ^{33}S are usually in the sub-per mil range. Nominal separation of potential isobaric interferences for ^{36}S is unproblematic (Table 4); however, because of the very low abundance of ^{36}S (Table 3), tail contributions of other peaks in the mass 36 region are a serious concern. Important to mention in this respect is the tail of $^{12}C_3$, which can significantly contribute to ^{36}S, as shown by Nagashima *et al.* (2008), and which must be carefully monitored and, if present, subtracted from the recorded ^{36}S ion signal.

Other elements: Isotope measurements of several other elements have been reported, including Li, B, Mg, K, Ca, Ti, Cr, Fe, Ni and Pb (see sections 'Applications in cosmochemistry' and 'Biological geochemistry'). In contrast to the elements described above, which are measured with Cs^+ primary ions, all these elements are measured with O^- primary ions, that is, usually at lower spatial resolution. While multi-collection measurements are possible for Li, B and Mg on the NS50/50L, isotope measurements of Ca, Ti, Cr and Fe in multi-collection with static magnetic field are possible only on the NS50L; on the NS50, the combination of multi-collection and peak-jumping mode has to be used.

Ion imaging

By rastering the primary ion beam over the sample, isotope distribution images can be acquired. This technique, 'ion imaging', is widely used on the NanoSIMS. Ion images consist of up to 2048 × 2048 pixels, and sizes are typically

between 1 × 1 and 50 × 50 μm^2. Integration times per pixel are typically in the ms range. Images are usually subdivided into a number of planes to allow for correction of image shifts, for example, due to sample stage movement. Image resolution is determined to first order by the primary ion beam diameter; for Cs^+, it is 50–100 nm for a beam current of < 1 pA, and for O^-, it is 200–400 nm for < 10 pA (see Table 1). The ion imaging technique can create isotope and element distribution maps from which isotope and elemental ratio images can be calculated. In this way, it is possible to search for objects with specific isotopic fingerprints, for example, presolar grains (see section 'Applications in cosmochemistry'). An example is shown in Figure 5 where ~ 300 nm-sized presolar silicates stand out by their strong enrichment in ^{17}O. The application of ion imaging is restricted to measurements with electron multipliers because the response time of Faraday cups is too long.

NanoSIMS versus other SIMS instruments/techniques

Besides the NanoSIMS, there are several other types of SIMS instruments/techniques that are widely used in cosmo- and geochemistry: Time-of-Flight SIMS (ToF-SIMS), Cameca's 'all-rounder' IMSxf (x = 3…7) ion probe and the large-geometry ion probes Cameca IMS1270/1280 and SHRIMP I/II/RG. Advantages of ToF-SIMS are parallel detection of all secondary ions with one polarity, sub-micrometre spatial resolution, little sample destruction and preservation and analysis of organic molecules (Stephan 2001). A disadvantage is the difficulty of measuring isotopic compositions because of low ion signals and limited mass resolution. The Cameca IMSxf series ion probe has been used for a multitude of applications. A major advantage of this instrument is its low price compared with other ion probes. Disadvantages are a lower sensitivity than in other instruments and a lower spatial resolution (~ 1 μm) than in the NanoSIMS. The SHRIMP I/II/RG ion probe is primarily used for U–Pb dating of zircons (Ireland 1995), a topic that has been only rarely addressed with the NanoSIMS (Stern *et al.* 2005). There remains the Cameca IMS1270/1280 ion probe, which we will compare with the NanoSIMS in some detail in the following.

While the NanoSIMS 50/50L ion probe was designed for high spatial resolution isotope/element measurements, the strength of the IMS1270/1280 ion probe is high-precision isotope measurements. Both instruments are characterised by a high transmission for secondary ions (Figure 6), at a level of several 10% up to a MRP of about 7000 in the NanoSIMS (close to the limit of what can be achieved with a 10 μm entrance and 25 μm exit slit) and a MRP of > 10000 in the IMS1270/1280. This is important because (i) high spatial resolution measurements are made with low primary ion currents, resulting in relatively low secondary ion intensities and (ii) high-precision isotope measurements require high secondary ion signals. Regarding absolute sensitivities, or useful yields, at full transmission, reliable and meaningful comparisons between the NanoSIMS (see ion sources and the primary ion beam) and the IMS1270/1280 ion probes are not available to the best of our knowledge. Nevertheless, it can be expected that useful yields at full transmission will not differ dramatically between these two types of instruments.

Both types of instrument are capable of performing multi-collection measurements. With the IMS1270/1280 ion probe, it is possible to get spot-to-spot repeatability (1*s*) close to 0.1‰ on geological materials, for example, for $^{18}O/^{16}O$ measurements at a scale ≥ 10 μm (Kita *et al.* 2011). This has not been achieved yet with the NanoSIMS, possibly largely due to the strong gradient of the electrostatic field between sample and EOW, which makes the IMF very sensitive to small changes in topography. With regard to

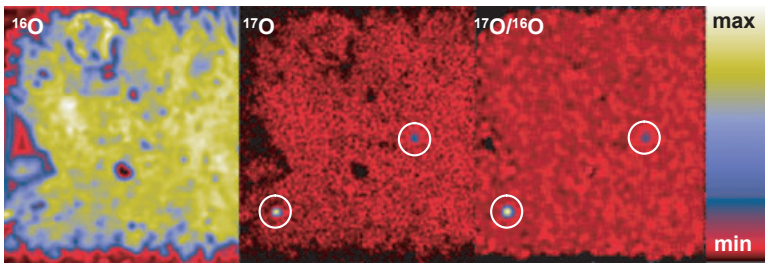

Figure 5. Negative secondary ion images of ^{16}O and ^{17}O and the $^{17}O/^{16}O$ ratio of a 9 × 9 μm^2-sized region in the matrix of the Acfer 094 meteorite. Colour scale (low to high intensity): black–red–blue–yellow–white. Two ~ 300 nm-sized presolar silicate grains (white circles) stand out as hot spots in the ^{17}O and $^{17}O/^{16}O$ images. From Hoppe *et al.* (2005).

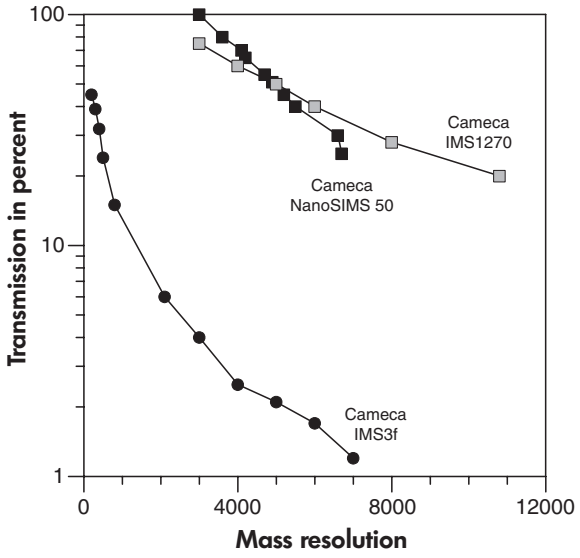

Figure 6. Transmission (relative to the secondary ion signal when all slits in the mass spectrometer are open) as a function of MRP in three SIMS instruments for $^{12}C^-$ secondary ions emitted under Cs^+ bombardment from a SiC disc. NanoSIMS data courtesy François Hillion (Cameca, Paris), IMS1270 data courtesy of Kevin McKeegan (UCLA) and IMS3f data courtesy of Ernst Zinner (Washington University, St. Louis, MO, USA).

spatial resolution on the sample surface, the NanoSIMS has a smallest achievable primary ion beam (Cs^+, O^-) diameter that is at least a factor of 5 smaller than that in the IMS12870/1280. Usually, the IMS1270/1280 instruments are operated with beam spots tens of micrometre in diameter.

Applications in cosmochemistry

The NanoSIMS ion probe has been used to study a variety of cosmochemical problems. Samples suitable for NanoSIMS studies are conventional thin (or thick) sections of, for example, meteorites, individual, micro- or sub-micrometre-sized grains on flat surfaces, for example, presolar SiC grains dispersed on clean Au foils, or microtome sections or sections prepared by the focused ion beam (FIB) technique. Microtome or FIB sections permit to combine NanoSIMS with transmission electron microscopy (TEM) studies, which enable co-ordinated mineralogical and isotopic studies of materials *in situ* at sub-micrometre scales. This has resulted in several important advances, for example, the identification of primordial organic nanoglobules (Nakamura-Messenger *et al.* 2006, see section on Extraterrestrial organics) and the discovery of presolar silicates in interplanetary dust particles (IDPs; Messenger *et al.* 2003; see section on Presolar grains).

Presolar grains

The study of so-called presolar grains was a driving force for major improvements in the initial design of the NanoSIMS. Presolar grains are sub-micrometre- and micrometre-sized refractory dust grains that are found in small quantities, at a level of ng g^{-1} to hundreds of µg g^{-1}, in certain types of solar system materials, such as primitive meteorites, IDPs and matter from comet 81/P Wild 2 returned by NASA's Stardust mission. Presolar grains are older than our solar system and represent a sample of stardust that can be analysed in the laboratory for isotopic compositions and mineralogy (Zinner 2007, Hoppe 2008). These pristine grains are formed in the winds of asymptotic giant branch (AGB) stars and in the ejecta of supernova (SN) and nova explosions. The study of the isotopic compositions of major and minor elements in single presolar grains has provided a wealth of astrophysical information, for example, on stellar nucleosynthesis and evolution, on mixing in SN ejecta, grain growth in stellar environments, on processes in the interstellar medium (ISM) and on the inventory of stars that contributed dust to our solar system. Presolar grains exhibit large isotope anomalies, which range over many orders of magnitude for the CNO elements and which are at the per cent level or larger for intermediate-mass elements. The sub-micrometre size of most presolar grains and their large isotope anomalies make the NanoSIMS the perfect choice for isotope measurements.

Presolar silicates: One of the most important discoveries in the field of presolar grain research in recent years was the identification of presolar silicates, first in an IDP (Messenger *et al.* 2003) and later also in primitive meteorites (Mostefaoui and Hoppe 2004, Nguyen and Zinner 2004) by NanoSIMS oxygen ion imaging (see Ion imaging and Figure 5). Presolar silicates were also identified in the IMS1270 ion probe equipped with a SCAPS detector (Nagashima *et al.* 2004); however, because of lower spatial resolution, this technique reliably identifies only the largest presolar grains (> 500 nm) or those with comparatively large isotope anomalies for which contributions from surrounding isotopically normal matter do not completely erase the isotope anomaly. In contrast to other presolar minerals, for example, SiC, which was already discovered more than a decade earlier (Bernatowicz *et al.* 1987), presolar silicates cannot be chemically separated from meteorites, and only the application of high-resolution ion imaging techniques made their discovery possible. Hundreds of presolar silicates have been found to date.

Presolar oxides have been studied in detail by conventional SIMS since the middle of the 1990s. Based on their O isotopic compositions, presolar oxides are divided into four

distinct groups (Nittler *et al.* 1997, 2008). In general, presolar silicates show O isotope systematics similar to presolar oxides (Figure 7). Noticeable exceptions are the extreme ^{18}O enrichment of a SN olivine (Messenger *et al.* 2005) and the higher $^{18}O/^{16}O$ ratios of Group 2 silicate grains. The latter, however, is likely to be an experimental bias because measured $^{18}O/^{16}O$ ratios of 200–300 nm-sized grains, the typical size of presolar silicates, from thin sections might be shifted towards higher values because of dilution effects due to contributions from surrounding matter with normal isotopic composition (Nguyen *et al.* 2007). This must be taken into account even for a primary ion beam size of nominally 100 nm diameter, because 5% of the beam intensity will be outside of a circle with 200 nm diameter. This of course will also affect $^{17}O/^{16}O$ ratios, but lower than solar ratios will be more affected than higher than solar ratios. This can be easily seen from an example for a presolar grain with $^{17}O/^{16}O = 7.6 \times 10^{-4}$ (factor of 2 enrichment in ^{17}O) and $^{18}O/^{16}O = 2 \times 10^{-5}$ (factor of 100 depletion in ^{18}O). Dilution with 10% isotopically normal matter gives $^{17}O/^{16}O = 7.3 \times 10^{-4}$ (i.e., 4% change) and $^{18}O/^{16}O = 2 \times 10^{-4}$ (i.e., factor of 10 change).

Apart from meteoritic diamonds, whose origin is still a matter of debate, presolar silicates represent the most abundant presolar phase. Abundances of presolar silicates vary strongly among different primitive solar system materials (Figure 8), the fingerprint of parent body processes (thermal and aqueous alteration) and possibly also abundance variations in the solar nebula. Highest abundances are usually observed in primitive IDPs, which have average presolar silicate concentrations of ~ 400 μg g^{-1} (Floss *et al.* 2006) and up to the weight per cent level in individual particles (Busemann *et al.* 2009). Primitive meteorites and Antarctic micrometeorites show lower presolar silicate abundances (Nguyen *et al.* 2007, 2010b, Yada *et al.* 2008, Floss and Stadermann 2009, Vollmer *et al.* 2009, Bose *et al.* 2010, Leitner *et al.* 2012). Among the well-characterised meteorites, the highest presolar silicate abundances are seen in CR3 chondrites, the CO3 chondrite ALHA 77307 and the ungrouped C chondrite Acfer 094, where concentrations between 150 and 220 μg g^{-1} have been observed. Early studies of matter returned from the comet Wild 2 yielded only surprisingly low presolar silicate/oxide abundances of 10–20 μg g^{-1} (McKeegan *et al.* 2006, Stadermann *et al.* 2008). However, these abundance estimates are based on the identification of presolar O isotopic signatures in impact residues in large craters on Al foil targets on-board the Stardust spacecraft (Figure 9) in which isotope anomalies might have been partially erased due to melting and mixing of presolar grains with surrounding material of solar system origin. Recently, Leitner *et al.* (2010) started a study of O isotopic compositions of impact residues in small (< 2 μm) craters on Al foils in which dilution effects are expected to be much less pronounced; indeed,

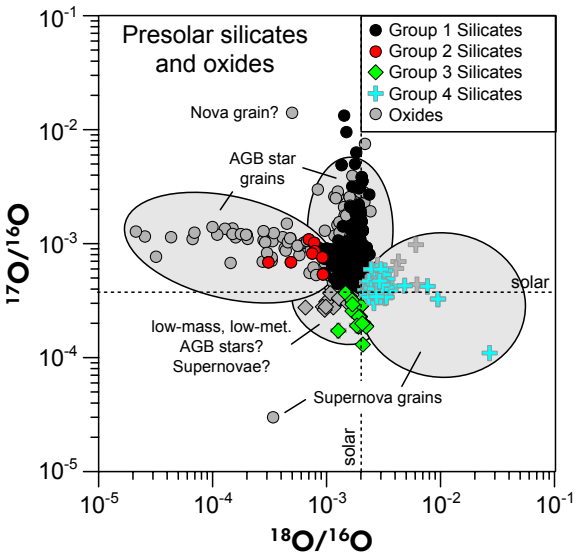

Figure 7. O isotopic ratios of the different groups of presolar silicate grains. Data for presolar oxide grains are shown for comparison. The data are from the Washington University Presolar Grain Database (Hynes and Gyngard 2009). The solar system ratios are shown by the dashed lines.

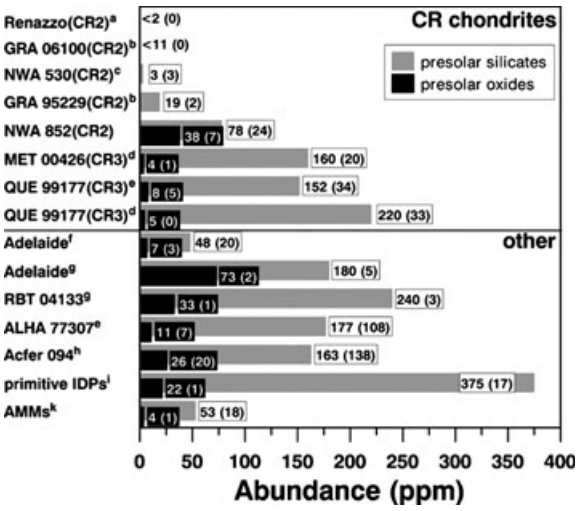

Figure 8. Abundances of presolar silicates and oxides in primitive solar system materials. The numbers in parentheses give the number of identified grains. AMM, Antarctic micrometeorites. Abundances are given in μg g^{-1}. From Leitner *et al.* (2012), © 2012, The American Astronomical Society.

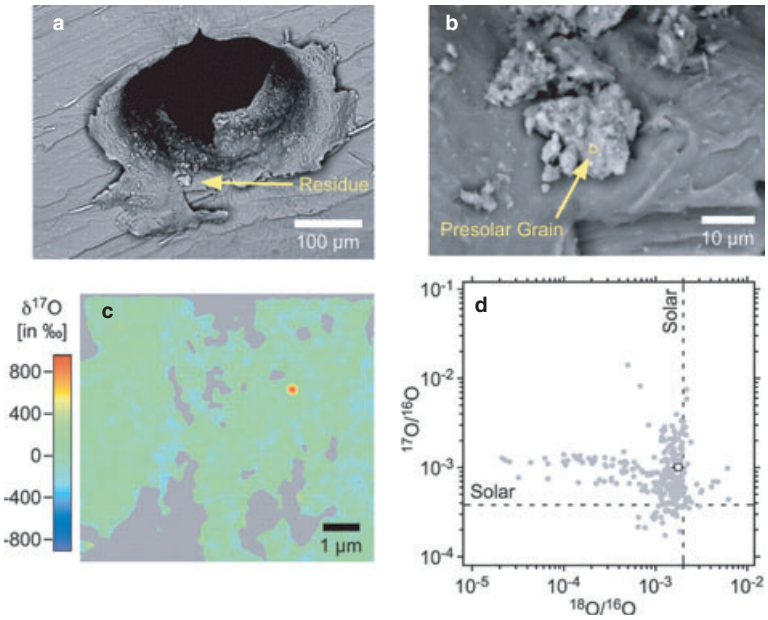

Figure 9. Identification of a presolar O-rich grain (unknown mineralogy) in matter from comet Wild 2 returned by NASA's Stardust mission. (a) SEM picture of a large impact crater on an Al foil. The residue patch in which the presolar grain was found is marked by the yellow arrow. (b) Location of the presolar grain in the residue patch. (c) Isotope map of $\delta^{17}O$ in the residue patch; the presolar grain stands out by its large ^{17}O enrichment. (d) The O isotopic composition of the presolar grain in comparison with the data of other presolar O-rich grains. From McKeegan *et al.* (2006). Reprinted with permission from AAAS.

the finding of a presolar signature in one impact residue among ~ 200 studied impact residues suggests that the abundance of presolar silicates/oxides might be higher than 1000 µg g^{-1}, in agreement with the view that comets represent the most primitive matter in our solar system. A similar conclusion was drawn from another NanoSIMS study of Acfer 094 material used in hypervelocity shot experiments (Floss *et al.* 2013).

Isotope data other than for O are rare for presolar silicates, even for major elements like Mg, Si and Fe, because of experimental difficulties. Silicon can be measured with high spatial resolution with the Cs^+ primary ion source. However, Si ion yields are much lower in O-rich environments than, for example, in SiC. For that reason, measurement uncertainties of Si isotopic ratios of presolar silicates are relatively large (several 10‰). Nevertheless, interesting results have been obtained, for example, that in a Si three-isotope representation silicates plotted along the so-called SiC mainstream line and that Group 4 silicates tend to have lower than solar $^{29}Si/^{28}Si$ and $^{30}Si/^{28}Si$ ratios, in qualitative agreement with the data of SiC SN grains of type *X* (Vollmer *et al.* 2008, Nguyen *et al.* 2010b).

Magnesium is even more challenging than Si because Mg is measured as positive secondary ions by using O^- primary ions. The size of the O^- primary ion beam is comparable with or larger than that of presolar silicates, and large dilution effects are to be expected for the isotope ratios of presolar grains. For this reason, specific procedures have been developed to minimise dilution effects employing a combination of FIB (focused ion beam technique) with NanoSIMS (Nguyen *et al.* 2010a, Kodolanyi and Hoppe 2011). After identification of presolar silicates based on their O isotopic fingerprints, the matter surrounding the presolar silicate grains is removed by FIB milling. This produces deep valleys (1–1.5 µm) in the meteoritic thin sections and results in strongly suppressed Mg secondary ion signals from these regions, thus minimising contributions from the presolar grains' surroundings (Figure 10). While most grains were shown to exhibit only small Mg isotope anomalies, a few SN and nova grains show large anomalies of > 200‰ in $^{25}Mg/^{24}Mg$ and $^{26}Mg/^{24}Mg$ (Nguyen *et al.* 2010a, Nguyen *et al.* 2011).

Like Mg, also Fe isotopes (^{54}Fe, ^{56}Fe, ^{57}Fe) have been measured following FIB milling with the O^- primary ion source and a NS50L (Nguyen *et al.* 2011). Specific care must be taken to account for the ^{54}Cr interference, which cannot be separated from ^{54}Fe. For this reason, ^{52}Cr must be monitored along with the Fe isotopes. The 4 nova and SN grains studied by Nguyen *et al.* (2011) all show solar

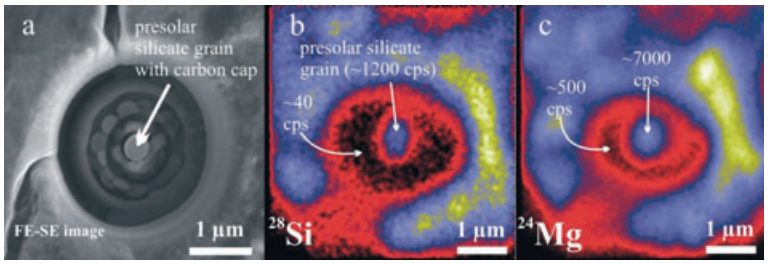

Figure 10. FIB preparation and NanoSIMS Mg isotope measurement of a presolar silicate grain. (a) SEM picture of the presolar silicate and its surrounding; about 1 µm of material around the presolar grain was milled away by FIB. (b) $^{28}Si^{+}$ ion image of the region around the presolar silicate. Secondary ion count rates are strongly suppressed in the valley produced by FIB milling. (c) Same as (b) but for $^{24}Mg^{+}$. From Kodolanyi and Hoppe (2011).

Fe isotopic ratios within uncertainties. Iron isotopes can also be measured as FeO^{-} using the Cs^{+} primary ion source with its higher spatial resolution. Such measurements were done with NS50 ion probes for ^{54}Fe and ^{56}Fe in multi-collection (Mostefaoui and Hoppe 2004, Vollmer and Hoppe 2010) and for ^{54}Fe, ^{56}Fe and ^{57}Fe in a combined multi-collection/peak-jumping mode (Ong *et al.* 2012); typical measurement uncertainties were 30–40‰ for $^{54}Fe/^{56}Fe$ and somewhat larger for $^{57}Fe/^{56}Fe$. While all $^{54}Fe/^{56}Fe$ ratios were shown to be solar within ~ 100‰, moderate $^{57}Fe/^{56}Fe$ anomalies of up to 200‰ were observed.

Presolar oxides: Oxygen ion imaging not only identifies presolar silicates but also presolar oxides. Presolar oxides are less abundant than presolar silicates (Figure 8), but the abundance ratio of presolar oxides to presolar silicates provides important clues on aqueous alteration in meteorite parent bodies (Floss and Stadermann 2009, Leitner *et al.* 2012). In the 1990s, the known presolar oxide inventory contained mostly micrometre-sized grains that were chemically separated from meteorites. In contrast to SiC, separates of refractory O-rich grains contain mostly grains of solar system origin, and small, sub-micrometre-sized presolar grains remained largely undetected. Only with the NanoSIMS did it become possible to identify and study sub-micrometre-sized O-rich presolar grains. A large number of presolar spinel grains were found by O ion imaging of a spinel separate from the Murray meteorite (Zinner *et al.* 2005). The study of those grains has been particularly useful for characterising the Mg isotopic compositions of O-rich stardust, many of which were shown to exhibit substantial Mg isotope anomalies (Figure 11). Zinner *et al.* (2005) also report Cr isotope data for some presolar spinel grains. These

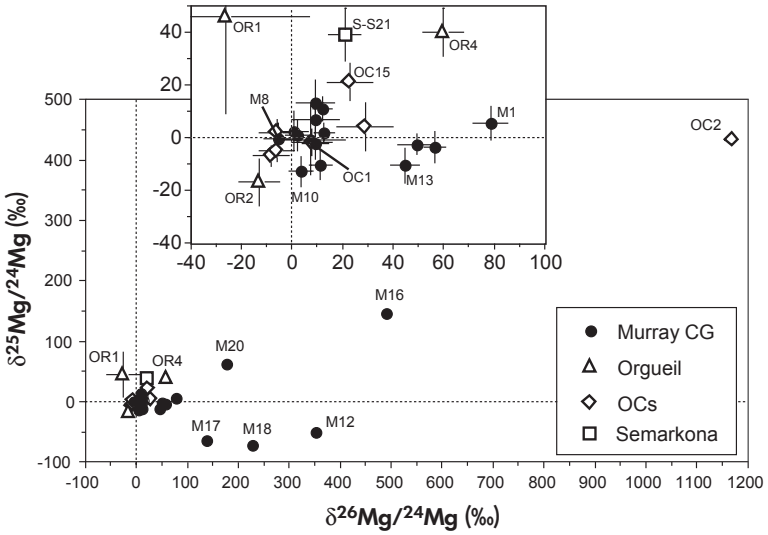

Figure 11. Magnesium isotopic ratios, given as per mil deviation from the solar system ratios, of presolar spinel grains from primitive meteorites. The dashed lines represent the solar ratios. Uncertainty bars are 1*s*. Reprinted from Zinner *et al.* (2005), © 2005, with permission from Elsevier.

measurements were done in a combined multi-collection/peak-jumping mode, involving measurement of all Cr isotopes (^{50}Cr, ^{52}Cr, ^{53}Cr, ^{54}Cr) and selected Ti and Fe isotopes to correct for unresolved isobaric interferences. While these measurements did not reveal large Cr isotope anomalies within the measurement uncertainties of several 10‰, large ^{54}Cr enrichments (with δ^{54}Cr of up to thousands of per mil) have been found by Cr ion imaging on other grain separates, both using O^- primary ions and analysing positive secondary ions of Cr (Dauphas *et al.* 2010, Qin *et al.* 2011) and using Cs^+ primary ions and analysing Cr as CrO^- (Nittler *et al.* 2012). Carriers of these anomalies are $\leq$ 100 nm-sized oxide grains, probably spinel. A spinel grain with large enrichments in ^{16}O (plots in the lower left of Figure 7) was shown to carry radiogenic ^{44}Ca from the decay of radioactive ^{44}Ti (half-life 60 yr); this finally provided proof that grains with large ^{16}O enrichments are from supernovae (SNe), the only place in which ^{44}Ti can be made in large quantities (Gyngard *et al.* 2010). In a combined IMS6f/NS50/NS50L study, Nittler *et al.* (2008) measured O, Mg, Al and K–Ca isotopic compositions of several oxide grains in three separate analysis set-ups. K and Ca isotopes were measured on a NS50 in a combined multi-collection/peak-jumping mode, involving all stable K and Ca isotopes except ^{46}Ca. It was shown that the multi-element isotope data of Group 4 oxide grains agree very well with model predictions for SNe, giving strong support to the proposed SN origin of Group 4 grains.

Presolar SiC and graphite: Presolar SiC and graphite grains were studied by conventional SIMS in great detail for isotopic composition during the late 1980s and the 1990s. These measurements concentrated on micrometre-sized grains. With the advent of the NanoSIMS ion probe, it became possible to extend such studies to sub-micrometre-sized grains, to look for isotope heterogeneities in larger grains and to extend the isotope studies to yet unexplored elements. Because SiC can be separated from meteorites in almost pure form by physical and chemical treatments and because it hosts a large number of minor elements, a large body of information on isotopic compositions exists, and SiC can be considered the best characterised presolar mineral. As with the O-rich presolar grains, presolar SiC was divided into distinct populations, based on the isotopic compositions of C, N and Si (Zinner 2007, Hoppe 2008, Figures 12 and 13).

An important NanoSIMS application is the search for rare X, U/C and Z grains, which can be identified on the basis of specific Si isotope signatures (Figure 13), among SiC grain separates for detailed follow-up studies. Many of these searches were done by C and Si ion imaging in a fully automated way (Gröner and Hoppe 2006, Gyngard *et al.*

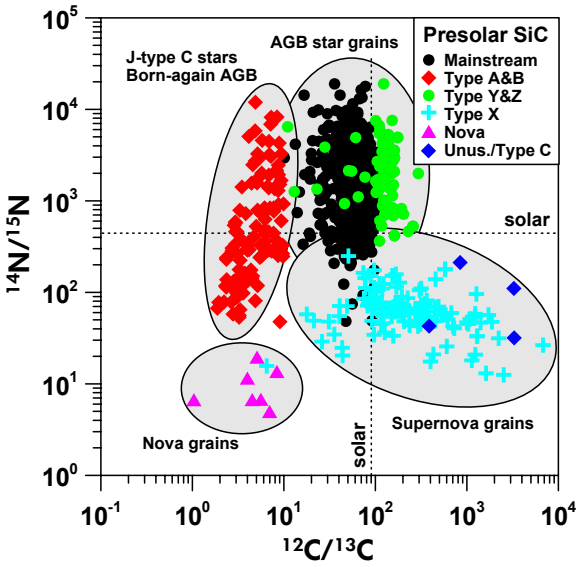

Figure 12. Carbon and N isotopic compositions of different populations of presolar SiC grains. The solar ratios are indicated by the dashed lines. From Hoppe (2011).

2010). This permitted the study of thousands of small presolar SiC grains. It was shown that the abundance of Z grains increases with decreasing grain size (Zinner *et al.* 2007, Hoppe *et al.* 2010), consistent with the view that these grains formed in the winds of low-mass AGB stars with comparatively low metallicity. Further constraints on the parent stars of *Z* grains came from Mg–Al and Ti isotope measurements. The Ti measurements were done in a combined multi-collection peak-jumping mode with a NS50, involving all five Ti isotopes and selected Ca, V and Cr isotopes to correct for unresolved isobaric interferences (Zinner *et al.* 2007).

Fully automated ion imaging surveys also identified several of the rare *X* and U/C grains (Hoppe *et al.* 2010, 2012). The finding of high abundances of ^{26}Al and the presence of radiogenic ^{44}Ca in U/C grains demonstrated their close relationship to *X* grains and finally proved the SN origin of U/C grains (Hoppe *et al.* 2012). Sulfur isotope measurements on U/C and *X* grains revealed large S isotope anomalies, namely enhancements in ^{32}S. The combination of heavy Si (Figure 13) with light S (Figure 14) in U/C grains has been interpreted to result from a fractionation between S and Si caused by molecule chemistry in the still unmixed SN ejecta (Hoppe *et al.* 2012). Several *X* grains have also been analysed for Li and B isotopic compositions (Fujiya *et al.* 2011). The observed small excess of ~ 16% for ^{11}B has been interpreted to be a hint for B produced by the neutrino process in SNe.

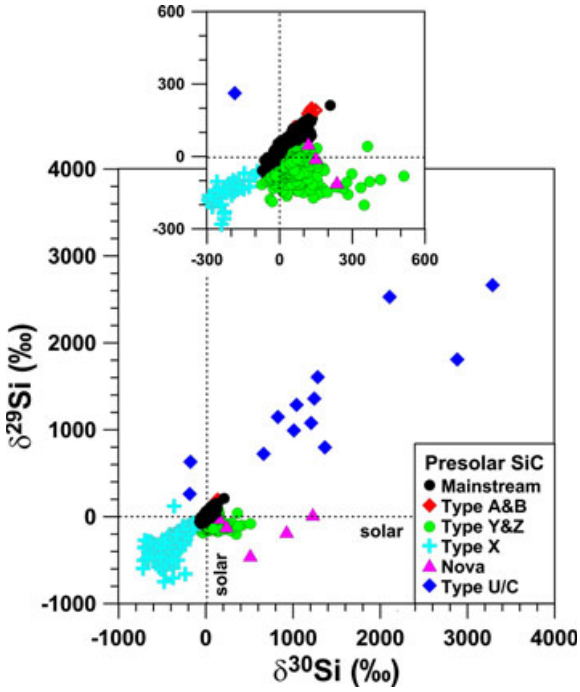

Figure 13. Silicon isotopic ratios in per mil deviation from the solar system ratios for different populations of presolar SiC grains. The mainstream grains show only moderate Si isotope anomalies and plot along a line with slope 1.37 ('SiC mainstream line'). The *X* grains are characterised by large enrichments in ^{28}Si, and the U/C grains by large enrichments in ^{29}Si and ^{30}Si. Most *Z* grains have lower than solar ^{29}Si/^{28}Si and plot to the right of the mainstream line.

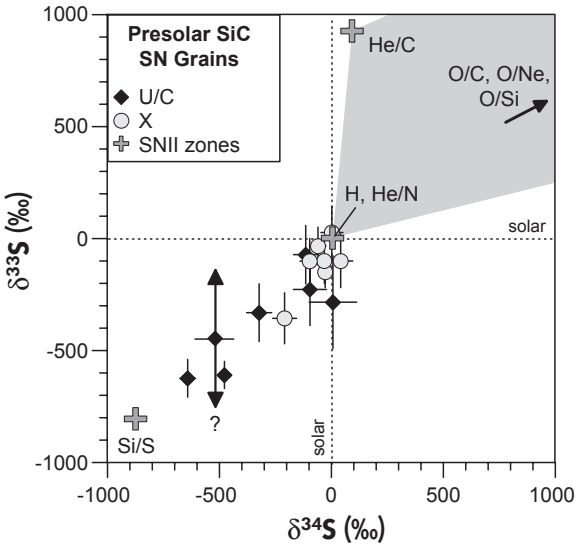

Figure 14. Sulfur isotopic ratios, given as per mil deviation from the solar system ratios, of presolar SiC grains of type *X* and U/C, which are from SNe. The question mark indicates an unknown δ^{33}S in the respective grain. Predictions for different layers in a 15 M⊙ SNII (Rauscher *et al.* 2002) are shown for comparison. Uncertainty bars are 1*s*. Adapted from Hoppe *et al.* (2012).

A large number of *X* grains and a few nova and presolar Si_3N_4 grains, mostly micrometre in size, which were previously found by ion imaging in the older-generation Cameca IMSxf instruments, have also been studied in the NanoSIMS for several isotope systems of intermediate-mass elements. Besmehn and Hoppe (2003) report Si and Ca–Ti (^{40}Ca, ^{42}Ca, ^{44}Ca, ^{48}Ti) isotope data, showing that the spatial distribution of radiogenic ^{44}Ca is positively correlated with ^{48}Ti, giving strong support to the view that ^{44}Ca excesses are from the decay of radioactive ^{44}Ti. Nittler and Hoppe (2005) report Mg–Al, Ca–Ti (same isotopes as above) and Ti (all Ti isotopes together with ^{52}Cr to correct for unresolved ^{50}Cr measured in a combined multi-collection/peak-jumping mode) data for several grains originally classified as *X* and nova grains. These measurements showed that a grain with very low ^{12}C/^{13}C and ^{14}N/^{15}N ratios, which is commonly attributed to a nova source, carried radiogenic ^{44}Ca, pointing to an origin from a SN. Lin *et al.* (2010) measured Mg–Al and Ca–Ti–V (^{40}Ca, ^{44}Ca, ^{46}Ti, ^{47}Ti, ^{48}Ti, ^{49}Ti, ^{51}V in a combined multi-collection/peak-jumping mode using a NS50) and investigated different SN mixing scenarios to account for the multi-element isotope data. Marhas *et al.* (2008) report C, N and Si isotopic data (all C, N [CN] and Si isotopes measured in a combined multi-collection/peak-jumping mode) as well as Fe and Ni isotope data (^{52}Cr, ^{54}Fe, ^{56} Fe, ^{57}Fe, ^{58}Ni, ^{60}Ni, ^{61}Ni, and ^{62}Ni measured in a combined multi-collection/peak-jumping mode using a NS50; ^{52}Cr was included to correct ^{54}Fe for unresolved ^{54}Cr; ^{56}Fe was used to correct ^{58}Ni for unresolved ^{58}Fe). As was similarly concluded for S in U/C grains, the Fe isotope data of *X* grains (Figure 15), namely their close-to-solar ^{54}Fe/^{56}Fe ratios, suggest elemental fractionation between Fe and Si in SN ejecta, possibly by molecule chemistry.

In addition to isotope measurements on rare SiC grain types as described above, interesting results have also been obtained for micrometre-sized mainstream (and *X*) grains. Barium isotope data (all Ba isotopes except the very rare ^{130}Ba and ^{132}Ba were measured in a combined multi-collection/peak-jumping mode) were reported by Marhas *et al.* (2007) for several mainstream and *X* grains. While the *X* grains exhibit Ba isotope patterns that are not conclusive with respect to SN nucleosynthesis and mixing, the mainstream grains exhibit an s-process pattern, which is well explained within the context of an origin from low-mass AGB

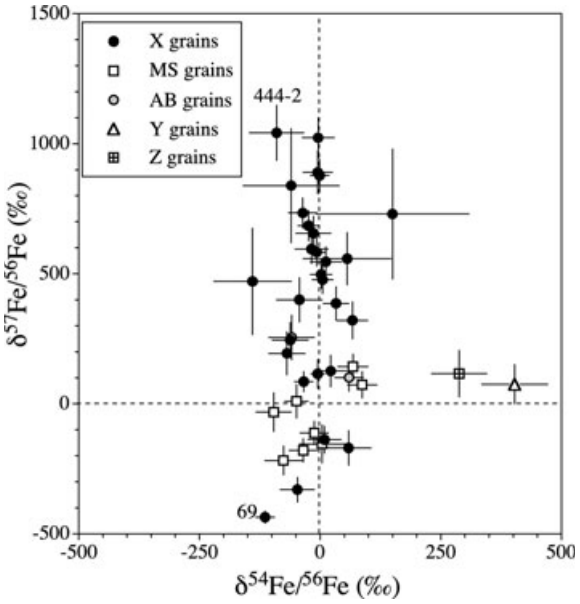

Figure 15. Iron isotopic compositions, given as per mil deviation from the solar ratios, for different populations of presolar SiC grains. The close-to-normal $^{54}Fe/^{56}Fe$ ratios of *X* grains are surprising in view of simple *ad hoc* SN mixing models. Uncertainty bars are 1*s*. From Marhas *et al.* (2008), Figure 4. Reproduced by permission of the AAS.

stars. Gyngard *et al.* (2009) measured Li isotopes and found enrichments in ^{6}Li of up to 30%, which are best explained by spallation reactions induced by Galactic cosmic rays. From the ^{6}Li enrichments, cosmic ray exposure ages of between 40 Myr and 1 Gyr have been inferred.

Stadermann *et al.* (2005b) studied in detail the C, N, O and Ti isotopic compositions in TEM microtome slices of a 12 μm-sized presolar graphite grain. These measurements were done in three set-ups, comprising the C and CN isotopes measured with multi-collection, the C and O isotopes measured with multi-collection and the Ca and Ti isotopes measured in a combined multi-collection/peak-jumping mode (^{40}Ca, ^{43}Ca, ^{44}Ca and all Ti isotopes). Isotope gradients were found for $^{13}C/^{12}C$ and $^{18}O/^{16}O$, probably the result of isotope exchange with material of normal composition. Internal TiC subgrains showed a strong O signal with larger O isotope anomalies than was found in the host graphite. The TiC subgrains exhibit large ^{49}Ti enrichments and in one case evidence for now extinct ^{44}Ti, as similarly observed in SiC SN grains. Extended multi-element (C, N, O, Si, Al–Mg, K–Ca, Ti) NanoSIMS studies were conducted by Jadhav *et al.* (2008) on several micrometre-sized high-density presolar graphite grains. These measurements were done in 5 set-ups, comprising C and O isotopes, CN and Si isotopes, Mg–Al isotopes (all with multi-collection), as well as K–Ca isotopes (^{39}K, ^{41}K, ^{40}Ca, ^{42}Ca, ^{44}Ca, ^{48}Ti plus ^{12}C for grain identification) and Ti (all Ti isotopes plus ^{40}Ca, ^{51}V and ^{52}Cr for interference corrections and ^{12}C for grain identification) measured in a combined multi-collection/peak-jumping mode. Extremely large non-radiogenic Ca and Ti isotope anomalies were found, especially enrichments in ^{42}Ca (up to a factor of 17), ^{43}Ca (up to a factor of 29), ^{46}Ti (up to a factor of 36) and ^{50}Ti (up to a factor of 34).

Extraterrestrial organics

Another important area of NanoSIMS applications is isotope measurements by ion imaging of the low atomic number elements H, C, N and O in organic matter from a variety of primitive solar system materials. Isotopic fingerprints of these elements can be used to constrain the physico-chemical conditions under which the organics formed. Examples of possible mechanisms to produce large D and ^{15}N enrichments include ion–molecule reactions in the gas phase at low temperatures (10–20 K) and catalytic processes on dust grains. These specific fingerprints can be inherited by organic matter that formed in cold interstellar molecular clouds or in the outer reaches of the protoplanetary disc where low-temperature conditions prevailed.

Duprat *et al.* (2010) report on large D excesses (D/H values of 10–30× the terrestrial value) in organic matter in micrometeorites from Antarctic snow. Because crystalline minerals are embedded in the organics, the authors favour a solar system origin, namely in the cold regions of the protoplanetary disc, rather than an interstellar heritage. Large D excesses with D/H ratios of 2.5–9× the terrestrial value have also been found in micrometre- and sub-micrometre-sized organic globules from the Tagish Lake meteorite (Nakamura-Messenger *et al.* 2006). These globules are thought to have formed as organic ice coatings on pre-existing grains that were photochemically processed into refractory organic matter, either in the protoplanetary disc or in the cold molecular cloud from which our solar system formed. The globules also exhibit large ^{15}N enrichments with $^{15}N/^{14}N$ ratios of 1.2–2× the terrestrial atmospheric composition. Figure 16 shows the N isotopic ratios together with the corresponding TEM image, illustrating the information that can be obtained from co-ordinated NanoSIMS and TEM studies of 50–70 nm-thick microtome sections. Large D and ^{15}N excesses at the micrometre scale are a characteristic feature of IDPs, as was inferred already by ion imaging with conventional SIMS (Messenger 2000). In a combined NanoSIMS (C and N isotopes) and conventional SIMS (H isotopes) study of insoluble organic matter (IOM)

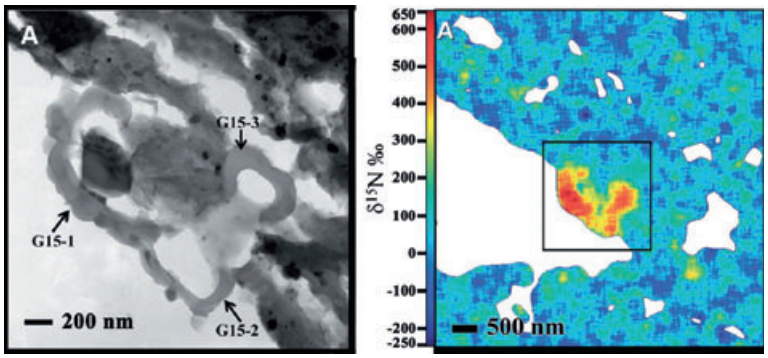

Figure 16. Left: Bright-field TEM image of three organic globules (G15-1 1.3 μm, G15-2 0.7 μm and G15-3 0.55 μm) embedded in saponite matrix. Right: Nitrogen isotopic image of a section containing a uniform ^{15}N-enriched globule aggregate. The box is the field of view of the left Figure. From Nakamura-Messenger *et al.* (2006). Reprinted with permission from AAAS.

from primitive meteorites, Busemann *et al.* (2006) showed that micrometre-sized H and N isotope anomalies ('hot spots'; D/H up to 20× and ^{15}N/^{14}N up to 4× the terrestrial values) reach or even exceed those seen in IDPs. This implies that both samples from asteroids (meteorites) and samples presumably from comets (certain IDPs) preserve primitive organics from the time when our solar system formed. Samples returned from comet Wild 2 by NASA's Stardust mission confirm this conclusion (McKeegan *et al.* 2006). The largest ^{15}N enrichments of up to 6× the terrestrial abundance have been found in a xenolith from the unique CB–CH chondrite Isheyevo (Briani *et al.* 2009; Figure 17). Interestingly, this xenolith does not only host matter enriched in ^{15}N but also matter with depletions in ^{15}N of ~ 30%. These ^{15}N depletions come close to those inferred for Jupiter and the Sun (Owen *et al.* 2001, Meibom *et al.* 2007b, Marty *et al.* 2011, Huss *et al.* 2012), testifying the pristine nature of this unique object. Generally, C isotopic anomalies have turned out to be small in organic matter, typically only at the lower per cent level. A comparatively large C isotope anomaly has been reported by Floss *et al.* (2004) for the anhydrous IDP Benavente in which a ~ 1 μm^2-sized patch of C-rich matter, probably heteroatomic organic compounds, with a depletion in ^{13}C of 70‰, which is associated with a ^{15}N enrichment, was found (Figure 18). Additional micrometre-sized grains with similar isotopic anomalies were

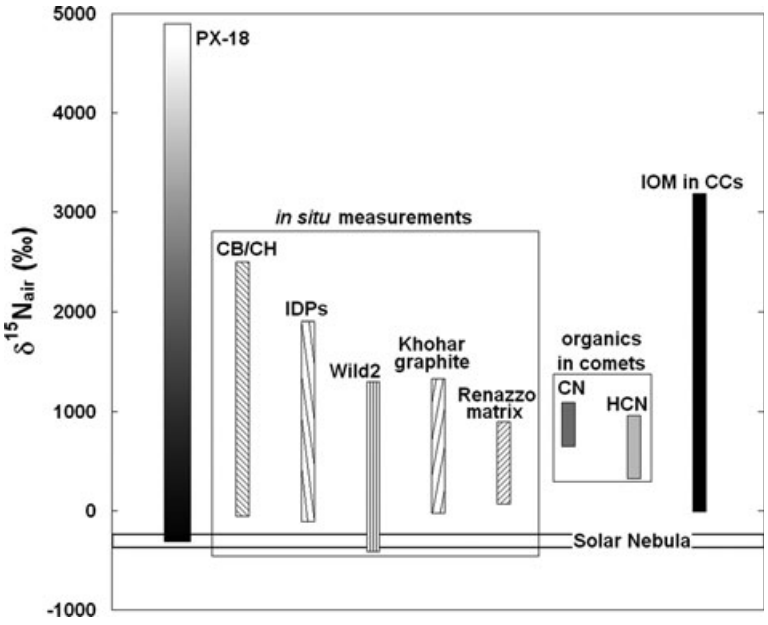

Figure 17. Range of δ^{15}N values found in xenolith PX-18 from the CB–CH chondrite Isheyevo in comparison with other primitive solar system materials. From Briani *et al.* (2009).

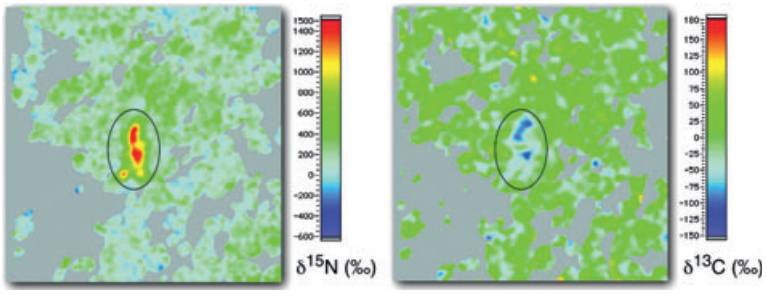

Figure 18. Maps of $\delta^{15}N$ and $\delta^{13}C$ in the IDP Benavente. A region with enhanced ^{15}N and depleted ^{13}C has been circled. Field of view is 10 μm × 10 μm². From Floss *et al.* (2004). Reprinted with permission from AAAS.

found by De Gregorio *et al.* (2010) and Matrajt *et al.* (2012).

Hashizume *et al.* (2011) discovered extreme O isotope anomalies with $\delta^{17,18}O$ values of up to 530 ± 110‰ in IOM from a carbonaceous chondrite (Figure 19). The authors propose an origin of these $^{17,18}O$ enrichments by photodissociation of carbon monoxide in the protosolar nebula.

Extinct radioactive nuclides

Several isotope systems (Mg–Al, S–Cl, Cr–Mn, Fe–Ni) have been studied with the NanoSIMS in meteoritic and cometary minerals in the quest for now extinct radioactive nuclides and to obtain time constraints on the early chronology of solar system formation. Matzel *et al.* (2010) measured the ^{26}Mg–^{26}Al isotope systematics of a ~ 5 μm-sized refractory particle ('Coki') from comet Wild 2 returned by NASA's Stardust mission. No evidence for radiogenic ^{26}Mg from the decay of radioactive ^{26}Al (half-life 716 kyr) was found, which let the authors to conclude that this refractory particle formed at least 1.7 Myr after calcium–aluminium-rich inclusions (CAIs) in the inner solar system, was transported to the Kuiper belt and finally incorporated into Wild 2.

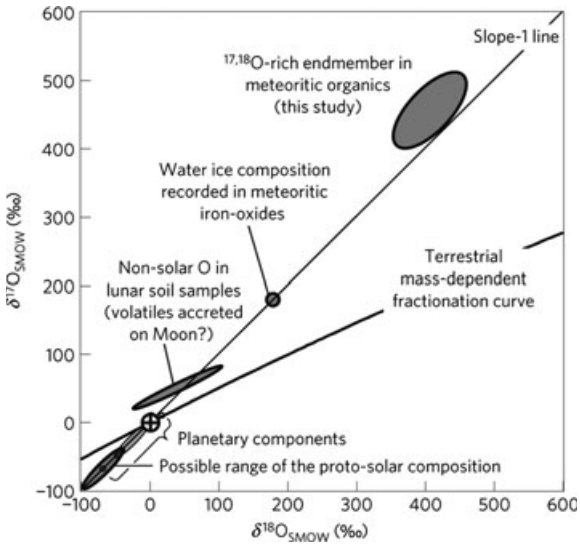

Figure 19. Oxygen isotopic composition of an $^{17,18}O$-rich end member in meteoritic organics compared with other planetary materials. Reprinted by permission from Macmillan Publishers Ltd: Nature Geoscience (Hashizume *et al.* 2011), © 2011.

Jacobsen *et al.* (2011) and Nagashima *et al.* (2008) investigated the ^{36}S–^{36}Cl isotope systematics in 5–40 μm-sized Cl-bearing minerals in CAIs and in a chondrule. As pointed out in the section Isotope measurements, the background in the mass 36 region must be monitored, which requires measurements in a combined multi-collection/peak-jumping mode. Nagashima *et al.* (2008) found no clear evidence for radiogenic ^{36}S from the decay of radioactive ^{36}Cl (half-life 0.30 Myr) in sodalite in CAIs from the Vigarano CV3 chondrite and in a chondrule from the Ningqiang carbonaceous chondrite. For sodalite in the Pink Angel CAI from the Allende CV3 chondrite, Nagashima *et al.* (2008) reported small ^{36}S excesses (at the 2*s* level) from which an initial $^{36}Cl/^{35}Cl$ of ~ 2×10^{-6} was inferred. Much higher ^{36}S excesses have been observed by Jacobsen *et al.* (2011) in wadalite from CAIs in Allende leading to an inferred initial $^{36}Cl/^{35}Cl$ of $(1.81 \pm 0.13) \times 10^{-5}$. It was concluded by these authors that the high level of ^{36}Cl and the absence of ^{26}Al in co-existing grossular implies production of ^{36}Cl by late-stage solar energetic particles in the protoplanetary disc and that ^{36}Cl is unrelated to the origin of ^{26}Al.

^{53}Cr–^{53}Mn isotope systematics have been studied on carbonates from CI (Hoppe *et al.* 2007, Petitat *et al.* 2011) and CM chondrites (Fujiya *et al.* 2012). These measurements were done in a combined multi-collection/peak-jumping mode in order to record ^{52}Cr and ^{53}Cr ion intensities on NS50 instruments. Large ^{53}Cr excesses were

found that correlate with Mn/Cr ratios (Figure 20), providing clear evidence for the decay of radioactive ^{53}Mn (half-life 3.7 Myr). Hoppe *et al.* (2007) and Petitat *et al.* (2011) infer ^{53}Mn/^{55}Mn ratios of 2–5 × 10^{-6} in carbonates from the CI chondrites Orgueil and Kaidun, suggestive of carbonate formation and onset of aqueous activity on the parent body ~ 3–4 Myr after CAI formation. Similarly, Fujiya *et al.* (2012) inferred ^{53}Mn/^{55}Mn ratios of ~ 3 × 10^{-6} for four CM chondrites, suggesting a formation age of ~ 5 My after CAI formation.

Mostefaoui *et al.* (2005) studied the ^{60}Ni–^{60}Fe isotope system in troilite grains from metal-free aggregates and in magnetite grains from the Semarkona ordinary chondrite. In this study, ^{54}Fe, ^{60}Ni and ^{62}Ni were measured in multi-collection. A potential problem is the tail contribution of ^{46}TiO to ^{62}Ni in samples with high Ti and low Ni; consequently, Ti-rich samples must be avoided. The observed ^{60}Ni excesses of up to ~ 100‰ correlate with Fe/Ni ratios, suggestive of decay of radioactive ^{60}Fe (half-life 2.6 Myr). The inferred initial ^{60}Fe/^{56}Fe in troilite is (0.92 ± 0.24) × 10^{-6} (2*s*); however, isotope disturbance cannot be fully excluded, and the initial abundance of ^{60}Fe in the solar system is still a matter of lively debate and further research.

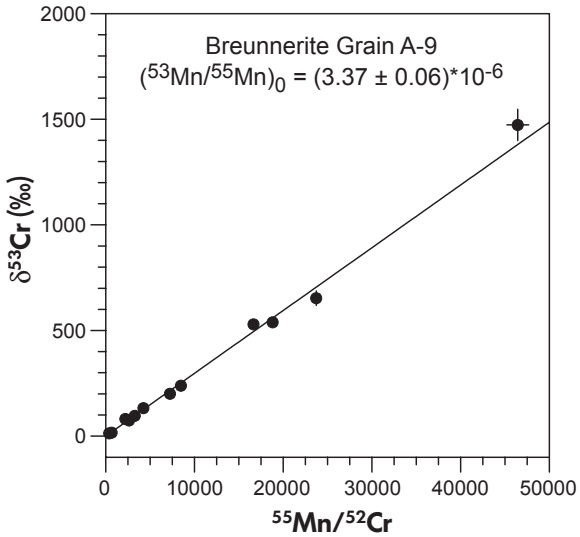

Figure 20. δ^{53}Cr as a function of Mn/Cr ratios in a 180 μm × 180 μm^2-sized carbonate (breunnerite) grain from the Orgueil CI chondrite. The good correlation between ^{53}Cr excesses and Mn/Cr suggests decay of radioactive ^{53}Mn (half-life 3.7 Myr) with an initial ^{53}Mn/^{55}Mn ratio of (3.37 ± 0.06) × 10^{-6} at the time when this carbonate formed. Uncertainty bars are 1*s*. From Hoppe *et al.* (2007).

Other meteoritic and Lunar samples

Meibom *et al.* (2007b) studied the C and N isotopic compositions of C-bearing osbornite (TiN) in a CAI from the Isheyevo meteorite. The petrography and mineralogy of this CAI as well as thermodynamic calculations suggest that the osbornite formed in a high-temperature region of the solar nebula and that the C and N represent protosolar compositions. The measured ^{15}N/^{14}N ratio of (2.356 ± 0.018) × 10^{-3} (1*s*) is distinctly lower than air composition (0.0036765) or bulk meteorites, but is in excellent agreement with the values reported for Jupiter ((2.3 ± 0.3) × 10^{-3}; Owen *et al.* 2001; Figure 21) and for solar wind samples returned by NASA's Genesis mission ((2.27 ± 0.03) × 10^{-3} (2*s*), Marty *et al.* 2011; (2.12 ± 0.34) × 10^{-3} (2*s*), Huss *et al.* 2012). The ^{13}C/^{12}C ratio of 0.01125 in osbornite was found to be close to that of terrestrial samples and bulk meteorites.

Oxygen isotope imaging has been used to study CAIs and Wark-Lovering rims. In contrast to presolar grains, where O isotope anomalies are very large (see Presolar grains), smaller anomalies (at the several per mil or 10*s* of per mil level) must be resolved among adjacent minerals in these objects. This has been successfully achieved by Ito and Messenger (2008) who observed a sharp O isotopic boundary between neighbouring minerals in a CAI that constrains its thermal history. Ito *et al.* (2010) and Simon *et al.* (2011) found O isotopic variations in Wark-Lovering

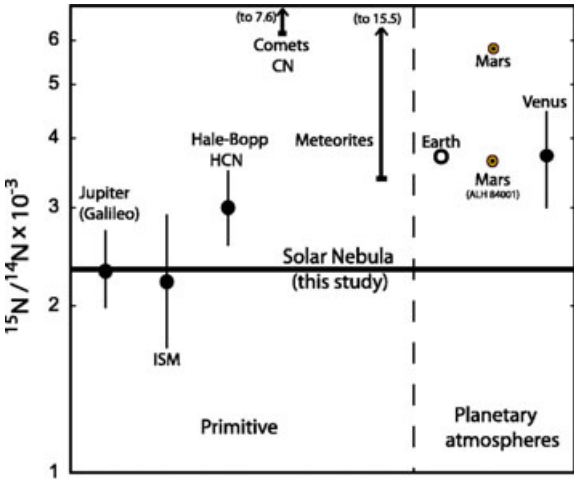

Figure 21. N isotopic ratios of different solar system objects and the ISM. The data for osbornite from a CAI are indicated by the solid line. From Meibom *et al.* (2007b), © 2007, The American Astronomical Society.

rims, which suggest circulation of their host CAIs in the solar nebula.

While most NanoSIMS studies in cosmochemistry have dealt with isotope measurements, some others dealt with the investigation of trace element concentrations and distributions on a micrometre-size scale in extraterrestrial rocks. Beck *et al.* (2005) studied shock processes in two meteorites, the ordinary chondrite Tenham and the Martian meteorite Zagami. Concentrations of Ca, Mn, Rb, Cs and Ba (recorded as positive secondary ions of ^{44}Ca, ^{55}Mn, ^{85}Rb, ^{133}Cs and ^{138}Ba along with other isotopes of major and minor elements in two series in multi-collection) were imaged in co-existing high-pressure minerals. From this, it was inferred that these meteorites experienced a shock with a duration of ~ 1 s caused by an impactor ~ 5 km in size (Tenham) and of ~ 10 ms caused by an impactor ~ 0.1 km in size (Zagami). Saal *et al.* (2008) measured abundances of CO_2, H_2O, F, S and Cl in lunar volcanic glasses (recorded as negative secondary ions of ^{12}C, ^{16}OH, ^{19}F, ^{32}S and ^{35}Cl along with ^{30}Si in multi-collection using a NS50L). From this, it was inferred that the bulk Moon is not completely depleted in highly volatile elements, including water. The latter was estimated, based on the NanoSIMS data and model calculations, to be present at a level of 745 μg g^{-1}. In a follow-up study by Hauri *et al.* (2011) of the same trace elements or compounds (except CO_2) by ion imaging of lunar melt inclusions, water contents of between 615 and 1410 μg g^{-1} were inferred. Abundances of F, S and Cl are in the range observed for terrestrial mid-ocean ridge basalts and are highly correlated with water contents. This led these authors to conclude that some parts of the lunar interior contain as much water as the Earth's upper mantle. A method to measure rare earth element abundances with 5–10 μm spatial resolution has been developed for a NS50L and applied to CAI minerals by Ito and Messenger (2009). This method makes use of the multi-collection capability of the NanoSIMS and employs energy filtering, following the previously established technique for conventional SIMS (Zinner and Crozaz 1986).

Applications in biological geochemistry

The high spatial resolution of the NanoSIMS has opened up new studies in more biologically oriented research fields as well. With a spatial resolution better than *ca.* 300 nm, one can begin to resolve not only individual cells, but also different compartments within cells. This capability, in combination with dynamic (i.e., pulse-chase) isotopic labelling experiments in which a compound is strongly enriched in a rare stable isotope or in a trace element, allows the uptake, assimilation, storage and translocation of this compound (and its metabolic derivatives) to be imaged directly. Any compound that can be isotopically or trace element labelled can in principle be imaged, provided that the target molecules are not lost during sample preparation. Importantly, by labelling a compound isotopically, biological function is not compromised. This is especially important when working with small molecules that are not easily tagged with, for example, fluorescent probes without affecting their biological function. Furthermore, in isotopic labelling experiments, high analytical precision or accuracy is not a strong requirement because the isotopic effects introduced into the cell with the labelled compound(s) are usually very large. Nonetheless, it is recommended that control samples consisting of similarly prepared, but isotopically normal biological tissue be used as a reference material against which the isotopic anomaly is quantified. This will remove any concern about IMF, matrix effects, etc.

Sample preparation of biological tissue for NanoSIMS analysis is an important process, but the details are outside the scope of this review. Here it is simply pointed out that the NanoSIMS is capable of analysing thin sections prepared for imaging by TEM (see also Extraterrestrial organics). Such sections of biological samples are usually about 70–150 nm thick and are produced by ultramicrotomy of cells embedded in epoxy or paraffin. The loss of soluble compounds during the process of fixation and embedding of cells is a problem that requires serious attention.

In the following, four examples of the use of the NanoSIMS on biological samples are provided, which are intended to illustrate the type of data that can be obtained on biological materials. As a result of data treatment by different laboratories using different software, the colour coding of the images presented below is different, but the isotopic or trace element enrichments should be clearly observable in each case. In addition, the table in Appendix A gives a comprehensive (but perhaps not exhaustive) summary of NanoSIMS studies on biological materials, which will allow the reader to rapidly find more detailed information about the study of a particular type of biological tissue. Most of these measurements were done in a static multi-collection mode, and unresolved isobaric interferences are of no concern. For this reason, we do not give as much of the measurement details as for the applications described above (Applications in cosmochemistry).

Environmental microbiology

Bacteria and archaea play an essential role in the global biogeochemical cycle and in many more localised biological processes. However, means to evaluate directly

metabolic processes by these unicellular organisms at the scale of individual cells, or in cell populations within larger and more complex communities, have been lacking. With the NanoSIMS, in combination with, for example, *in situ* hybridisation techniques that allow specific bacterial or archaea strains to be individually identified, or in combination with gene expression studies, it is now possible to shed light on the N and/or C fixation processes by individual populations of bacteria *in situ* (Lechene *et al.* 2007, Popa *et al.* 2007, Musat *et al.* 2008).

Figure 22 is from a study of filamentous N-fixing cyanobacteria (Popa *et al.* 2007). Some cyanobacteria are uniquely capable of fixing both dinitrogen (N_2) and carbon dioxide (CO_2), deriving energy from oxygenic photosynthesis. The sheer abundance in phytoplankton communities makes these microorganisms important species in the global biogeochemical cycles of C and N. Under conditions of N limitation, some vegetative cells of filamentous freshwater cyanobacterium (here *Anabaena oscillarioides*) can differentiate into heterocysts, non-growing, specialised cells in which N_2 is fixed into organic N (Stewart 1973, Meeks and Elhai 2002). This process is catalysed by the enzyme nitrogenase, but the activity of nitrogenase is inhibited by the presence of oxygen (Stewart 1973). Therefore, the heterocysts must be physically isolated from

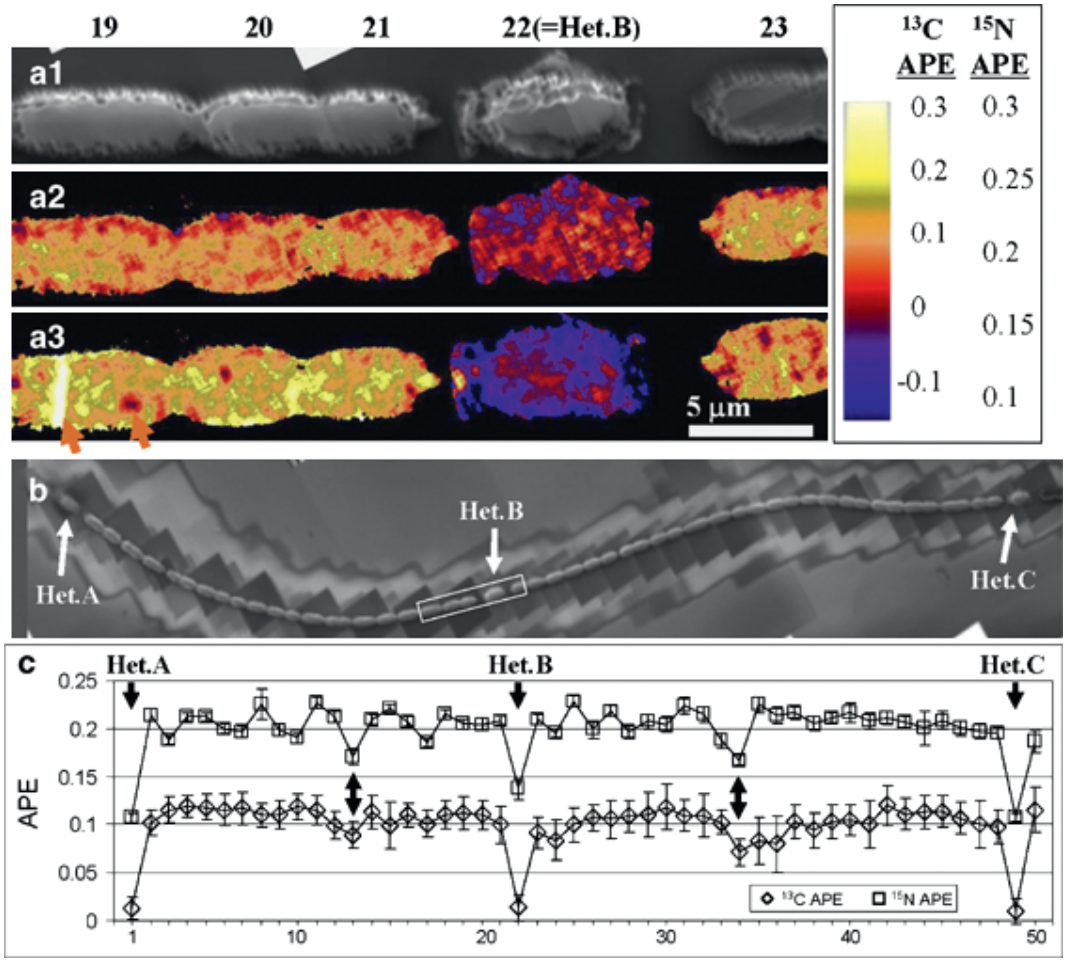

Figure 22. Chain of five cells from a filament of *Anabaena oscillarioides* analysed with NanoSIMS after 4 hr of incubation with $H^{13}CO_3$ and $^{15}N_2$. Het: heterocyst. Individual cells are numbered to correspond with the numbering in (c). (a1) Image reconstruction based on secondary electrons. (a2) The distribution of ^{13}C enrichment. (a3) The distribution of ^{15}N enrichment. Enrichment is expressed as atom per cent enrichment (APE). (b) Post-analysis NanoSIMS secondary electron image of a filament of fifty cells of *A. oscillarioides* showing three heterocysts (Het) after 4 hr of incubation with $H^{13}CO_3$ and $^{15}N_2$. The white box indicates the area shown in the images a1, a2 and a3. (c) The cell-to-cell variation in ^{13}C (diamonds) and ^{15}N enrichment (squares) along the same filament of fifty cells. There are 1–6 independent replicate measurements per cell. Uncertainty bars are 2*s*. Reprinted by permission from MacMillan Publishers Ltd: The ISME Journal (Popa *et al.* 2007), © 2007.

nearby vegetative cells, which are sites of oxygenic photosynthesis and CO_2 fixation. At the same time, this isolation cannot be complete, because the vegetative and heterocyst cells must be able to exchange energy, organic C and fixed N. How these two cell types, heterocysts and vegetative cells, respectively, coexist in the same filament and manage to share resources and maintain equilibrium between oxygenic photosynthesis and N_2 fixation have been studied with NanoSIMS imaging following dynamic $NaH^{13}CO_3$ and $^{15}N_2$ enrichment experiments of their medium (Popa *et al.* 2007).

Figure 22 demonstrates the intracellular isotopic heterogeneity between heterocysts and vegetative cells after 4 hr of incubation with $NaH^{13}CO_3$ and $^{15}N_2$. The observed patterns of isotopic enrichment reflect both cell physiology and development. The study found evidence for rapid export of newly fixed N_2 from heterocysts to vegetative cells and relatively uniform distribution of newly fixed N_2 among vegetative cells, with the exception of cells in the process of heterocyst differentiation (mid-point cells indicated by double arrows in Figure 22c). Features of cell division in vegetative cells (Figure 22a3, cell #19) and relative differences between the biosynthetic age of amino acid C and N used to construct septation walls can also be observed with the high spatial resolution offered by the NanoSIMS. The isotopic maps presented in Figure 22 show that the metabolic role and level of activity of individual cells can be inferred directly from NanoSIMS imaging, which can quantify the uptake of, for example, ^{13}C and ^{15}N during the labelling experiment(s). This approach can be used to study single-cell-level physiological performance in a wide range of prokaryote communities, as well as exchange of metabolites between adjacent cells.

In another NanoSIMS study of N_2 fixation by individual bacteria living in symbiosis with a eukaryotic host, it was demonstrated that N_2 fixed by the bacteria is transferred to the host eukaryote cells and used for metabolism (Lechene *et al.* 2007). The bivalve *Lyrodus pedicellatus* (commonly known as shipworm) has a gill containing a gland (gland of Deshayes) that hosts a population of symbiont bacteria of the species *Teredinibacter turnerae*, which were suspected to be able to fix N_2. In extracted and cultured populations of *T. turnerae*, it was found that the mean ^{15}N fraction increased over time during incubation with $^{15}N_2$ (Figure 23a–c). As a control, it was observed that the $^{15}N/^{14}N$ ratio in cells of *Enterococcus faecalis*, a bacterium lacking the ability to fix nitrogen, did not increase when grown for the same estimated number of generations in the presence of the $^{15}N_2$ tracer and analysed together with *T. turnerae* in a mixed population (Figure 23a–c).

NanoSIMS imaging was then applied to measure the incorporation of ^{15}N by symbionts within gill bacteriocytes *in vivo* by exposing *L. pedicellatus* to $^{15}N_2$ for 8 days. Figure 23d exhibits the dramatic increase in the $^{15}N/^{14}N$ ratio within the gland of Deshayes, associated with the bacterial community, demonstrating the strong incorporation of gaseous $^{15}N_2$ into bacterial biomass. Furthermore, host structures free of bacteria within the gill show enhanced $^{15}N/^{14}N$ ratios (albeit less than the bacteria themselves), providing strong evidence that $^{15}N_2$ fixed by the bacteria in the gland is transferred to the host organism and used in biosynthesis.

Cell biology – Eukaryote symbiosis

The subcellular isotopic imaging capabilities of the NanoSIMS open up a multitude of new research opportunities in cell biology of higher organisms, including drug delivery. The principles are illustrated with a study of another symbiotic organism, the reef-building coral, most species of which host endosymbiotic photosynthesising algae, often referred to as dinoflagellates or zooxanthellae. Assimilation of inorganic nitrogen from nutrient-poor tropical seas is an essential challenge for this endosymbiosis. Despite the clear evidence that reef-building corals can use ammonium as an inorganic nitrogen source, the dynamics and precise roles of host and symbionts in this fundamental process remain unclear.

As illustrated above and in Figure 24, the NanoSIMS can provide direct imaging of metabolic exchanges within an intact symbiosis. In Figure 24, the NanoSIMS images demonstrate the capabilities of both dinoflagellate and animal cells (in this case, the reef-building coral *Acropora aspera*) to fix nitrogen from seawater enriched in $^{15}NH_4$ (ammonium; Pernice *et al.* 2012). However, quantification of $^{15}N/^{14}N$ ratios obtained from the different tissue layers in the host organism and from the photosynthesising algae, respectively, shows that the latter can fix about 20 times more nitrogen than the coral host cells in response to a sudden pulse of sea water enriched in ammonium. Given the importance of N in cell maintenance, growth and functioning, ammonium assimilation facilitated primarily by the symbiont algae may have been a key to the evolutionary success of reef-building corals in nutrient-poor waters.

A technically important aspect included in this example (Figure 24) is the direct comparison between the NanoSIMS isotopic maps and the cell images obtained by TEM. In even higher-resolution NanoSIMS images, it is possible to resolve all histological compartments of a eukaryote cell, including nucleus, mitochondria, Golgi apparatus, etc., which can provide important clues to the pathways of isotopically labelled molecules inside these cells.

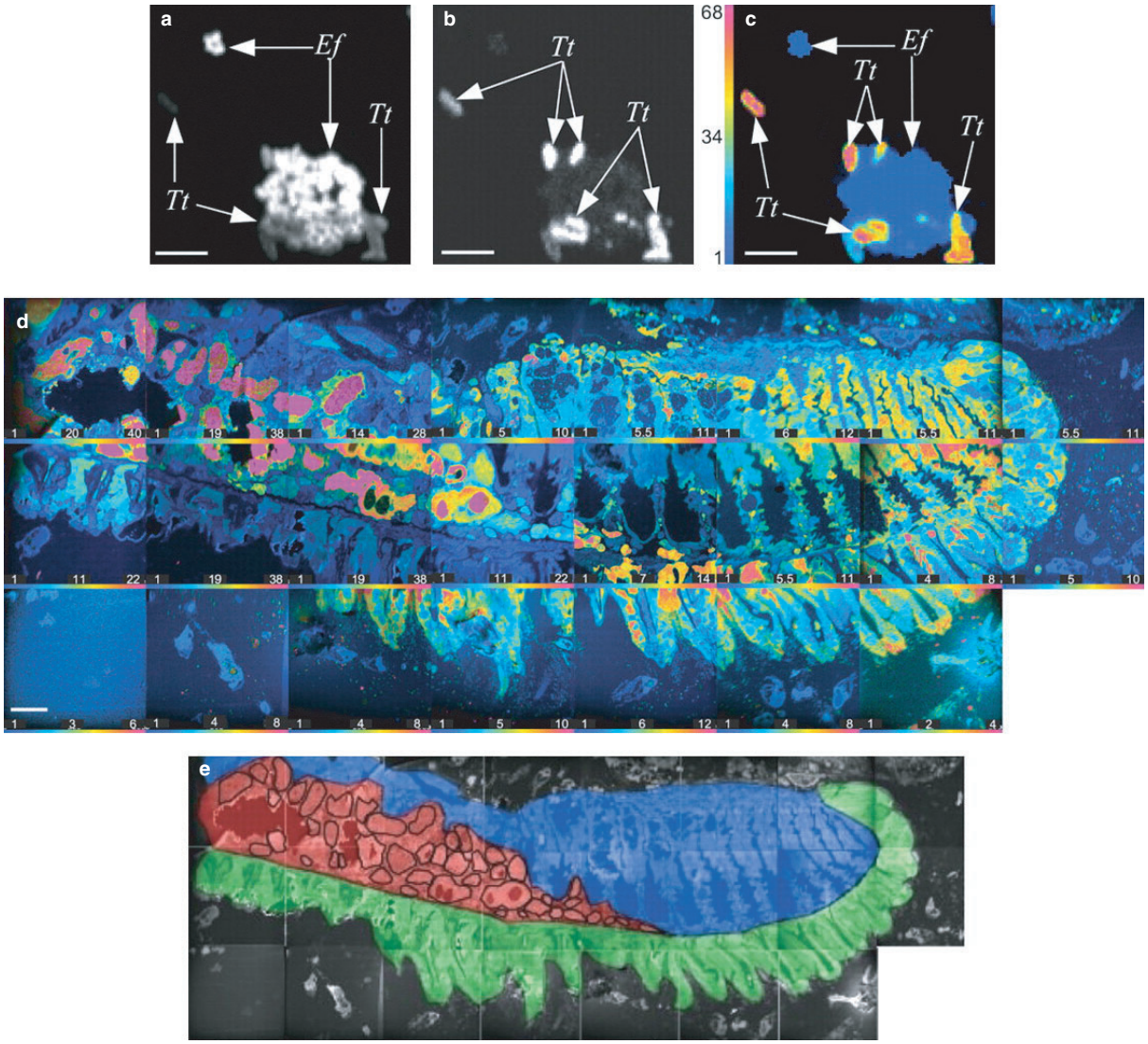

Figure 23. N fixation by *Teredinibacter turnerae* bacteria and by bacterial symbionts within the marine bivalve *Lyrodus pedicellatus*. (a and b) Parallel isotopic maps of a field of view containing *T. turnerae* (*Tt*) and *Enterococcus faecalis* (*Ef*). (a) $^{12}C^{14}N^-$. (b) $^{12}C^{15}N^-$. (c) The colour-coded ratio between a and b. The images consist of 256 × 256 pixels, and acquisition time was 30 min. Scale bar is 5 μm. (d) Mosaic of colour-coded $^{12}C^{15}N^-/^{12}C^{14}N^-$ ratio maps. Each tile is 100 μm × 100 μm, 256 × 256 pixels and with acquisition times of 120 min per tile. Scale bar is 25 μm. The colours represent different levels of ^{15}N enrichment, from blue (normal, unlabelled N isotopic compositions) to magenta in regions highly enriched in ^{15}N by a factor indicated in the colour bars for each tile. (e) Cartoon of the isotopic map in (d) outlining the locations of the gland of Deshayes (red), interlamellar junctions (blue), ctenidial filaments (green) and bacteriocytes (outlines). In (c), the highest ^{15}N incorporation is seen in *T. turnerae* and none on *E. faecalis*. In (d), the highest ^{15}N incorporation is seen in bacteriocytes of the gland of Deshayes. From Lechene *et al.* (2007). Reprinted with permission from AAAS.

Plants and soils

The use of NanoSIMS in the study of environmental contaminants and/or chemical hazards is illustrated here with the example of arsenic (As), a toxic element for humans with a poorly defined threshold below which it is not carcinogenic (Smith *et al.* 2002). Recent studies have shown that rice is a major source of inorganic As in diets where rice is a staple food (Mondal and Polya 2008). Understanding the uptake and sequestration of As into the rice plant is therefore important for developing strategies to reduce As concentrations in rice grains. Moore *et al.* (2011) used the

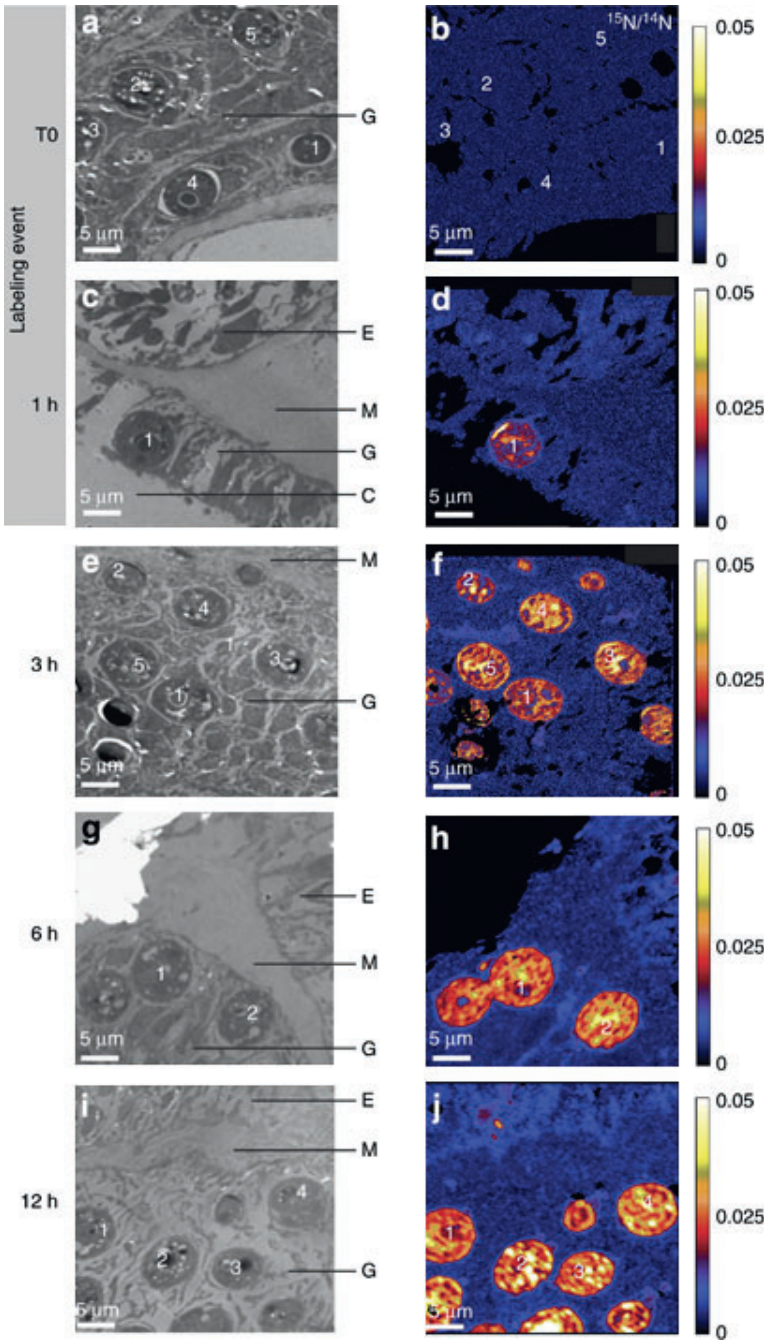

Figure 24. Imaging of ^{15}N–ammonium uptake within the reef-building coral *Acropora aspera*. (a, c, e, g, i) TEM images and (b, d, f, h, j) distribution of $^{15}N/^{14}N$ as measured by NanoSIMS in the same sections of *A. aspera* tissue during the time series of the pulse-chase labelling experiment. (a–b) t = 0, no label; (c–d) t = 1 hr; (e–f) t = 3 hr; (g–h) t = 6 hr; and (i–j) t=12 hr. Individual dinoflagellate symbionts that have absorbed ^{15}N are clearly visible within the coral gastrodermal tissue after 1 hr. C, Coelenteron; G, gastroderm; E, epiderm; M, mesoglea. For each NanoSIMS image, the increase in $^{15}N/^{14}N$ ratio of each individual dinoflagellate symbionts is indicated by the colour code. Reprinted by permission from MacMillan Publishers Ltd: The ISME Journal (Pernice *et al.* 2012), © 2012.

NanoSIMS to investigate the distribution of As and silicon (Si) in rice roots, having documented distinct subcellular distributions of As and Si between the roots of rice plants with and without the Si/As efflux transporter Lsi2 and a wild type. Mutation of the Lsi2 transporter results in stronger vacuolar accumulation of As in the endodermal cells (Figure 25) compared with the wild type, where pericycle (primary tissue located at the periphery of the root vascular cylinder) accumulation is observed. Vacuolar accumulation of As is also observed to be associated with sulfur, suggesting that As may be stored as arsenite–phytochelatin complexes in which it is being detoxified. Silicon is localised at the cell walls of the endodermal cells (Figure 25) with little apparent effect of the Lsi2 mutation on its distribution.

These observations provide yet another example of the precise comparison that is possible between NanoSIMS images and TEM images of the same cell structures.

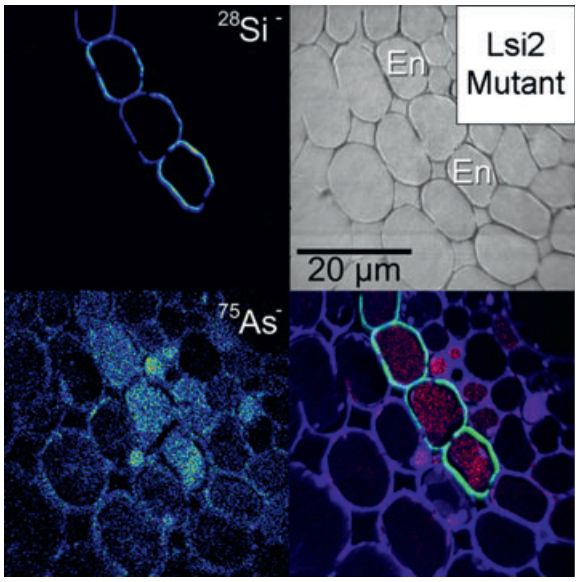

Figure 25. NanoSIMS $^{28}Si^-$ and $^{75}As^-$ ion images and secondary electron image from the central region of a rice root treated with arsenate with a mutation in the Lsi2 silicon transporter. Arsenic accumulation was observed in the vacuoles of the endodermal cells, where the Lsi2 transporter is localised and silicon was localised around the same cells. The colour merge shows the relative locations $^{75}As^-$ (red), $^{28}Si^-$ (green) and $^{12}C^{14}N^-$ (blue, not shown as original NanoSIMS image). En, endodermis. Figure courtesy Katie Moore.

Biomineralisation

For more than a century, it has been known that both eukaryotes and prokaryotes can induce and/or control the formation of minerals, and the diversity in chemistry, morphology, structure and function of biominerals is enormous. Biominerals are major components in the global geochemical cycle (e.g., silica and radiolarians), form skeletons (e.g., hydroxyapatite in bones, calcium carbonate in shells) and serve as storage media for essential nutrients and toxic elements (detoxification). Biominerals can induce diseases in humans (e.g., calcification in urinary tracts and in arteries) and are used extensively as time markers in sedimentology, as proxies for temperature and salinity in palaeoclimatology (e.g., foraminifera, corals) and as indicators of ancient life forms (e.g., stromatolites). Additionally, biominerals can display unique material properties that find use in nanotechnologies. Yet, surprisingly little is known about the exact processes by which organisms initiate, control and stop the growth of minerals and how the external environment influences their composition. Analytical tools that can provide chemical, structural and isotopic information at these length scales have been lacking so far. The NanoSIMS is providing the study of biominerals with a multitude of new opportunities, of which just one is illustrated in this last example.

Gorzelak *et al.* (2011) used a NanoSIMS to study the regeneration of broken calcium carbonate spines of the sea urchin *Paracentrotus lividus* with two labelling events in which the stable isotope ^{26}Mg was added to the surrounding sea water. These two labelling events, lasting 72 and 24 hr, respectively, and separated in time by 3 days, resulted in calcium carbonate with clearly visible enrichments in the $^{26}Mg/^{44}Ca$ ratio (Figure 26). The isotope maps provide direct, quantified information about the dynamics of the biomineralisation process. In these structures, stereom trabeculae initially grow as conical microspines, which form within < 1 day. Lateral growth then takes place allowing adjacent microspines to join by forming a horizontal 'bridge' (Figure 26d). This process is very fast and seems to occur several times per day. While new trabeculae form, the older trabeculae already connected in a thin meshwork thicken simultaneously and very slowly at an approximate rate of about 1 µm day^{-1} (Figure 26b–f). This thickening process includes both microspines and bridges (Figure 26b–f). The overall longitudinal growth rate of the inner stereom is *ca.* 125 µm day^{-1}.

This work is a good example of how the dynamics of biomineral formation can be imaged with very high spatial and temporal resolution at different structural length scales without imposing unnecessary stress to the organism under study. The possibilities for combining NanoSIMS imaging with isotopic or trace element labelling experiments to understand better the workings of living organisms seem endless.

Conclusions and outlook

It is our hope that this review has given the reader a better idea of the operation of an ion probe and of the special strengths of the NanoSIMS instrument. With its superior spatial resolution, high sensitivity and multi-collection capability, the NanoSIMS has become an indispensable tool for many studies in cosmochemistry and biological geochemistry. The ability to do high-resolution ion imaging at the sub-micrometre scale has led to new discoveries, for example, the detection of presolar (stardust) silicates in primitive solar system materials, and is sure to continue to do so in the years to come, especially as the technology becomes more integrated in the biological and life sciences. In general, the NanoSIMS ion probe is the instrument of choice if quantitative ion imaging at the sub-micrometre scale is required. For isotope studies that require precision at the sub-per mil level,

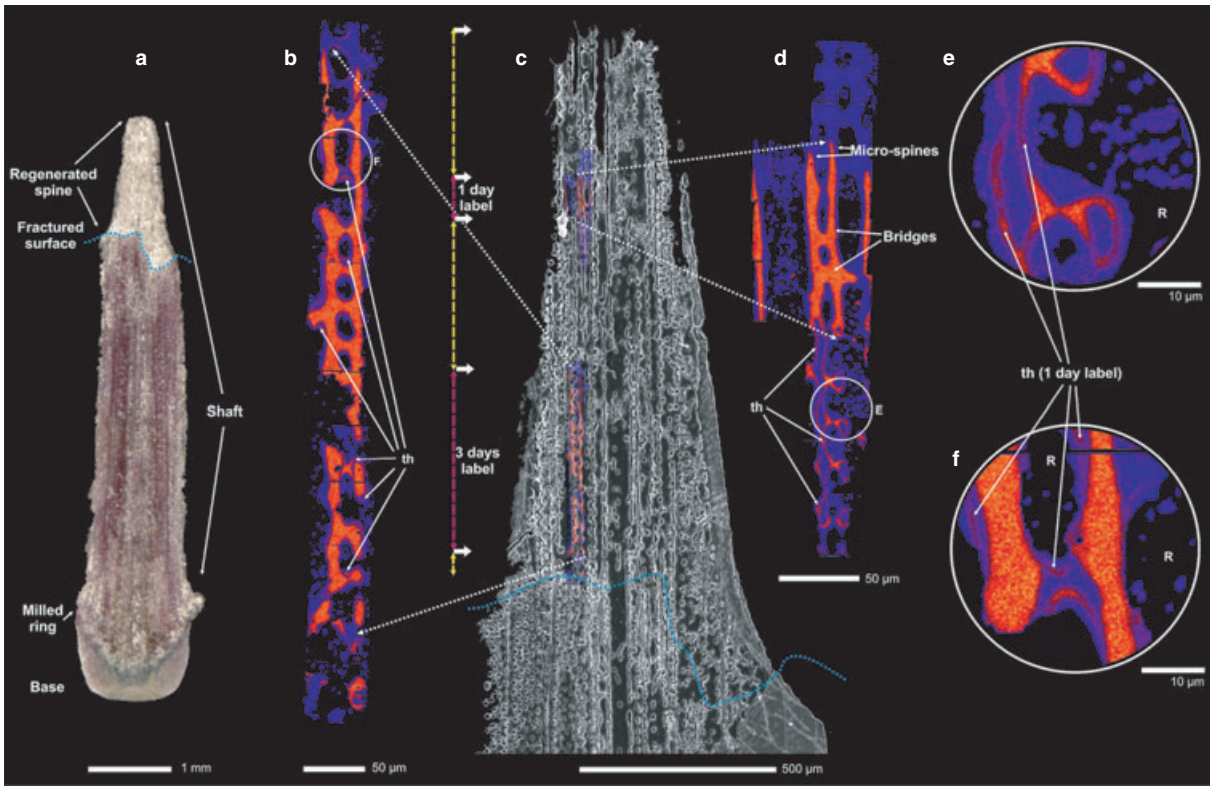

Figure 26. (a) Lateral view of investigated spine of *Paracentrotus lividus* with regenerated fragment of apical part. (c) Lateral view (scanning electron microscope) of a polished and Au-coated section of spine combined with NanoSIMS images showing two labelling events (dotted arrows show position of NanoSIMS images enlarged in b, d). Etching and SEM observations were performed after the NanoSIMS imaging. (b) NanoSIMS image of the $^{26}Mg/^{44}Ca$ distribution in labelled skeleton during first (3-day) labelling event. (d) NanoSIMS image of the $^{26}Mg/^{44}Ca$ distribution in labelled skeleton during second 1-day labelling event. Blue regions indicate growth in normal (i.e., unlabelled) artificial sea water with normal $^{26}Mg/^{44}Ca$ ratio. Red–yellow regions indicate enhanced $^{26}Mg/^{44}Ca$ ratio due to the ^{26}Mg labelling. (e, f) Enlargements of the stereom showing the 1-day thickening process ('th' and arrows) during the second labelling event on the previously formed skeleton. 'R' marks resin-filled pores. Reprinted from Gorzelak *et al.* (2011), © 2011, with permission from Elsevier.

other instruments, such as the Cameca IMS 1270/1280 and SHRIMP ion probes, are preferred, but their analytical precision comes at the expense of spatial resolution.

It is hoped that future developments will lead to an improvement in the achievable beam size of the negative oxygen ion source, which is currently limited to about 200 nm (optimum conditions) and 400 nm (routine operation), respectively. This would permit the study of alkali, alkali earth and transition metals with a spatial resolution better than 100 nm, similar to the resolution obtained for H, C, N, O, Si and S isotopes, which are measured with the positive caesium ion source. Higher useful yields would also be desirable. In theory, this would be possible if laser resonance ionisation could be implemented. The design of the ion optics in the NanoSIMS renders such improvements difficult, however. In any case, in its current incarnation, the NanoSIMS represents an extremely powerful new analytical technique. Scientists from different disciplines are just beginning to appreciate its potential. We hope our review can help push this development further along.

Acknowledgements

PH wishes to thank the late Frank Stadermann for his close cooperation, joint visits to Cameca and his great helpfulness during the development and early phase of operation of the NanoSIMS. PH also wishes to thank Ernst Zinner for the introduction into the field of ion probe mass spectrometry, Guenter Lugmair for his efforts to get the NanoSIMS to the Max Planck Institute for Chemistry and François Hillion for a

fruitful collaboration over many years. AM thanks Joe Wooden (USGS) for teaching him the métier of ion microprobe analyses. We gratefully acknowledge constructive and helpful comments by three anonymous reviewers, the Guest Editor Klaus Peter Jochum and François Hillion. This work was supported in part by the European Research Council Advanced Grant 246749 (BIOCARB) to AM.

References

Audinot J.-N., Guignard C., Migeon H.-N. and Hoffmann L. (2006)
Study of the mechanism of diatom cell division by means of ^{29}Si isotope tracing. **Applied Surface Science, 252**, 6813–6815.

Audinot J.-N., Senou M., Migeon H.-N. and Many M.C. (2008)
Visualisation of thyroid hormone synthesis by ion imaging. **Applied Surface Science, 255**, 1185–1189.

Azari F., Vali H., Guerquin-Kern J.-L., Wu T.-D., Croisy A., Sears S.K., Tabrizian M. and McKee M.D. (2008)
Intracellular precipitation of hydroxyapatite mineral and implications for pathologic calcification. **Journal of Structural Biology, 162**, 468–479.

Beck P., Gillet P., El Goresy A. and Mostefaoui S. (2005)
Timescales of shock processes in chondritic and martian meteorites. **Nature, 435**, 1071–1074.

Behrens S., Loesekann T., Pett-Ridge J., Weber P.K., Ng W.-O., Stevenson B.S., Hutcheon I.D., Relman D.A. and Spormann A.M. (2008)
Linking microbial phylogeny to metabolic activity at the single-cell level by using enhanced element labeling-catalyzed reporter deposition fluorescence *in situ* hybridization (EL-FISH) and NanoSIMS. **Applied and Environmental Microbiology, 74**, 3143–3150.

Benninghoven A., Rüdenauer F.G. and Werner H.W. (1987)
Secondary ion mass spectrometry: Basic concepts, instrumental aspects, applications and trends. **Wiley (New York)**, 1227pp.

Bernatowicz T., Fraundorf G., Ming T., Anders E., Wopenka B., Zinner E. and Fraundorf P. (1987)
Evidence for interstellar SiC in the Murray carbonaceous meteorite. **Nature, 330**, 728–730.

Besmehn A. and Hoppe P. (2003)
A NanoSIMS study of Si- and Ca-Ti-isotopic compositions of presolar silicon carbide grains from supernovae. **Geochimica et Cosmochimica Acta, 67**, 4693–4703.

Bose M., Floss C. and Stadermann F.J. (2010)
An investigation into the origin of Fe-rich presolar silicates in Acfer 094. **Astrophysical Journal, 714**, 1624–1636.

Brahmi C., Domart-Coulon I., Rougee L., Pyle D.G., Stolarski J., Mahoney J.J., Richmond R.H., Ostrander G.K. and Meibom A. (2012b)
Pulsed ^{86}Sr-labeling and NanoSIMS imaging to study coral biomineralization at ultra-structural length scales. **Coral Reefs, 31**, 741–752.

Brahmi C., Kopp C., Domart-Coulon I., Stolarski J. and Meibom A. (2012a)
Skeletal growth dynamics linked to trace-element composition in the scleractinian coral *Pocillopora damicornis*. **Geochimica et Cosmochimica Acta, 99**, 146–158.

Brahmi C., Meibom A., Smith D.C., Stolarski J., Auzoux-Bordenave S., Nouet J., Doumenc D., Djediat C. and Domart-Coulon I. (2010)
Skeletal growth, ultrastructure and composition of the azooxanthellate scleractinian coral *Balanophyllia regia*. **Coral Reefs, 29**, 175–189.

Briani G., Gounelle M., Marrocchi Y., Mostefaoui S., Leroux H., Quirico E. and Meibom A. (2009)
Pristine extraterrestrial material with unprecedented nitrogen isotopic variation. **PNAS, 106**, 10522–10527.

Busemann H., Nguyen A.N., Cody G., Hoppe P., Kilcoyne A.L.D., Stroud R.M., Zega T.J. and Nittler L.R. (2009)
Ultra-primitive interplanetary dust particles from the comet 26P/Grigg-Skjellerup dust stream collection. **Earth and Planetary Science Letters, 288**, 44–57.

Busemann H., Young A.F., Alexander C.M.O.D., Hoppe P., Mukhopadhyay S. and Nittler L.R. (2006)
Interstellar chemistry recorded in organic matter from primitive meteorites. **Science, 312**, 727–730.

Byrne M.E., Ball D.A., Guerquin-Kern J.-L., Rouiller I., Wu T.-D., Downing K.H., Vali H. and Komeili A. (2010)
Desulfovibrio magneticus RS-1 contains an iron- and phosphorus-rich organelle distinct from its bullet-shaped magnetosomes. **Proceedings of the National Academy of Sciences of the United States of America, 107**, 12263–12268.

Cabin-Flaman A., Monnier A.-F., Coffinier Y., Audinot J.-N., Gibouin D., Wirtz T., Boukherroub R., Migeon H.-N., Bensimon A., Jannière L., Ripoll C. and Norris V. (2011)
Combed single DNA molecules imaged by secondary ion mass spectrometry. **Analytical Chemistry, 83**, 6940–6947.

Clement S.W.J., Compston W. and Newstead G. (1977).
Design of a large, high resolution ion microprobe. **International Secondary Ion Mass Spectrometry Conference, Springer (Münster)**.

Clode P.L., Kilburn M.R., Jones D.L., Stockdale E.A., Cliff J.B. III, Herrmann A.M. and Murphy D.V. (2009)
In situ mapping of nutrient uptake in the rhizosphere using nanoscale secondary ion mass spectrometry. **Plant Physiology, 151**, 1751–1757.

Clode P.L., Stern R.A. and Marshall A.T. (2007)
Subcellular imaging of isotopically labeled carbon compounds in a biological sample by ion microprobe (NanoSIMS). **Microscopy Research and Technique, 70**, 220–229.

references

Coplen T.B., Hopple J.A., Böhlke J.K., Peiser H.S., Rieder S.E., Krouse H.R., Rosman K.J.R., Ding T., Vocke R.D. Jr, Révész K.M., Lamberty A., Taylor P. and De Bièvre P. (2006)
Compilation of minimum and maximum isotope ratios of selected elements in naturally occurring terrestrial materials and reagents. U.S. Geological Survey, Water Resources Investigations Report 01-4222, 98pp.

Dauphas N., Remusat L., Chen J.H., Roskosz M., Papanastassiou D.A., Stodolna J., Guan Y., Ma C. and Eiler J.M. (2010)
Neutron-rich chromium isotope anomalies in supernova ejecta. Astrophysical Journal, 720, 1577–1591.

Dauphin Y., Ball A.D., Cotte M., Cuif J.-P., Meibom A., Salome M., Susini J. and Williams C.T. (2008)
Structure and composition of the nacre-prisms transition in the shell of *Pinctada margaritifera* (Mollusca, Bivalvia). Analytical and Bioanalytical Chemistry, 390, 1659–1669.

Dauphin Y., Brunelle A., Cotte M., Cuif J.-P., Farre B., Laprevote O., Meibom A., Salome M. and Williams C.T. (2010)
A layered structure in the organic envelopes of the prismatic layer of the shell of the Pearl Oyster *Pinctada margaritifera* (Mollusca, Bivalvia). Microscopy and Microanalysis, 16, 91–98.

De Gregorio B.T., Stroud R.M., Nittler L.R., Alexander C.M.O.D., Kilcoyne A.L.D. and Zega T.J. (2010)
Isotopic anomalies in organic nanoglobules from Comet 81P/Wild 2: Comparison to Murchison nanoglobules and isotopic anomalies induced in terrestrial organics by electron irradiation. Geochimica et Cosmochimica Acta, 74, 4454–4470.

Duprat J., Dobrică E., Engrand C., Aléon J., Marrocchi Y., Mostefaoui S., Meibom A., Leroux H., Rouzaud J.-N., Gounelle M. and Robert F. (2010)
Extreme deuterium excesses in ultracarbonaceous micrometeorites from central Antarctic snow. Science, 328, 742–745.

Eybe T., Audinot J.N., Bohn T., Guignard C., Migeon H.N. and Hoffmann L. (2008)
NanoSIMS 50 elucidation of the natural element composition in structures of cyanobacteria and their exposure to halogen compounds. Journal of Applied Microbiology, 105, 1502–1510.

Finzi-Hart J.A., Pett-Ridge J., Weber P.K., Popa R., Fallon S.J., Gunderson T., Hutcheon I.D., Nealson K.H. and Capone D.G. (2009)
Fixation and fate of C and N in the cyanobacterium *Trichodesmium* using nanometre-scale secondary ion mass spectrometry. Proceedings of the National Academy of Sciences of the United States of America, 106, 6345–6350.

Floss C. and Stadermann F. (2009)
Auger nanoprobe analysis of presolar ferromagnesian silicate grains from primitive CR chondrites QUE 99177 and MET 00426. Geochimica et Cosmochimica Acta, 73, 2415–2440.

Floss C., Stadermann F.J., Bradley J., Dai Z.R., Bajt S. and Graham G. (2004)
Carbon and nitrogen isotopic anomalies in an anhydrous interplanetary dust particle. Science, 303, 1355–1358.

Floss C., Stadermann F.J., Bradley J.P., Dai Z.R., Bajt S., Graham G. and Lea A.S. (2006)
Identification of isotopically primitive interplanetary dust particles: A NanoSIMS isotopic imaging study. Geochimica et Cosmochimica Acta, 70, 2371–2399.

Floss C., Stadermann F.J., Kearsley A.T., Burchell M.J. and Ong W.J. (2013)
The abundance of presolar grains in comet 81 P/Wild 2. Astrophysical Journal, 763, 140 (11pp).

Foster R.A., Kuypers M.M.M., Vagner T., Paerl R.W., Musat N. and Zehr J.P. (2011)
Nitrogen fixation and transfer in open ocean diatom-cyanobacterial symbioses. The ISME Journal, 5, 1484–1493.

Fujiya W., Hoppe P. and Ott U. (2011)
Hints for neutrino-process boron in presolar silicon carbide grains from supernovae. Astrophysical Journal, 730, L7–L11.

Fujiya W., Sugiura N., Hotta H., Ichimura K. and Sano Y. (2012)
Evidence for the late formation of hydrous asteroids from young meteoritic carbonates. Nature Communications, 3, 627.

Gagnon A.C., Adkins J.F. and Erez J. (2012)
Seawater transport during coral biomineralization. Earth and Planetary Science Letters, 329, 150–161.

Georgantzopoulou A., Balachandran Y.L., Rosenkranz P., Dusinska M., Lankoff A., Wojewodzka M., Kruszewski M., Guignard C., Audinot J.-N., Girija S., Hoffmann L. and Gutleb A.C. (2012)
Ag nanoparticles: Size- and surface-dependent effects on model aquatic organisms and uptake evaluation with NanoSIMS. Nanotoxicology, doi:10.3109/17435390.2012.715312.

Gormanns P., Reckow S., Poczatek J.C., Turck C.W. and Lechene C. (2012)
Segmentation of multi-isotope imaging mass spectrometry data for semi-automatic detection of regions of interest. PLoS ONE, 7, e30576.

Gorzelak P., Stolarski J., Dubois P., Kopp C. and Meibom A. (2011)
^{26}Mg labeling of the sea urchin regenerating spine: Insights into echinoderm biomineralization process. Journal of Structural Biology, 176, 119–126.

Gorzelak P., Stolarski J., Mazur M. and Meibom A. (2012)
Micro- to nanostructure and geochemistry of extant crinoidal echinoderm skeletons. Geobiology, 11, 29–43.

Gröner E. and Hoppe P. (2006)
Automated ion imaging with the NanoSims ion microprobe. Applied Surface Science, 252, 7148–7151.

references

Guerquin-Kern J.-L., Hillion F., Madelmont J.-C., Labarre P., Papon J. and Croisy A. (2004)
Ultra-structural cell distribution of the melanoma marker iodobenzamide: Improved potentiality of SIMS imaging in life sciences. **Biomedical Engineering Online**, **3**, 10.

Gyngard F., Amari S., Zinner E. and Ott U. (2009)
Interstellar exposure ages of large presolar SiC grains from the Murchison meteorite. **Astrophysical Journal**, **694**, 359–366.

Gyngard F., Zinner E., Nittler L.R., Morgand A., Stadermann F.J. and Hynes K.M. (2010)
Automated NanoSIMS measurements of spinel stardust from the Murray meteorite. **Astrophysical Journal**, **717**, 107–120.

Hallegot P., Audinot J.N. and Migeon H.N. (2006)
Direct NanoSIMS imaging of diffusible elements in surfaced block of cryo-processed biological samples. **Applied Surface Science**, **252**, 6706–6708.

Hashizume K., Takahata N., Naraoka H. and Sano Y. (2011)
Extreme oxygen isotope anomaly with a solar origin detected in meteoritic organics. **Nature Geoscience**, **4**, 165–168.

Hauri E., Weinreich T., Saal A.E., Rutherford M.C. and Van Orman J.A. (2011)
High pre-eruptive water contents preserved in lunar melt inclusions. **Science**, **333**, 213–215.

Hillion F., Daigne B., Girard F. and Slodzian G. (1993)
A new high performance SIMS instrument: The Cameca "Nanosims 50". **In: Benninghoven A., Nihei Y., Shimizu R. and Werner H.W. (eds), Secondary Ion Mass Spectrometry SIMS IX. Wiley (Chichester)**, 254–257.

Hillion F., Daigne B., Girard F. and Slodzian G. (1995)
The CAMECA "NANOSIMS 50" experimental results. **In: Benninghoven A., Hagenhoff B. and Werner H.W. (eds), Secondary Ion Mass Spectrometry SIMS X. Wiley (Chichester)**, 979–982.

Hillion F., Kilburn M.R., Hoppe P., Messenger S. and Weber P.K. (2008)
The effect of QSA on S, C, O and Si. **Geochimica et Cosmochimica Acta**, **72**, A377.

Hoppe P. (2008)
Reservoir for comet material: Circumstellar grains. **Space Science Reviews**, **138**, 43–57.

Hoppe P. (2011)
Measurements of presolar grains. Proceedings of the 11th Symposium on Nuclei in the Cosmos (NIC XI). July 19–23, 2010 Heidelberg, Germany. Available online at http://pos.sissa.it/cgi-bin/reader/conf.cgi?confid=100#session-121.

Hoppe P., Fujiya W. and Zinner E. (2012)
Sulfur molecule chemistry in supernova ejecta recorded by silicon carbide stardust. **Astrophysical Journal**, **745**, L26.

Hoppe P., Leitner J., Gröner E., Marhas K.K., Meyer B.S. and Amari S. (2010)
NanoSIMS studies of small presolar SiC grains: New insights into supernova nucleosynthesis, chemistry and dust formation. **Astrophysical Journal**, **719**, 1370–1384.

Hoppe P., Macdougall D. and Lugmair G.W. (2007)
High spatial resolution ion microprobe measurements refine chronology of carbonate formation in Orgueil. **Meteoritics and Planetary Science**, **42**, 1309–1320.

Hoppe P., Mostefaoui S. and Stephan T. (2005)
NanoSIMS oxygen and sulfur isotope imaging of primitive Solar System materials. **Lunar and Planetary Science**, **36**, abstract #1301.

Houlbreque F., Meibom A., Cuif J.-P., Stolarski J., Marrocchi Y., Ferrier-Pages C., Domart-Coulon I. and Dunbar R.B. (2009)
Strontium-86 labeling experiments show spatially heterogeneous skeletal formation in the scleractinian coral *Porites porites*. **Geophysical Research Letters**, **36**, L04604.

Huss G.R., Nagashima K., Jurewicz A.J.G., Burnett D.S. and Olinger C.T. (2012)
The isotopic composition and fluence of solar-wind nitrogen in a genesis B/C array collector. **Meteoritics and Planetary Science**, **47**, 1436–1448.

Hynes K.M. and Gyngard F. (2009)
The presolar grain data base: http://presolar.wustl.edu/~pgd. **Lunar and Planetary Science**, **40**, abstract #1398.

Ireland T.R. (1995)
Ion microprobe mass spectrometry: Techniques and applications in cosmochemistry, geochemistry and geochronology. **In: Rowe M. and Hyman M. (ed.), Advances in analytical geochemistry. JAI Press (Greenwich)**, 1–118.

Ito M. and Messenger S. (2008)
Isotopic imaging of refractory inclusions in meteorites with the NanoSIMS 50L. **Applied Surface Science**, **255**, 1446–1450.

Ito M. and Messenger S. (2009)
Rare earth element measurements of melilite and fassaite in Allende CAI by NanoSIMS. **Meteoritics and Planetary Science**, **44**, A97.

Ito M., Messenger S., Keller L.P., Rahman Z.U., Ross D.K. and Nakamura-Messenger K. (2010)
FIB-NanoSIMS-TEM coordinated study of a Wark-Lovering rim in a Vigarano Type A CAI. **Lunar and Planetary Science**, **41**, abstract #1177.

Jacobsen B., Matzel J., Hutcheon I.D., Krot A.N., Yin Q., Nagashima K., Ramon E.C., Weber P.K., Ishii H.A. and Ciesla F. (2011)
Formation of the short-lived radionuclide ^{36}Cl in the protoplanetary disk during late-stage irradiation of a volatile-rich reservoir. **Astrophysical Journal**, **731**, L28.

Jadhav M., Amari S., Marhas K.K., Zinner E. and Maruoka T. (2008)
New stellar sources for high-density, presolar graphite grains. **Astrophysical Journal**, **682**, 1479–1485.

references

Kilburn M.R. and Wacey D. (2011)
Elemental and isotopic analysis by NanoSIMS: Insights for the study of stromatolites and early life on Earth. In: Tewari V. and Seckbach J. (eds), Stromatolites: Interaction of microbes with sediments. Springer (Netherlands), 463–493.

Kita N.T., Huberty J.M., Kozdon R., Beard B.L. and Valley J.W. (2011)
High-precision SIMS oxygen, sulfur and iron stable isotope analyses of geological materials: Accuracy, surface topography and crystal orientation. Surface and Interface Analysis, 43, 427–431.

Kleinfeld A.M., Kampf J.P. and Lechene C. (2004)
Transport of C-13-oleate in adipocytes measured using multi imaging mass spectrometry. Journal of the American Society for Mass Spectrometry, 15, 1572–1580.

Kodolanyi J. and Hoppe P. (2011)
A promising method to obtain more accurate Mg and Fe isotope compositional data on presolar silicate particles. Proceedings of the 11th Symposium on Nuclei in the Cosmos (NIC XI). July 19–23, 2010 Heidelberg, Germany. Available online at http://pos.sissa.it/cgi-bin/reader/conf.cgi?confid=100#session-121.

Kopp C., Meibom A., Beyssac O., Stolarski J., Djediat S., Szlachetko J. and Domart-Coulon I. (2011)
Calcareous sponge biomineralization: Ultrastructural and compositional heterogeneity of spicules in *Leuconia johnstoni* Carter, 1871. Journal of Structural Biology, 173, 99–109.

Lau K.H., Christlieb M., Schroeder M., Sheldon H., Harris A.L. and Grovenor C.R.M. (2010)
Development of a new bimodal imaging methodology: A combination of fluorescence microscopy and high-resolution secondary ion mass spectrometry. Journal of Microscopy, 240, 21–31.

Lechene C., Hillion F., McMahon G., Benson D., Kleinfeld A.M., Kampf J.P., Distel D., Luyten Y., Bonventre J., Hentschel D., Park K., Ito S., Schwartz M., Benichou G. and Slodzian G. (2006)
High-resolution quantitative imaging of mammalian and bacterial cells using stable isotope mass spectrometry. Journal of Biology, 5, 20.

Lechene C.P., Lee G.Y., Poczatek J.C., Toner M. and Biggers J.D. (2012)
3D Multi-isotope imaging mass spectrometry reveals penetration of O-18-trehalose in mouse sperm nucleus. PLoS ONE, 7, e42267.

Lechene C.P., Luyten Y., McMahon G. and Distel D.L. (2007)
Quantitative imaging of nitrogen fixation by individual bacteria within animal cells. Science, 317, 1563–1566.

Leitner J., Hoppe P. and Heck P.R. (2010)
First discovery of presolar material of possible supernova origin in impact residues from comet 81P/Wild 2. Lunar and Planetary Science, 41, abstract #1607.

Leitner J., Vollmer C., Hoppe P. and Zipfel J. (2012)
Characterization of presolar material in the CR chondrite Northwest Africa 852. Astrophysical Journal, 745, 38.

Lepareur M. (1980)
Le micro-analyseur ionique de seconde génération Cameca, modele 3F. Revue Technique Thomson-CSF, 12, 225–265.

Li T., Wu T.-D., Mazeas L., Toffin L., Guerquin-Kern J.-L., Leblon G. and Bouchez T. (2008)
Simultaneous analysis of microbial identity and function using NanoSIMS. Environmental Microbiology, 10, 580–588.

Lin Y., Gyngard F. and Zinner E. (2010)
Isotopic analysis of supernova SiC and Si_3N_4 grains from the Qingzhen (EH3) chondrite. Astrophysical Journal, 709, 1157–1173.

Ma Y., Aichmayer B., Paris O., Fratzl P., Meibom A., Metzler R.A., Politi Y., Addadi L., Gilbert P.U.P.A. and Weiner S. (2009)
The grinding tip of the sea urchin tooth exhibits exquisite control over calcite crystal orientation and Mg distribution. Proceedings of the National Academy of Sciences of the United States of America, 106, 6048–6053.

Marhas K.K., Amari S., Gyngard F., Zinner E. and Gallino R. (2008)
Iron and nickel isotopic ratios in presolar SiC grains. Astrophysical Journal, 689, 622–645.

Marhas K.K., Hoppe P. and Ott U. (2007)
NanoSIMS studies of Ba isotopic compositions in single presolar silicon carbide grains from AGB stars and supernovae. Meteoritics and Planetary Science, 42, 1077–1101.

Marty B., Chaussidon M., Wiens R.C., Jurewicz J.G. and Burnett D.S. (2011)
A ^{15}N-poor isotopic composition for the solar system as shown by Genesis solar wind samples. Science, 332, 1533–1536.

Matrajt G., Messenger S., Brownlee D. and Joswiak D. (2012)
Diverse forms of primordial organic matter identified in interplanetary dust particles. Meteoritics and Planetary Science, 47, 525–549.

Matzel J., Ishii H.A., Joswiak D., Hutcheon I.D., Bradley J.P., Brownlee D., Weber P.K., Teslich N., Matrajt G., McKeegan K.D. and MacPherson G.J. (2010)
Constraints on the formation age of cometary material from the NASA Stardust mission. Science, 328, 483–486.

Mayali X., Weber P.K., Brodie E.L., Mabery S., Hoeprich P.D. and Pett-Ridge J. (2012)
High-throughput isotopic analysis of RNA microarrays to quantify microbial resource use. The ISME Journal, 6, 1210–1221.

references

McKeegan K.D., Aléon J., Bradley J., Brownlee D., Busemann H., Butterworth A., Chaussidon M., Fallon S., Floss C., Gilmour J., Gounelle M., Graham G., Guan Y., Heck P.R., Hoppe P., Hutcheon I.D., Huth J., Ishii H., Ito M., Jacobsen S.B., Kearsley A., Leshin L.A., Liu M.-C., Lyon I., Marhas K., Marty B., Matrajt G., Meibom A., Messenger S., Mostefaoui S., Mukhopadhyay S., Nakamura-Messenger K., Nittler L., Palma R., Pepin R.O., Papanastassiou D.A., Robert F., Schlutter D., Snead C.J., Stadermann F.J., Stroud R., Tsou P., Westphal A. and Young E.D., Ziegler K., Zimmermann L. and Zinner E. (2006)
Isotopic compositions of cometary matter returned by Stardust. Science, 314, 1724–1728.

Meeks J.C. and Elhai J. (2002)
Regulation of cellular differentiation in filamentous cyanobacteria in free-living and plant-associated symbiotic growth states. Microbiology and Molecular Biology Reviews, 66, 94–121.

Meibom A., Cuif J.-P., Hillion F.O., Constantz B.R., Juillet-Leclerc A., Dauphin Y., Watanabe T. and Dunbar R.B. (2004)
Distribution of magnesium in coral skeleton. Geophysical Research Letters, 31, L23306, doi:10.1029/2004GL021313.

Meibom A., Cuif J.-P., Houlbreque F., Mostefaoui S., Dauphin Y., Meibom K.L. and Dunbar R. (2008)
Compositional variations at ultra-structure length scales in coral skeleton. Geochimica et Cosmochimica Acta, 72, 1555–1569.

Meibom A., Krot A.N., Robert F., Mostefaoui S., Russell S.S., Petaev M.I. and Gounelle M. (2007b)
Nitrogen and carbon isotopic composition of the Sun inferred from a high-temperature solar nebula condensate. Astrophysical Journal, 656, L33–L36.

Meibom A., Mostefaoui S., Cuif J.-P., Dauphin Y., Houlbreque F., Dunbar R. and Constantz B. (2007a)
Biological forcing controls the chemistry of reef-building coral skeleton. Geophysical Research Letters, 34, L02601, doi:10.1029/2006GL028657.

Messenger S. (2000)
Identification of molecular-cloud material in interplanetary dust particles. Nature, 404, 968–971.

Messenger S., Keller L.P. and Lauretta D.S. (2005)
Supernova olivine from cometary dust. Science, 309, 737–741.

Messenger S., Keller L.P., Stadermann F., Walker R.M. and Zinner E. (2003)
Samples of stars beyond the solar system: Silicate grains in interplanetary dust. Science, 300, 105–108.

Mondal D. and Polya D.A. (2008)
Rice is a major exposure route for arsenic in Chakdaha block, Nadia district, West Bengal, India: A probabilistic risk assessment. Applied Geochemistry, 23, 2987–2998.

Moore K.L., Schroder M., Lombi E., Zhao F.-J., McGrath S.P., Hawkesford M.J., Shewry P.R. and Grovenor C.R.M. (2010)
NanoSIMS analysis of arsenic and selenium in cereal grain. New Phytologist, 185, 434–445.

Moore K.L., Schroeder M., Wu Z., Martin B.G.H., Hawes C.R., McGrath S.P., Hawkesford M.J., Ma J.F., Zhao F.-J. and Grovenor C.R.M. (2011)
High-resolution secondary ion mass spectrometry reveals the contrasting subcellular distribution of arsenic and silicon in rice roots. Plant Physiology, 156, 913–924.

Moore K.L., Zhao F.-J., Gritsch C.S., Tosi P., Hawkesford M.J., McGrath S.P., Shewry P.R. and Grovenor C.R.M. (2012)
Localisation of iron in wheat grain using high resolution secondary ion mass spectrometry. Journal of Cereal Science, 55, 183–187.

Moreau J.W., Weber P.K., Martin M.C., Gilbert B., Hutcheon I.D. and Banfield J.F. (2007)
Extracellular proteins limit the dispersal of biogenic nanoparticles. Science, 316, 1600–1603.

Morono Y., Terada T., Nishizawa M., Ito M., Hillion F., Takahata N., Sano Y. and Inagaki F. (2011)
Carbon and nitrogen assimilation in deep subseafloor microbial cells. Proceedings of the National Academy of Sciences of the United States of America, 108, 18295–18300.

Mostefaoui S. and Hoppe P. (2004)
Discovery of abundant *in situ* silicate and spinel grains from red giant stars in a primitive meteorite. Astrophysical Journal, 613, L149–L152.

Mostefaoui S., Lugmair G.W. and Hoppe P. (2005)
^{60}Fe: A heat source for planetary differentiation from a nearby supernova explosion. Astrophysical Journal, 625, 271–277.

Mueller W.E.G., Wang X., Sinha B., Wiens M., Schroeder H.-C. and Jochum K.P. (2010)
NanoSIMS: Insights into the organization of the proteinaceous scaffold within Hexactinellid sponge spicules. ChemBioChem, 11, 1077–1082.

Musat N., Halm H., Winterholler B., Hoppe P., Peduzzi S., Hillion F., Horreard F., Amann R., Jorgensen B.B. and Kuypers M.M.M. (2008)
A single-cell view on the ecophysiology of anaerobic phototrophic bacteria. Proceedings of the National Academy of Sciences of the United States of America, 105, 17861–17866.

Nagashima K., Krot A.N. and Yurimoto H. (2004)
Stardust silicates from primitive meteorites. Nature, 428, 921–924.

references

Nagashima D., Ott U., Hoppe P. and El Goresy A. (2008)
Search for extinct ^{36}Cl: Vigarano CAIs, the Pink Angel from Allende, and a Ningqiang chondrule. Geochimica et Cosmochimica Acta, 72, 6141–6153.

Nakamura-Messenger K., Messenger S., Keller L.P., Clemett S.J. and Zolensky M.E. (2006)
Organic globules in the Tagish Lake meteorite: Remnants of the protosolar disk. Science, 314, 1439–1442.

Nguyen A., Messenger S., Ito M. and Rahman Z. (2010a)
Mg isotopic measurement of FIB-isolated presolar silicate grains. Lunar and Planetary Science, 41, abstract #2413.

Nguyen A., Messenger S., Ito M. and Rahman Z. (2011)
Fe and Mg isotopic analyses of isotopically unusual presolar silicate grains. Lunar and Planetary Science, 42, abstract #2711.

Nguyen A., Nittler L.R., Stadermann F., Stroud R. and Alexander C.M.O.D. (2010b)
Coordinated analyses of presolar grains in the Allan Hills 77307 and Queen Elizabeth Range 99177 meteorites. Astrophysical Journal, 719, 166–189.

Nguyen A.N., Stadermann F.J., Zinner E., Stroud R.M., Alexander C.M.O.D. and Nittler L.R. (2007)
Characterization of presolar silicate and oxide grains in primitive carbonaceous chondrites. Astrophysical Journal, 656, 1223–1240.

Nguyen A.N. and Zinner E. (2004)
Discovery of ancient silicate stardust in a meteorite. Science, 303, 1496–1499.

Nittler L.R., Alexander C.M.O.D., Gallino R., Hoppe P., Nguyen A.N., Stadermann F.J. and Zinner E.K. (2008)
Aluminum-, calcium- and titanium-rich oxide stardust in ordinary chondrite meteorites. Astrophysical Journal, 682, 1450–1478.

Nittler L.R., Alexander C.M.O.D., Gao X., Walker R.M. and Zinner E. (1997)
Stellar sapphires: The properties and origins of presolar Al_2O_3 in meteorites. Astrophysical Journal, 483, 475–495.

Nittler L.R. and Hoppe P. (2005)
Are presolar silicon carbide grains from novae actually from supernovae? Astrophysical Journal, 631, L89–L92.

Nittler L.R., Wang J. and Alexander C.M.O.D. (2012)
Confirmation of extreme ^{54}Cr enrichments in Orgueil nano-oxides and correlated O-isotope measurements. Lunar and Planetary Science, 43, abstract #2442.

Ong W.J., Floss C. and Gyngard F. (2012)
Negative secondary ion measurements of $^{54}Fe/^{56}Fe$ and $^{57}Fe/^{54}Fe$ in presolar silicate grains from Acfer 094. Lunar and Planetary Science, 43, abstract #1225.

Owen T., Mahaffy P.R., Niemann H.B., Atreya S. and Wong M. (2001)
Presolar nitrogen. Astrophysical Journal, 553, L77–L79.

Pacton M., Ariztegui D., Wacey D., Kilburn M.R., Rollion-Bard C., Farah R. and Vasconcelos C. (2012)
Going nano: A new step toward understanding the processes governing freshwater ooid formation. Geology, 40, 547–550.

Peixoto P., Zeghida W., Carrez D., Wu T.-D., Wattez N., Croisy A., Demeunynck M., Guerquin-Kern J.-L. and Lansiaux A. (2009)
Unusual cellular uptake of cytotoxic 4-hydroxymethyl-3-aminoacridine. European Journal of Medicinal Chemistry, 44, 4758–4763.

Pernice M., Meibom A., Van Den Heuvel A., Kopp C., Domart-Coulon I., Hoegh-Guldberg O. and Dove S. (2012)
A single-cell view of ammonium assimilation in coral-dinoflagellate symbiosis. The ISME Journal, 6, 1314–1324.

Peteranderl R. and Lechene C. (2004)
Measure of carbon and nitrogen stable isotope ratios in cultured cells. Journal of the American Society for Mass Spectrometry, 15, 478–485.

Petitat M., Marrocchi Y., McKeegan K.D., Mostefaoui S., Meibom A., Zolensky M.E. and Gounelle M. (2011)
^{53}Mn–^{53}Cr ages of Kaidun carbonates. Meteoritics and Planetary Science, 46, 275–283.

Popa R., Weber P.K., Pett-Ridge J., Finzi J.A., Fallon S.J., Hutcheon I.D., Nealson K.H. and Capone D.G. (2007)
Carbon and nitrogen fixation and metabolite exchange in and between individual cells of *Anabaena oscillarioides*. The ISME Journal, 1, 354–360.

Qin L., Nittler L.R., Alexander C.M.O.D., Wang J., Stadermann F.J. and Carlson R.W. (2011)
Extreme ^{54}Cr-rich nano-oxides in the CI chondrite Orgueil – Implication for a late supernova injection into the solar system. Geochimica et Cosmochimica Acta, 75, 629–644.

Quintana C., Bellefqih S., Laval J.Y., Guerquin-Kern J.L., Wu T.D., Avila J., Ferrer I., Arranz R. and Patino C. (2006)
Study of the localization of iron, ferritin, and hemosiderin in Alzheimer's disease hippocampus by analytical microscopy at the subcellular level. Journal of Structural Biology, 153, 42–54.

Quintana C., Wu T.-D., Delatour B., Dhenain M., Guerquin-Kern J.L. and Croisy A. (2007)
Morphological and chemical studies of pathological human and mice brain at the subcellular level: Correlation between light, electron, and NanoSIMS microscopies. Microscopy Research and Technique, 70, 281–295.

Rasmussen B., Fletcher I.R., Brocks J.J. and Kilburn M.R. (2008)
Reassessing the first appearance of eukaryotes and cyanobacteria. Nature, 455, 1101–1104.

Rauscher T., Heger A., Hoffman R.D. and Woosley S.E. (2002)
Nucleosynthesis in massive stars with improved nuclear and stellar physics. Astrophysical Journal, 576, 323–348.

references

Reynaud S., Ferrier-Pages C., Meibom A., Mostefaoui S., Mortlock R., Fairbanks R. and Allemand D. (2007)
Light and temperature effects on Sr/Ca and Mg/Ca ratios in the scleractinian coral Acropora sp. Geochimica et Cosmochimica Acta, 71, 354–362.

Rousseau M., Meibom A., Geze M., Bourrat X., Angellier M. and Lopez E. (2009)
Dynamics of sheet nacre formation in bivalves. Journal of Structural Biology, 165, 190–195.

Saal A.E., Hauri E., Cascio M.L., Van Orman J.A., Rutherford M.C. and Cooper R.F. (2008)
Volatile content of lunar volcanic glasses and the presence of water in the Moon's interior. Nature, 454, 192–196.

Sheik A.R., Brussaard C.P.D., Lavik G., Foster R.A., Musat N., Adam B. and Kuypers M.M.M. (2012)
Viral infection of *Phaeocystis globosa* impedes release of chitinous star-like structures: Quantification using single cell approaches. Environmental Microbiology, doi: 10.1111/j.1462-2920.2012.02838.x

Shimizu N. and Hart S.R. (1982)
Isotope fractionation in secondary ion mass spectrometry. Journal of Applied Physics, 53, 1303–1311.

Shirai K., Takahata N., Yamamoto H., Omata T., Sasaki T. and Sano Y. (2008)
Novel analytical approach to bivalve shell biogeochemistry: A case study of hydrothermal mussel shell. Geochemical Journal, 42, 413–420.

Sigmund P. (1969)
Theory of sputtering. I. Sputtering yield of amorphous and polycrystalline targets. Physical Review, 184, 383–416.

Simon J.I., Hutcheon I.D., Simon S.B., Matzel J.E.P., Ramon E.C., Weber P.K., Grossman L. and DePaolo D.J. (2011)
Oxygen isotope variations at the margin of a CAI records circulation within the solar nebula. Science, 331, 1175–1178.

Sinha B.W., Hoppe P., Huth J., Foley S. and Andreae M.O. (2008)
Sulfur isotope analyses of individual aerosol particles in the urban aerosol at a central European site (Mainz, Germany). Atmospheric Chemistry and Physics, 8, 7217–7238.

Slodzian G., Chaintreau M., Dennebouy R. and Rousse A. (2001)
Precise *in situ* measurements of isotopic abundances with pulse counting of sputtered ions. European Physical Journal – Applied Physics, 14, 199–231.

Slodzian G., Daigne B., Girard F. and Hillion F. (1993)
Ion optics for a high resolution scanning ion microscope and spectrometer: Transmission evaluations. In: Benninghoven A., Nihei Y., Shimizu R. and Werner H.W. (eds), Secondary Ion Mass Spectrometry SIMS IX. Wiley (Chichester), 294–297.

Slodzian G., Hillion F., Stadermann F. and Zinner E. (2004)
QSA influences on isotopic ratio measurements. Applied Surface Science, 231, 874–877.

Slodzian G., Lorin J.C. and Havette A. (1980)
Isotopic effect on the ionization probabilities in secondary ion emission. Journal of Physics, 23, 555–558.

Smart K.E., Smith J.A.C., Kilburn M.R., Martin B.G.H., Hawes C. and Grovenor C.R.M. (2010)
High-resolution elemental localization in vacuolate plant cells by nanoscale secondary ion mass spectrometry. The Plant Journal, 63, 870–879.

Smith A.H., Lopipero P.A., Bates M.N. and Steinmaus C.M. (2002)
Public health – Arsenic epidemiology and drinking water standards. Science, 296, 2145–2146.

Stadermann F.J., Croat T.K., Bernatowicz T.J., Amari S., Messenger S., Walker R.M. and Zinner E. (2005b)
Supernova graphite in the NanoSIMS: Carbon, oxygen and titanium isotopic compositions of a spherule and its TiC sub-components. Geochimica et Cosmochimica Acta, 69, 177–188.

Stadermann F.J., Floss C., Bland P.A., Vicenzi E.P. and Rost D. (2005a)
An oxygen-18 rich presolar silicate grain from the Acfer 094 meteorite: A NanoSIMS and ToF-SIMS study. Lunar and Planetary Science, 36, abstract #2004 (CD ROM).

Stadermann F.J., Hoppe P., Floss C., Heck P.R., Hörz F., Huth J., Kearsley A.T., Leitner J., Marhas K.K., McKeegan K.D. and Stephan T. (2008)
Stardust in STARDUST – The C, N and O isotopic compositions of Wild 2 cometary matter in Al foil impacts. Meteoritics and Planetary Science, 43, 299–313.

Steinhauser M.L., Bailey A.P., Senyo S.E., Guillermier C., Perlstein T.S., Gould A.P., Lee R.T. and Lechene C.P. (2012)
Multi-isotope imaging mass spectrometry quantifies stem cell division and metabolism. Nature, 481, 516–519.

Stephan T. (2001)
TOF-SIMS in cosmochemistry. Planetary and Space Science, 49, 859–906.

Stern R.A., Fletcher I.R., Rasmussen B., McNaughton N.J. and Griffin B.J. (2005)
Ion microprobe (NanoSIMS 50) Pb-isotope geochronology at < 5 μm scale. International Journal of Mass Spectrometry, 244, 125–134.

Stewart W.D.P. (1973)
Nitrogen-fixation by photosynthetic microorganisms. Annual Review of Microbiology, 27, 283–316.

references

Stolarski J., Gorzelak P., Mazur M., Marrocchi Y. and Meibom A. (2009)
Nanostructural and geochemical features of the Jurassic isocrinid columnal ossicles. Acta Palaeontologica Polonica, 54, 69–75.

Stolarski J., Kitahara M.V., Miller D.J., Cairns S.D., Mazur M. and Meibom A. (2011)
The ancient evolutionary origins of Scleractinia revealed by azooxanthellate corals. BMC Evolutionary Biology, 11, 316.

Stolarski J., Meibom A., Przenioslo R. and Mazur M. (2007)
A Cretaceous scleractinian coral with a calcitic skeleton. Science, 318, 92–94.

Tourna M., Stieglmeier M., Spang A., Könneke M., Schintlmeister A., Urich T., Engel M., Schloter M., Wagner M., Richter A. and Schleper C. (2011)
Nitrososphaera viennensis, an ammonia oxidizing archaeon from soil. Proceedings of the National Academy of Sciences of the United States of America, 108, 8420–8425.

Vollmer C. and Hoppe P. (2010)
First Fe isotopic measurement of a highly ^{17}O-enriched stardust silicate. Lunar and Planetary Science, 41, abstract #1200.

Vollmer C., Hoppe P. and Brenker F. (2008)
Si-isotopic compositions of presolar silicate grains from red giant stars and supernovae. Astrophysical Journal, 684, 611–617.

Vollmer C., Hoppe P., Stadermann F.J., Floss C. and Brenker F. (2009)
NanoSIMS analysis and auger electron spectroscopy of silicate and oxide stardust from the carbonaceous chondrite Acfer 094. Geochimica et Cosmochimica Acta, 73, 7127–7149.

Wacey D., Gleeson D. and Kilburn M.R. (2010)
Microbialite taphonomy and biogenicity: New insights from NanoSIMS. Geobiology, 8, 403–416.

Wedlock , L. , Berners-Proce S., Cliff J., Filgueira L., Kilburn M. and Saunders M. (2010)
Cellular distribution of a gold(I) based anti-cancer compound: A complementary NanoSIMS and EFTEM study. Microscopy and Microanalysis, 16 (Suppl S2), 420–421.

Woebken D., Burow L.C., Prufert-Bebout L., Bebout B.M., Hoehler T.M., Pett-Ridge J., Spormann A.M., Weber P.K. and Singer S.W. (2012)
Identification of a novel cyanobacterial group as active diazotrophs in a coastal microbial mat using NanoSIMS analysis. The ISME Journal, 6, 1427–1439.

Yada T., Floss C., Stadermann F.J., Zinner E., Nakamura T., Noguchi T. and Lea A.S. (2008)
Stardust in Antarctic micrometeorites. Meteoritics and Planetary Science, 43, 1287–1298.

Zhang D.-S., Piazza V., Perrin B.J., Rzadzinska A.K., Poczatek J.C., Wang M., Prosser H.M., Ervasti J.M., Corey D.P. and Lechene C.P. (2012)
Multi-isotope imaging mass spectrometry reveals slow protein turnover in hair-cell stereocilia. Nature, 481, 520–524.

Zinner E. (1989)
Isotopic measurements with the ion microprobe. In: Shanks W.C. III and Criss R.E. (eds). New frontiers in stable isotope research: Laser probes, ion probes and small-sample analysis, USGS Bulletin, 1890, 145–162.

Zinner E. (2007)
Presolar grains. In: Davis A.M. (ed.), Meteorites, comets and planets. Elsevier (Amsterdam), 1.

Zinner E., Amari S., Guinness R., Jennings C., Mertz A.F., Nguyen A.N., Gallino R., Hoppe P., Lugaro M., Nittler L.R. and Lewis R.S. (2007)
NanoSIMS isotopic analysis of small presolar grains: Search for Si3N4 grains from AGB stars and Al and Ti isotopic compositions of rare presolar SiC grains. Geochimica et Cosmochimica Acta, 71, 4786–4813.

Zinner E. and Crozaz G. (1986)
A method for the quantitative measurement of rare earth elements in the ion microprobe. International Journal of Mass Spectrometry and Ion Processes, 69, 17–38.

Zinner E., Nittler L.R., Hoppe P., Gallino R., Straniero O., Alexander C.M.O.D. and Lewis R.S. (2005)
Oxygen, magnesium and chromium isotopic ratios of presolar spinel grains. Geochimica et Cosmochimica Acta, 69, 4149–4165.

Zumholz K., Hansteen T., Hillion F., Horreard F. and Piatkowski U. (2007)
Elemental distribution in cephalopod statoliths: NanoSIMS provides new insights into nano-scale structure. Reviews in Fish Biology and Fisheries, 17, 487–491.

Appendix A
Table summarising NanoSIMS studies on biological materials

Kingdom	Organism	Isotope determined	Function	Correlated imaging techniques	Isotope enrichment	Reference
Prokaryote	Microbial cells	^{12}C, ^{13}C, $^{12}C^{14}N$ and $^{12}C^{15}N$	Dynamics of C and N assimilation of microbial cells in sediments samples	CARD–FISH Epifluoroscence microscopy	^{13}C-labelled glucose, pyruvate, acetate, bicarbonate, methane, ammonium and amino acids mixture; ^{15}N-labelled ammonium and amino acids	Morono *et al.* (2011)
	Cell culture of a filamentous freshwater cyanobacterium *Anabaena oscillarioides*	^{12}C, ^{13}C, $^{12}C^{14}N$ and $^{12}C^{15}N$ and ^{31}P	Uptake and exchange of metabolites by heterocyst and vegetative cells		$NaH^{13}CO_3$ and $^{15}N_2$	Popa *et al.* (2007)
	Culture of the marine cyanobacterium *Trichodesmium*	^{12}C, ^{13}C, $^{12}C^{14}N$ and $^{12}C^{15}N$ and ^{31}P	Dynamics of C and N metabolism	TEM Light microscopy	$NaH^{13}CO_3$ and $^{15}N_2$	Finzi-Hart *et al.* (2009)
	Samples from actively growing and fully lithified fossilised microbialite	^{12}C, $^{12}C^{14}N$, ^{32}S, ^{16}O, ^{24}Mg, ^{40}Ca and ^{28}Si	Trace the taphonomic preservation of both morphological and biochemical signals associated with microbes in living and recently fossilised microbialites	Light microscopy SE		Wacey *et al.* (2010)
	Culture of bacterial strains of *Escherichia coli, Bacillus subtilis* and *Pyrococcus abyssi* and uncultured microbes	^{12}C, ^{13}C, $^{12}C^{14}N$, $^{12}C^{15}N$, $^{13}C^{14}N$, ^{32}S and ^{127}I	Description of a new method (SIMS *in situ* hybridisation) allowing the simultaneous analysis of microbial identity and function		$^{13}C_6$-glucose and $^{15}NH_4Cl$	Li *et al.* (2008)
	Culture of the cyanobacteria *Anabaena* sp. and *Cylindrospermum alatosporum*	^{16}O, $^{12}C^{14}N$, ^{31}P, ^{32}S and ^{81}Br	Naturally abundant elements mapping and the distribution of bromine at subcellular lateral resolution			Eybe *et al.* (2008)
	Anaerobic phototrophic bacteria *Chlorobium clathratiforme, Chromatium okenii* and *Lamprocystis purpurea*	^{12}C, ^{13}C, $^{12}C^{14}N$, $^{12}C^{15}N$ and ^{19}F	Metabolic activities of anaerobic phototrophic bacteria and their contribution to the total ammonium and inorganic carbon assimilation in the system	HISH–SIMS CARD–FISH	$H^{13}CO_3$ and $^{15}NH_4$	Musat *et al.* (2008)
	The bacteria *Bacillus subtilis*	^{12}C, ^{13}C, $^{12}C^{14}N$, $^{12}C^{15}N$, $^{13}C^{14}N$, $^{13}C^{15}N$ and ^{32}S	Development of a combing-imaging by SIMS method (CIS) to obtain information on DNA replication and protein–DNA interactions at the level of single molecules	AFM	^{13}C-glucose and $^{15}NH_4Cl$	Cabin-Flaman *et al.* (2011)

Appendix A (continued).
Table summarising NanoSIMS studies on biological materials

Kingdom	Organism	Isotope determined	Function	Correlated imaging techniques	Isotope enrichment	Reference
	Cells of the bacteria *Escherichia coli* and *Vibrio cholerae* and cells of the heterotrophic alphaproteobacterium,*Rhizobium* sp. and a filamentous cyanobacterium, *Anabaena* sp.	For F-targeted cells: ^{12}C, ^{13}C, ^{19}F, $^{12}C^{14}N$ and $^{12}C^{15}N$; For Br-targeted cells: $^{12}C^{12}C$, $^{12}C^{13}C$, $^{12}C^{14}N$ and ^{81}Br	Combining FISH and NanoSIMS methods using elemental labelling of probe-targeted cells to study the metabolic interactions of a dual-species microbial consortium phylogenetic identity and metabolic activity	CARD–FISH EL-FISH	^{13}C-labelled amino acids mixture or $NaH^{13}CO_3$ a and $^{15}N_2$	Behrens *et al.* (2008)
	Samples of microbial mats with a non-heterocystous cyanobacterial filaments	$^{12}C^{15}N$ and $^{12}C^{14}N$	Identifying active N_2 fixing microorganisms in a complex microbial mat ecosystem and characterise their ecophysiological importance using extensive combined approaches including biogeochemical molecular and NanoSIMS analysis	CARD–FISH Fluorescence microscopy SEM	$^{15}N_2$	Woebken *et al.* (2012)
	For field experiment: Microbial community from a seawater sample; for laboratory experiment: strains of *Pseudomonas stutzeri*, *Vibrio cholerae* and *Bacillus cereus*	$^{13}C^{14}N$, $^{12}C^{14}N$ and $^{12}C^{15}N$	Development of the RNA-stable isotope probing (SIP) and its application to quantify amino acid, nucleic acid or fatty acid incorporation by 81 microbial taxa	Fluoresence microscopy	^{13}C-glucose and ^{15}N ammonium	Mayali *et al.* (2012)
	Strains of the ammonia-oxidising archaeon *Nitrososphaera viennesis*	^{12}C, ^{13}C, $^{12}C^{14}N$, ^{31}P, ^{16}O, ^{32}S and ^{19}F	Cultivation and isolation of an ammonia-oxidising archaeon from soil	TEM SEM	^{13}C-pyruvate	Tourna *et al.* (2011)
Eukaryote	Fragments of human brain hippocampus affected with Alzheimer (Alzheimer human brain) and samples of APP/PS1 transgenic mouse	$^{12}C^{14}N$, ^{16}O, ^{31}P, ^{32}S, $^{40}Ca^{16}O$ and ^{56}F	Morphological and chemical modifications in hippocampal regions of Alzheimer's disease human brain and in thalamus regions of an APP/PS1 transgenic model of amyloidosis mice brain	MRI Light microscopy TEM EDXS		Quintana *et al.* (2007)
	Fragments of human brain hippocampus affected with Alzheimer (Alzheimer human brain)	$^{12}C^{14}N$, ^{31}P, ^{32}S, $^{40}Ca^{16}O$ and ^{56}Fe	Distribution of iron, ferritin and haemosiderin at a subcellular level in the Alzheimer's disease hippocampus	TEM Light microscopy		Quintana *et al.* (2006)
	Human fibroblast cell culture, Jejunal segments of mice and *Drosophila* larvae	^{12}C, ^{13}C, $^{12}C^{14}N$, $^{12}C^{15}N$, ^{81}Br, ^{127}I, ^{31}P and ^{32}S	Imaging and quantification of stable isotope incorporation in stem cell division and metabolism with submicrometre resolution	DIC microscopy	^{15}N- and ^{13}C- labelled thymidine; $^{81}BrdU$ and iododeoxyuridine (^{127}I)	Steinhauser *et al.* (2012)
	The Bullfrogs *Rana catesbeian*, the mice *Mus musculus* and cultures utricles	^{12}C, ^{13}C, $^{12}C^{14}N$ and $^{12}C^{15}N$	Quantify protein turnover in hair cell stereocilia in the inner ear	Confocal microscopy	^{15}N-L-leucine or ^{15}N-enriched medium	Zhang *et al.* (2012)

Appendix A (continued).
Table summarising NanoSIMS studies on biological materials

Kingdom	Organism	Isotope determined	Function	Correlated imaging techniques	Isotope enrichment	Reference
	Culture of rat embryo fibroblast cells	^{12}C, ^{13}C, $^{12}C^{14}N$, $^{12}C^{15}N$ and $^{13}C^{14}N$	Measurements of isotope ratios of N and C in subcellular volumes of individual cells cultured in normal medium and ^{13}C- or ^{15}N-enriched medium		^{15}N- or ^{13}C- labelled glycine	Peterander1 and Lechene (2004)
	Human tumour cell line	^{127}I, ^{32}S, $^{12}C^{14}N$ and $^{31}P^{16}O$	Uptake and cell distribution of antitumour agent and its iodo-labelled analogue	NMR Real-time fluorescence microscopy Light microscopy		Peixoto *et al.* (2009)
	Human hairs	$^{12}C^{14}N$, ^{16}O, ^{127}I, $^{2}C_2$ and ^{32}S	Developing a method for NanoSIMS analysis that does not require preparation of thin sections			Hallegot *et al.* (2006)
	Polyps of the reef-building coral *Galaxea fascicularis*	^{12}C, ^{13}C, $^{12}C^{14}N$, ^{35}Cl, ^{31}P and ^{32}S	Uptake and metabolism of photosynthetically fixed 13C by coral symbionts	SE	$NaH^{13}CO_3$ and $NaH^{12}CO_3$	Clode *et al.* (2007)
	Tissue samples from tumour-bearing mice	^{127}I, $^{12}C^{14}N$, $^{13}C^{14}N$ and ^{31}P	Examine the specific affinity of a melanoma marker for melanin	Light microscopy	^{127}I-BZA	Guerquin-Kern *et al.* (2004)
	Human breast tumour cells	^{197}Au, $^{12}C^{14}N$ and ^{31}P	Subcellular localisation of a known Au-containing drug in tumour cells	Conventional TEM EFTEM		Wedlock *et al.* (2010)
	The bloom-forming phytoplankton *Phaeocystis globosa*	^{13}C, ^{12}C and $^{12}C^{14}N$	The impact of viral infection on carbon assimilation and cell morphology of their phytoplankton host, using bulk measurements and single-cell level	AFM SEM Epifluorescence microscopy	$H^{13}CO_3$	Sheik *et al.* (2012)
	The nickel hyperaccumulator plant *Alyssum lesbiacum*	^{58}Ni-, ^{16}O, $^{12}C^{14}N$, ^{31}P, ^{23}Na, ^{24}Mg, ^{39}K, ^{40}Ca, $^{12}C_2$ and ^{32}S	Distribution of nickel and other elements in leaf tissue	Light microscopy TEM SE		Smart *et al.* (2010)
	Durum wheat grains	^{16}O, $^{12}C^{14}N$, ^{31}P, ^{32}S, $^{31}P^{16}O$, $^{56}Fe^{16}O$ and $^{26}Si^{16}O$	Cellular and subcellular localisation of iron in in the aleurone layer and in the endosperm of immature wheat grain	SE		Moore *et al.* (2012)
	Grains of the wheat *Triticum aestivum* and of the rice *Oryza sativa*	^{16}O, $^{12}C^{14}N$, ^{32}S, $^{31}P^{16}O$ and ^{75}As or ^{80}Se	Cellular and subcellular localisation of selenium (Se) and arsenic (As) within cereal grain	S-XRF SE Optical and confocal light microscopy SEM		Moore *et al.* (2010)

GEOSTANDARDS and GEOANALYTICAL RESEARCH

Appendix A (continued).
Table summarising NanoSIMS studies on biological materials

Kingdom	Organism	Isotope determined	Function	Correlated imaging techniques	Isotope enrichment	Reference
	The rice *Oryza sativa*	$^{12}C^{14}N$, ^{28}Si, ^{31}P, ^{32}S, $^{56}Fe^{16}O$ and ^{75}As	Cellular and subcellular distributions of silicon (Si) and arsenic (As) in rice roots	TEM SE		Moore *et al.* (2011)
	HeLa cell culture and human umbilical cord endothelial cell culture	^{16}O, $^{12}C^{14}N$, ^{31}P, ^{79}Br, ^{81}Br and $^{98}Mo^{32}S$	Distribution of small molecules (BrdU and ATN-224) in cultured cells	MicroXAM Optical and fluorescence microscopy SE		Lau *et al.* (2010)
	Tissue sections of mice thyroid gland	^{12}C, $^{12}C^{14}N$, ^{31}P and ^{127}I	Expression of caveolin-1 protein in thyroid gland from normal mice and caveolin-1 knockout mice	Optical microscopy		Audinot *et al.* (2008)
	Mice sperm cells	^{16}O, ^{18}O, $^{12}C^{14}N$ and ^{28}Si	Imaging and measurement of trehalose in individual spermatozoa	QMI RDIC	^{18}O-trehalose	Lechene *et al.* (2012)
	Tissue sections of mouse cochlea, mouse brain and mouse intestinal crypt	$^{12}C^{14}N$, $^{12}C^{15}N$, ^{31}P and ^{32}S	Developing a method for a fast, semi-automatic boundary detection of regions of interests (ROI) using a support vector machine	SVM Light microscopy	^{15}N-leucine or ^{15}N-thymidine	Gormanns *et al.* (2012)
	Mouse adipocytes cell culture	^{13}C, ^{12}C, $^{12}C^{14}N$ and $^{13}C_{14}$ or $^{12}C^{15}N$	Imaging and quantification of free fatty acid (FFA) in intracellular lipid droplets of cultured adipocytes	Light microscopy RDIC	^{13}C-oleic acid	Kleinfeld *et al.* (2004)
Prokaryote and Eukaryote	The bacterium *Vibrio ficheri*, the algae *Desmodesmus subspicatus* and the crustacean *Daphnia magna*	$^{12}C^{14}N$, ^{31}P, ^{34}S, ^{107}Ag and $^{107}Ag^{16}O$	Assessing the ecotoxicological effects of Ag nanoparticles, synthesised b chemical and biological method, in aquatic organisms			Georgantzopoulou *et al.* (2012)
	Cell culture of the nitrogen-fixing bacteria *Teredinibacter turnerae*, individual bacterial symbionts in the gill of the marine bivalve *Lyrodus pedicellatus* (shipworm) and subcellular domains of bacteria-free host tissue	^{12}C, ^{13}C, $^{12}C^{14}N$ and $^{12}C^{15}N$	Localisation and measurement of the incorporation of N_2 gas	TEM	$^{15}N_2$	Lechene *et al.* (2007)
	The filamentous heterocystous cyanobacteria symbionts *Richelia intracellularis*, *Calothrix rhizosolenia* and *Climacodium frauenfeldianum* and their diatom host, *Hemiaulus membranaceus*, *Rhizosolenia devei*, *Chaetoceros* spp. and *Crocosphaera watsonii*	$^{12}C^{15}N$ and $^{12}C^{14}N$	Measurements of N_2 fixation rates of by symbiotic cyanobacteria and the N transfer to their diatom partners	Epifluorescence microscopy	$^{15}N_2$	Foster *et al.* (2011)

Appendix A (continued).
Table summarising NanoSIMS studies on biological materials

Kingdom	Organism	Isotope determined	Function	Correlated imaging techniques	Isotope enrichment	Reference
	Different types of mammalian-cultured cells and tissue sections and bacteria cells	^{12}C, ^{13}C, $^{12}C^{15}N$, $^{12}C^{14}N$, ^{31}P, ^{16}O, ^{81}Br and ^{14}C	Developing a multi-isotope imaging of biological specimens together with atomic mass images to provide qualitative and quantitative information of subcellular compartments	RDIC	^{15}N-leucine or ^{15}N-uridine or $^{15}N_2$ or ^{14}C-thymidine	Lechene *et al.* (2006)
	Plant–soil microcosms	^{12}C, $^{12}C^{14}N$, $^{12}C^{15}N$ and ^{28}Si	Imaging and measurements of nutrient resource (N) capture between competing plant cells and microorganisms within the rhizosphere	TEM	$(^{15}NH_4)_2SO_4$	Clode *et al.* (2009)
Biomineralisation	Microbes in ooid grains	^{16}O, $^{12}C_2$, $^{12}C^{14}N$, ^{28}Si and ^{32}S	Microbes role in mineral precipitation during the formation of the carbonate cortex in freshwater ooids	SEM EDXS		Pacton *et al.* (2012)
	Boreoatlantic armhook squid *Gonatus fabricii*	^{23}Na, ^{40}Ca and ^{88}Sr	Distribution of Sr and Na related to the growth of cephalopod statoliths			Zumholz *et al.* (2007)
	The diatom *Nitzschia palea*	^{28}Si, ^{29}Si, ^{30}Si, ^{16}O and $^{12}C_2$	Construction mechanism of a new valve after cell division		$K_2{}^{29}SiO_3$	Audinot *et al.* (2006)
	The Mediterranean echinoid *Paracentrotus lividus*	^{24}Mg and ^{44}Ca	Understanding the structure and organisation of the crystals that form the grinding tip of the sea urchin teeth using 3 high-resolution microscopy	X-PEEM Microbeam X-ray diffraction Polarised light microscopy SEM		Ma *et al.* (2009)
	Samples from the giant basal spicules (GBS) of the sponge *Monorhaphis chuni*	^{28}Si, ^{16}O, ^{12}C and ^{32}S	Element composition and distribution within one lamellae of the giant basal spicules (GBS)	Light microscope SEM SE		Mueller *et al.* (2010)
	The deep-sea mussel *Bathymodiolus platifrons*	^{24}Mg, ^{44}Ca, ^{55}Mn, ^{88}Sr and ^{138}Ba	Mechanism of element incorporation into bivalve shells and chemical composition of the shell	EPMA Optical microscopy SEM		Shirai *et al.* (2008)
	The reef-building coral *Stylophora pistillata* and the deep-sea coral *Desmophyllum dianthus*	^{43}Ca, ^{42}Ca, ^{87}Sr,^{88}Sr, ^{136}Ba and ^{159}Tb	Uptake dynamics of several different enriched stable isotopes and the rare earth element Tb^{3+} during coral skeletal growth	Confocal microscopy SEM Optical microscopy	^{43}Ca, ^{87}Sr and ^{136}Ba	Gagnon *et al.* (2012)

Appendix A (continued).
Table summarising NanoSIMS studies on biological materials

Kingdom	Organism	Isotope determined	Function	Correlated imaging techniques	Isotope enrichment	Reference
	Sulfate-reducing bacteria-dominated biofilms	^{12}C, $^{12}C^{14}N$, ^{32}S, ^{31}P, $^{14}N^{16}O$ and $^{14}N^{32}S$	Analysis of nanoparticle aggregates formed in natural sulfate-reducing bacterial biofilms and evaluate the potential for various amino acids to induce rapid aggregation of metal sulfide nanoparticles	TEM SEM		Moreau *et al.* (2007)
	Cell cultures of the magnetotactic bacteria *Desulfovibrio magnecticus*	$^{56}Fe^{16}O$, $^{57}Fe^{16}O$, $^{12}C^{14}N$ and ^{31}P	Cellular and molecular mechanism of magnetite biomineralisation	TEM Cryo-Ultramicrotomy Cryo-electron tomography	^{57}Fe-malate	Byrne *et al.* (2010)
	The sea urchin *Paracentrotus lividus*	^{26}Mg and ^{44}Ca	Combining ^{26}Mg labelling of the magnesium calcite skeleton of echinoids with NanoSIMS imaging of the resulting structures	SEM	^{26}MgO	Gorzelak *et al.* (2011)
	Specimens of extant deep-sea stalked crinoids	^{26}Mg and ^{44}Ca	Micro- to nanostructural and geochemical analyses of calcitic skeletons	SEM FESEM AFM μ-XRF XANES		Gorzelak *et al.* (2012)
	The reef-building coral *Acropora aspera* and its dinoflagellate *Symbiodinium* symbionts	$^{12}C^{14}N$ and $^{12}C^{15}N$	Dynamics of ammonium incorporation within the intact symbiosis between the coral and its symbionts	TEM	$^{15}NH_4Cl$	Pernice *et al.* (2012)
	The reef-building coral *Pocillopora damicornis*	^{86}Sr and ^{44}Ca	Marine bicarbonate labelling based on ^{86}Sr incorporation into the aragonitic skeleton	SEM	$^{86}SrCO_3$	Brahmi *et al.* (2012b)
	The scleractinian coral *Pocillopora damicornis*	^{86}Sr, ^{24}Mg and ^{44}Ca	Skeletal growth dynamics and chemical composition of the ultrastructural components	SEM	$^{86}SrCO_3$	Brahmi *et al.* (2012a)
	The azooxantellate scleractinian coral *Balanophyillia regia*	^{88}Sr, ^{24}Mg and ^{44}Ca	Measurements of growth rate and skeletal ultrastructure	Light and fluorescence microscopy TEM SEM		Brahmi *et al.* (2010)
	The scleractinian coral *Acropora* sp.	^{88}Sr, ^{24}Mg and ^{44}Ca	Effect of light and temperature on Sr/Ca and Mg/Ca ratios in the skeleton			Reynaud *et al.* (2007)

Appendix A (continued).
Table summarising NanoSIMS studies on biological materials

Kingdom	Organism	Isotope determined	Function	Correlated imaging techniques	Isotope enrichment	Reference
	The Cretaceous fossil coral *Coelosmilia* sp. and the present-day scleractinian *Desmophyllum* sp.	^{88}Sr, ^{24}Mg and ^{44}Ca	Comparison between the skeletal structural features of a well-preserved coral and a present-day scleractinian coral	Optical microscope SEM AFM		Stolarski *et al.* (2007)
	The fossil crinoids collected from Gnaszym, Poland	^{88}Sr, ^{24}Mg and ^{44}Ca	Fine-scale structural and geochemical features of fossil crinoid recovered from the Middle Jurassic	Optical microscope SEM -back-scattered electron AFM		Stolarski *et al.* (2009)
	Several species of deep-sea azooxanthellae reef-building corals	^{88}Sr, ^{24}Mg and ^{44}Ca	Revealing the evolutionary origin of scleractinian corals using azooxanthellate corals			Stolarski *et al.* (2011)
	The reef-building coral *Proites* sp.	^{88}Sr, ^{24}Mg and ^{44}Ca, ^{12}C, $^{12}C^{14}N$, ^{32}S	Level of biological influence over the chemistry and growth of skeletal components	Optical microscopy SEM		Meibom *et al.* (2007a,b)
	The deep-sea coral *Caryophyllia ambrosia* and the scleractinian coral *Pavona clavus*	^{88}Sr, ^{24}Mg and ^{44}Ca	Biological effects in reef-building and deep-sea coral skeletal composition	Optical microscopy SEM		Meibom *et al.* (2008)
	The scleractinian coral *Pavona clavus*	^{88}Sr, ^{24}Mg and ^{44}Ca	Distribution of magnesium and strontium in coral skeleton	SEM		Meibom *et al.* (2004)
	The marine bivalve *Pinctada margaritifera*	^{12}C, $^{12}C^{14}N$, ^{32}S	Chemical elements distribution and changes in organic components' distribution of the mineralising matrices of the nacre-prisms boundary	Confocal microscopy SEM AFM FTIR XANES		Dauphin *et al.* (2008)
	The calcareous sponge *Leuconia johnstoni*	^{24}Mg and ^{44}Ca	Composition, mineralogy and ultrastructure of giant tetractins of calcareous sponge and the organisation of surrounding cells	Optical microscopy SEM TEM AFM SXM Raman microspectroscopy		Kopp *et al.* (2011)
	The marine bivalve *Pinctada margaritifera*	^{12}C, $^{12}C^{14}N$, ^{32}S	Structure and composition of the nacreous layer of the bivalve shell	SEM AFM FTIR XANES ToF-SIMS		Dauphin *et al.* (2010)

GEOSTANDARDS and GEOANALYTICAL RESEARCH

Appendix A (continued).
Table summarising NanoSIMS studies on biological materials

Kingdom	Organism	Isotope determined	Function	Correlated imaging techniques	Isotope enrichment	Reference
	The marine bivalve *Pinctada margaritifera*	^{1}H, $^{12}C^{14}N$, ^{32}S	Distribution of organic materials around individual tablets in the topmost layer of forming nacre in bivalves	SEM		Rousseau *et al.* (2009)
	The reef-building coral *Porites porites*	^{86}Sr and ^{44}Ca	Developing a method of labelling the skeleton with the stable isotope ^{86}Sr, with subsequent NanoSIMS imagined to obtain information about the biomineralisation process	SEM	$^{86}SrCO_3$	Houlbreque *et al.* (2009)
	Cell culture of calcified MDCK epithelial cells	$^{12}C^{14}N$, ^{16}O, ^{31}P, ^{32}S and $^{40}Ca^{16}O$	Pattern of intracellular nucleation and growth of hydroxyapatite	EDXS Confocal microscopy TEM		Azari *et al.* (2008)

AFM, atomic force microscopy; CARD–FISH, catalysed reporter deposition–fluorescence *in situ* hybridisation; DIC microscopy, differential interference contrast reflection microscopy; EPMA, electron probe microanalyser; EDXS, energy-dispersive X-ray spectroscopy; EFTEM, energy-filtered transmission electron microscopy; FESEM, field emission scanning electron microscopy; FTIR, fourier transform infrared microscopy; HISH–SIMS, halogen *in situ* hybridisation–secondary ion mass spectrometry; ICP-AES, inductively coupled plasma atomic emission spectroscopy; MicroXAM, surface mapping microscope; MRI, magnetic resonance images; NMR, nuclear magnetic resonance; QMI, quantitative mass images, it is extracted from SIMS; RDIC, reflection differential interference contrast microscopy; SE, secondary electron; SEM, scanning electron microscopy; SVM, support vector machine; SXM, scanning X-ray microscopy; S-XRF, combined synchrotron X-ray fluorescence; TEM, transmission electron microscopy; ToF-SIMS, time-of-flight secondary ion mass spectrometry; XANES, X-ray absorption near-edge structure; X-PEEM, X-ray photoelectron emission spectromicroscopy; μ-XRF, X-ray micro fluorescence.